

AU No. _____

DDC FILE COPY

ADA058198

AFAL-TR-77-35

AD 45651 (2)

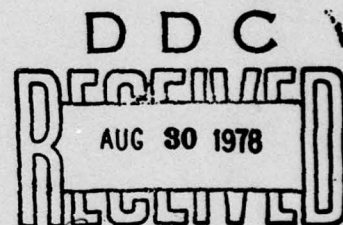


LEVEL

ADVANCED ARCHIVAL MEMORY

Corporate Research and Development
General Electric Company
Schenectady, New York 12301

April 1977



B

Quarterly Report No. 2

July 16, 1976 — October 15, 1976

Approved for public release; distribution unlimited.

78 08 15 008

AIR FORCE AVIONICS LABORATORY
AIR FORCE WRIGHT AERONAUTICAL LABORATORIES
AIR FORCE SYSTEMS COMMAND
WRIGHT-PATTERSON AIR FORCE BASE, OHIO 45433

NOTICE

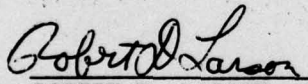
When Government drawings, specifications, or other data are used for any purpose other than in connection with a definitely related Government procurement operation, the United States Government thereby incurs no responsibility nor any obligation whatsoever; and the fact that the government may have formulated, furnished, or in any way supplied the said drawings, specifications, or other data, is not to be regarded by implication or otherwise as in any manner licensing the holder or any other person or corporation, or conveying any rights or permission to manufacture, use, or sell any patented invention that may in any way be related thereto.

This report has been reviewed by the Information Office (OI) and is releasable to the National Technical Information Service (NTIS). At NTIS it will be available to the general public, including foreign nations.

This technical report has been reviewed and is approved for publication.


JOHN M. BLASINGAME
Project Engineer

FOR THE COMMANDER


ROBERT D. LARSON, Chief
Electronic Research Branch
Air Force Avionics Laboratory

"If your address has changed, if you wish to be removed from our mailing list, or if the addressee is no longer employed by your organization please notify AFAL/DHR, W-PAFB, OH 45433 to help us maintain a current mailing list".

Copies of this report should not be returned unless return is required by security considerations, contractual obligations, or notice on a specific document.

Unclassified

SECURITY CLASSIFICATION OF THIS PAGE (When Data Entered)

REPORT DOCUMENTATION PAGE		READ INSTRUCTIONS BEFORE COMPLETING FORM
1. REPORT NUMBER AFAL-TR-77-35	2. GOVT ACCESSION NO.	3. RECIPIENT'S CATALOG NUMBER
4. TITLE (and Subtitle) Advanced Archival Memory		5. TYPE OF REPORT & PERIOD COVERED Quarterly Report No. 2 July 16, 1976-Oct. 15, '76
6. AUTHOR(s) C. Q. Lemmond, P. V. Gray, Dr. C. G. Kirkpatrick, B. D. Nathan, J. F. Norton, H. G. Parks, Dr. G. E. Possin, Dr. H. H. Woodbury		7. PERFORMING ORG. REPORT NUMBER SRD-77-074
8. PERFORMING ORGANIZATION NAME AND ADDRESS Corporate Research and Development General Electric Company Schenectady, New York 12345		9. CONTRACT OR GRANT NUMBER(s) F33615-76-C-1322
10. CONTROLLING OFFICE NAME AND ADDRESS Defense Advanced Research Project Agency 1400 Wilson Boulevard Arlington, Virginia 22209		11. PROGRAM ELEMENT, PROJECT, TASK AREA & WORK UNIT NUMBERS ARPA Order No. 3194
12. MONITORING AGENCY NAME & ADDRESS (if different from Controlling Office) Department of the Air Force Air Force Avionics Laboratory (AFSC) Wright-Patterson Air Force Base, Ohio 45433		13. REPORT DATE April 1977
14. DISTRIBUTION STATEMENT (of this Report) Approved for public release, distribution unlimited		15. NUMBER OF PAGES 158
15. DISTRIBUTION STATEMENT (of the abstract entered in Block 20, if different from Report) Quarterly Rept. no. 2, 16 Jul- 15 Oct 76		16. SECURITY CLASS. (of this report) Unclassified
17. SUPPLEMENTARY NOTES		18. DECLASSIFICATION/DOWNGRADING SCHEDULE
19. KEY WORDS (Continue on reverse side if necessary and identify by block number) Computer Ion Implantation Memory Systems Alloy Junction Electron Optics Ion Optics		
20. ABSTRACT (Continue on reverse side if necessary and identify by block number) During this reporting period, effort in the archival memory program included experimental work and theoretical studies on planar diode structures (memory target substrate), implantation of ions to write information on a planar diode structure, feasibility studies of the alloy junction method of writing using a Nd:YAG laser, the design and construction of a heated stage for alloy junction studies and the initiation of writing optics studies.		

DD FORM 1 JAN 73 1473

EDITION OF 1 NOV 65 IS OBSOLETE

Unclassified

SECURITY CLASSIFICATION OF THIS PAGE (When Data Entered)

406 627 15 008

Unclassified

SECURITY CLASSIFICATION OF THIS PAGE(When Data Entered)

20. Abstract

Studies and experimental verifications indicate that ion beam writing can be achieved using field emission ion sources. Alloy junction bit sites were successfully formed using a laser beam.

DISTRIBUTION TO	
DTIC	DTIC SOURCE
DDC	DDC SOURCE
UNCLASSIFIED	UNCLASSIFIED
BY	
DISTRIBUTION/AVAILABILITY CODES	
Dist. AVAIL. and/or SPECIAL	
A	

Unclassified

SECURITY CLASSIFICATION OF THIS PAGE(When Data Entered)

PREFACE

This is the second Quarterly Report (AFAL-TR-77-35) describing work conducted during the period July 16, 1976 to October 15, 1976. The first Quarterly Report (AFAL-TR-76-213) covers the initial investigations.

The objective of this basic research program is to investigate the feasibility of new storage techniques for large archival memories using ion and electron beam with semiconductor targets. The goal is the development of an archival memory capable of storing 10^{14} to 10^{15} bits with rapid access to the stored information.

The currently funded effort (Phase I) deals with feasibility studies of key technical areas. The program covers experimental and analytical investigations: (1) to demonstrate the feasibility of ion implanted and alloy junction storage media, (2) to determine the feasibility of beam optics design required for writing/reading on the media, and (3) to select the better of the two storage methods and perform a preliminary paper design of the concept for further development.

During this reporting period, effort in the archival memory program included experimental work and theoretical studies on planar diode structures (memory target substrate),

implantation of ions to write information on a planar diode structure, feasibility studies of the alloy junction method of writing using a Nd:YAG laser, the design and construction of a heated stage for alloy junction studies and the initiation of writing optics studies.

Ion beam writing experiments, using damage writing with inert ions, indicate that the required beam fluence for 10 Mbit/sec writing can be achieved with field emission ion sources.

Alloy junction bit sites were successfully formed using a Nd:YAG laser.

TABLE OF CONTENTS

<u>Section</u>		<u>Page</u>
	PREFACE	iii
	TABLE OF CONTENTS	v
	LIST OF ILLUSTRATIONS	vii
	LIST OF TABLES	xiii
	REPORT DOCUMENTATION	xv
I	INTRODUCTION AND SUMMARY	1
	Target Modeling Studies	2
	Target Substrate Development (Planar Diode)	3
	Ion Writing Studies	4
	Alloy Junction Writing Studies	5
II	MODELING OF CARRIER MOTION IN PLANAR DIODE STRUCTURES	7
	Description of the Model	8
	Detailed Description of the Computer Program	18
	Application of the Model	23
	Comparison to Other Work	60
	Future Plans	65
III	FABRICATION OF PLANAR DIODES	67
	Anodic Oxidation and Profile Measurement	75
IV	INFORMATION WRITING STUDIES	99
	Inert Ion Writing Experiments	99

TABLE OF CONTENTS

<u>Section</u>		<u>Page</u>
V	ALLOY JUNCTION STUDIES	107
	Metallurgical Studies	108
	Conclusions	117
	Auger Electron Spectrometer	119
	Ion Milling	122
	Alloy Junction - Eutectic Writing Experiments	124
	Laser Experiments for Eutectic Writing	126
	Thermal Bias Studies	144
VI	OPTICS STUDY	153
	REFERENCES	155

LIST OF ILLUSTRATIONS

<u>Figure</u>		<u>Page</u>
1	Model Geometry.	9
2	Format for Specification of Doping Profile.	19
3a	Computer Program for Solution of Carrier Diffusion.	24
3a	Computer Program for Solution of Carrier Diffusion.	25
3a	Computer Program for Solution of Carrier Diffusion.	26
3a	Computer Program for Solution of Carrier Diffusion.	27
3a	Computer Program for Solution of Carrier Diffusion.	28
3a	Computer Program for Solution of Carrier Diffusion.	29
3b	Typical Input-Output Sequence for Computer Program.	30
3b	Typical Input-Output Sequence for Computer Program.	31
3b	Typical Input-Output Sequence for Computer Program.	32
4	Carrier Density Profile for 100 keV As.	35
5	Measured Gain Versus Electron Beam Energy for Four Samples.	36
6	Comparison to Model Calculation for Sample A9C, As ⁺ Implant.	37
7a	Comparison to Model for Sample A17A, As ⁺ Implant.	38

LIST OF ILLUSTRATIONS

<u>Figure</u>		<u>Page</u>
7b	Comparison to Model for Sample A17A, As ⁺ Implant.	39
8	Electric Field and Electrostatic Potential.	41
9a	Model Calculations of the Collection Probability P(z).	43
9b	Model Calculations of the Collection Probability P(z).	44
10	Gain at 2 keV Based on Model Calculation.	45
11	Effect of Bulk Recombination on Collection Probability.	48
12	Schematic of Surface Recombination Modulation Experiment.	50
13	Model Calculations and Experimental Results for Surface Recombination.	53
14	Maximum Gain versus Beam Energy and Oxide Thickness.	57
15	Average Penetration of the Electron Beam in Silicon.	58
16	Schematic of Sample Geometry for Typical Application of Uniform Doping.	59
17	Dependence of Gain on Beam Energy.	61
18	Gain versus Beam Energy Measurements.	71
19	Gain versus Beam Energy Measurements.	72
20	Gain versus Beam Energy Measurements.	73
21	Four-Probe Resistivity Measurement.	77

LIST OF ILLUSTRATIONS

<u>Figure</u>		<u>Page</u>
22	Typical Anodization Curve.	80
23	Schematic of Anodization Cell.	82
24	Thickness of Si as Function of Thickness of SiO ₂ .	85
25	Schematic for Showing Derivation of the Conductivity, σ , As a Function of x.	87
26	Semilog Plot of a Linearly Decreasing Conductance (see insert) As a Function of x.	91
27	Computer Output of Calculated Carrier Concentrations Using Figure 26 As the Input.	92
28	Conductance of Sample P18A as Function of Depth.	94
29	Profile of Sample P18A.	95
30	Conductance of Sample A22A as Function of Depth.	96
31	Profile of Sample A22A.	97
32	Damage Cluster Formed Along Path of Incoming Ion.	102
33	Photomicrograph of the Spots Formed by the Laser at the Lowest Power Used.	109
34	Photomicrograph of the Spots Formed by the Laser at the Second Lowest Power Setting.	110
35	Photomicrograph of the Spots Formed by the Laser at the Third Power Setting.	111
36	Photomicrograph of the Spots Formed by the Laser at the Highest Power Setting.	112

LIST OF ILLUSTRATIONS

<u>Figure</u>		<u>Page</u>
37	Auger Profile Obtained from Spots Shown in Figure 36.	114
38	Auger Profile Obtained from Spots Shown in Figure 36.	114
39	Auger Profile Obtained from Spots Shown in Figure 35.	114
40	Auger Profile Obtained from Spots Shown in Figure 35.	115
41	Auger Profile Obtained from the Region Between Spots Shown in Figure 34.	115
42	Auger Profile Obtained from Spots Shown in Figure 33.	115
43	Auger Profile Obtained from Spots Shown in Figure 33.	116
44	Actual Auger Spectrum of the Surface on the Spot Used to Obtain the Profiles in Figure 43.	116
45	Photomicrograph Showing the Depth of Melting and Al Precipitation.	118
46	The Auger Electron Spectrometer, Ion Milling Apparatus and Associated Equipment.	120
47	Schematic Representation of the Auger Spectrometer.	121
48	The Test Chamber as Seen Through Viewing Port.	123
49	Cross Section of Target Used for Alloy Junction Experiments.	127
50	Laser Pulse Output, Laser Pulse at 22 A Lamp Drive.	130

LIST OF ILLUSTRATIONS

<u>Figure</u>		<u>Page</u>
51a	Laser Irradiated 10 x 10 Array.	133
51b	Laser Irradiated 10 x 10 Array.	134
51c	Laser Irradiated 10 x 10 Array.	135
51d	Laser Irradiated 10 x 10 Array.	136
51e	Laser Irradiated 10 x 10 Array.	137
51f	Laser Irradiated 10 x 10 Array.	138
52	Percent Modulation at 6 kV Read Beam.	139
53	Target Gain vs. Read Beam Potential.	140
54	Target Gain vs. Dead-Layer Thickness.	142
55	Photograph of Laser Heating Stage.	147
56	Schematic of Laser Heating Stage.	149

LIST OF TABLES

<u>Table</u>		<u>Page</u>
1	Parameters for Equation (9).	13
2	Comparison of Computer Results With Closed Form Solution For Constant Mobility of $E = 5 \times 10^3 \text{V/cm}$.	33
3	Summary of Planar Diode Experiments.	68
4	Summary of Planar Diode Experiments.	69
5	Auger Profiling Results.	117
6	Transmission Values of Schott Glass Filters.	129
7	Experimental Gain vs. Dead-Layer Thickness and Writing Depth.	141

SECTION I

INTRODUCTION AND SUMMARY

The Advanced Archival Memory Program is directed toward the development of a large memory with 10^{14} to 10^{15} bit capacity, rapid access to stored information ($< 100 \mu\text{sec}$. access to a block), and high data rates (10-100 Mbits/sec.). This Phase I of the overall program addresses technology studies of two memory approaches: (1) ion implantation to form surface diodes or damage bit sites, and (2) electron beam formed alloy junction surface diodes. These studies include not only memory target physics but also feasibility of the beam optics required to form bit sites by either of the approaches. At the conclusion of the studies, the better of the two storage methods will be selected based on memory target feasibility, practicability of the beam optics and applicability of such a memory to a large, rapid-access archival memory system.

During this quarter of the Advanced Archival Memory Program, a number of technical advances were made and directions for future research established in the following areas:

- Target Modeling
- Planar Diode (memory target substrate) Development
- Ion Writing
- Alloy Junction Writing

- Writing Optics Studies

Target Modeling Studies

Modeling studies, directed towards the development of analytical methods for understanding the motion of electron beam generated carriers in the large area planar collection diode, were continued and the results compared with electron beam gain versus beam energy data obtained from actual devices. Additionally, the accuracy of the model has been verified against published data. During this quarter, the model was expanded to include the entire solution of the injected carrier continuity equation, electric field effects and mobility changes resulting from doping profiles and appropriate boundary conditions. The model now applies to both the ion implant approach and the alloy junction approach.

The model studies indicate that the assumption of negligible bulk recombination is valid for the better quality planar diodes fabricated with arsenic. These studies revealed that surface recombination has an important effect on the device gain. By suitable control of surface recombination through processing, it may be possible to achieve a zero "dead-layer". This would result in the maximum possible target gain. (The "dead-layer" is the region in which carriers generated by the read electron beam are not collected by the diode.)

The model allows the introduction of bulk recombination so that ion damage writing can be modeled as well and an understanding can be gained of the motion of injected carriers as affected by damage-written bit sites. This will be investigated in more detail during the next quarter.

Target Substrate Development (Planar Diode)

Planar diode fabrication steps for silicon substrates have been developed to a point that performance is predictable. Planar diode fabrication using germanium is underway.

Studies to date have concentrated on As^+ implants into Si, since these were shown to possess the best gain characteristics at low energy. Phosphorus implants were also studied. However, the anomalous tailing which occurs with phosphorus and the less steep doping profile near the surface makes it less desirable than the arsenic implants. Modeling studies and preliminary experiments indicated that positioning the implant profile peak near the surface reduces the apparent "dead-layer" because carriers would no longer be trapped by field effects between the peak and the surface. By implanting through various oxide thicknesses, the peak has been shifted to various depths and the gain-energy relation measured. Apparent "dead-layers" only 200Å thick were observed on the better quality targets. Layers this thin result in 70% of the maximum possible gain being achieved.

Ge planar diode substrates were recently implanted with As^+ and P^+ . The target diode characteristics will be studied in the SEM during the next quarter. These will be used in the alloy junction target experiments.

In addition to the studies of gain versus beam energy performed using the scanning electron microscope, anodic oxidation and profile measurements were employed to determine carrier concentration as a function of depth.

Experiments involving As^+ implants at various energies and annealing treatments are aimed at achieving a high gain at 4 kV and will be continued during the next quarter.

Ion Writing Studies

The use of an inert ion to produce an ion damage site, rather than the ion doping mechanism initially proposed as the storage technique, was evaluated and the results are very promising. Resolution patterns were implanted using helium ions. The resulting device showed reading characteristics akin to the excellent results produced by writing diode bits with a boron ion beam. Since the fluence required for ion damage writing is at least 2 orders of magnitude less than that required for ion doping writing, up to a 100 times greater writing speed could be achieved for the same ion source.

Alloy Junction Writing Studies

Alloy junction bit diodes were formed using a laser as a means for evaluating this approach before the electron beam writing system becomes available early in the next quarter. A Nd:YAG laser was used and the beam energy controlled using neutral density filters. The target substrates were aluminum films on freshly etched silicon and germanium wafers. Single 120 nsec. laser pulses formed diodes of 5 μm (laser beam resolution limit) in diameter at the eutectic temperature (Si-Al 577°C). Studies using Auger analysis and profiling techniques verified that the alloying did occur.

In order to reduce the energy requirement on an electron beam writing system, a thermal bias of the target may be required. The temperature of the target substrate would be elevated to a point below the eutectic temperature and the electron beam heating would supply the remaining energy necessary to reach the alloying point. A heated stage was designed and fabricated for use with the laser for evaluation of this approach. A heated stage will be used with the electron beam system once it is in place.

SECTION II

MODELING OF CARRIER MOTION IN PLANAR DIODE STRUCTURES

During the previous quarter, work was initiated to establish a better understanding of the motion of electron beam generated carriers in the planar diode targets. A large number of devices were fabricated and the experimental results were analyzed using several models. This preliminary analysis suggested that it might be possible to understand the behavior of some of the better targets using a model which included no bulk recombination. This has important implications (discussed later) for the surface diode target concepts (both alloy junction and ion implant writing).

In this section, a model is discussed for the electron beam gain versus beam energy behavior of planar diode targets. The model uses the complete solution of the injected carrier continuity equation including the effects of electric fields due to doping profiles, mobility variation with doping and the appropriate boundary conditions. The generation of carriers by the electron beam as a function of penetration depth is included using the best available experimental data.

The model results support the conclusion that in properly prepared and annealed As-implanted devices the effect

of bulk recombination on the gain versus energy behavior is negligible. The results also indicate the important effect of surface recombination on the gain versus energy behavior. By proper surface treatment this could permit achieving a nearly perfect gain versus energy behavior (zero dead layer) although the practicality of this approach for surface diode targets is not clear as yet.

The second important application of the model is in understanding the motion of the injected carriers. The model permits the introduction of high bulk recombination which can be used to simulate the damage writing. This will permit a much better understanding of the writing process.

In the future the model could also be modified to include the effect of written surface diode regions. Since damage writing looks more promising, this modification has not been pursued.

Also, by examining the details of the current flow solutions from the model, it is possible to study the bit packing density limitations of the planar targets.

A. Description of the Model

Figure 1 shows the model geometry. For future reference the initial equations will be written in three-dimensional form but this model is explicitly one-dimensional. Carriers are

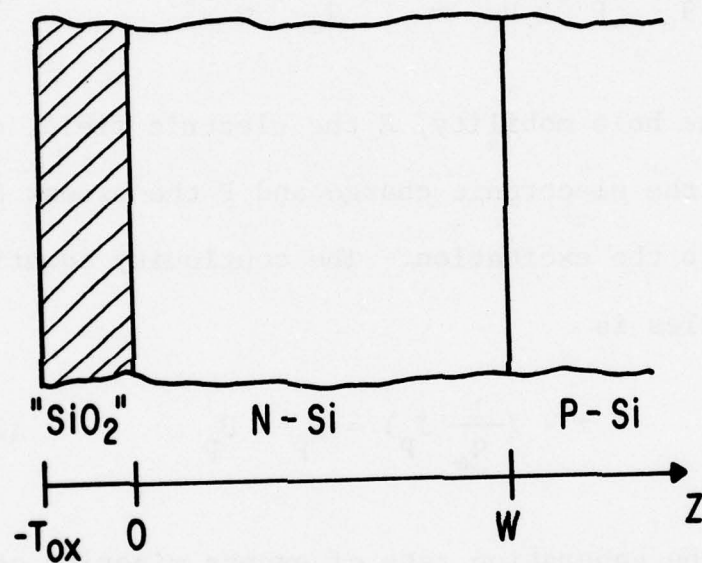


Figure 1. Model Geometry

generated by the electron beam in the n and p regions of the diode. For definiteness, we assume an n on p diode. All of the equations can be applied to p on n diodes by substituting $-E$ for E where E is the electric field.

The particle current flux of injected holes in the n material is:

$$\frac{1}{q_e} J_{\sim p} = \mu_p [PE - \left(\frac{KT}{q_e}\right) \nabla_{\sim} P] \quad (1)$$

where μ is the hole mobility, E the electric field, q_e the magnitude of the electronic charge and P the excess hole density due to the excitation. The continuity equation for the excess holes is

$$\nabla \cdot \left(\frac{1}{q_e} J_p\right) = G_p - U_p \quad (2)$$

where G_p is the generation rate of excess minority carriers (due to the electron beam in this case) and U_p is the bulk recombination rate. Expanding Equation (2) gives:

$$\mu (\nabla P \cdot \underline{E} + P \nabla \cdot \underline{E} - \frac{KT}{q_e} \nabla^2 P) + \nabla \mu \cdot (PE - \frac{KT}{q_e} \nabla P) = G_p - U_p \quad (3)$$

Since the planar diode structure is an N^+ on P diode with a typical doping ratio of $10^4:1$, the applied diode bias field is almost entirely in the P region with the part that extends

into the N^+ region typically confined to a region less than 0.01 μm from the metallurgical junction. Therefore, the electric field is assumed to be due entirely to the doping gradients. The electric field is given by:

$$\tilde{E} = - \left(\frac{KT}{q_e} \right) \frac{1}{N_e} \nabla N_e \quad (4)$$

where N_e is the total density of electrons in the unexcited device. This relation is derived from the condition of no electron current flow in the device in the unexcited state:

$$\frac{1}{q_e} J_n = -u \tilde{E} N_e - \frac{KT}{q_e} u \nabla N_e = 0 \quad (5)$$

Applying this relation to the excited device is equivalent to a small signal approximation. To calculate the electric field using Equation (4) from a measured doping profile it is assumed that $N_e = N_D$ where N_D is the density of ionized donors. This is a valid assumption as long as the Debye length

$$\lambda = \sqrt{\frac{\epsilon (KT/q)}{2q N_D}} \quad (6)$$

is small compared to the distance over which the doping is changing. For $N_D = 10^{17} \text{ cm}^{-3}$, $\lambda = 100 \text{ \AA}$ and for $N_D = 10^{19} \text{ cm}^{-3}$ $\lambda = 10 \text{ \AA}$. Hence for the typically high doping levels

considered here the assumption that $N_D = N_e$ is quite good. Algorithms exist within General Electric's Research and Development Center to calculate the exact electric field from any doping profile, if this is necessary.

The boundary conditions are

$$\mu \left(\frac{KT}{q_e} \cdot \frac{\partial P}{\partial Z} - E_p \right) = S_v P \quad Z = 0 \quad (7)$$

$$p = 0 \quad Z = W \quad (8)$$

The $Z = 0$ condition is the standard surface recombination velocity condition and is expressed in the form derived by Shockley-Reed-Hall statistics. The diode boundary conditions at $Z = W$ can be thought of as the limit of the surface recombination condition with $S_v = \infty$. A more realistic condition would be Equation (7) with $S_v \sim 5 \times 10^6$ cm/sec which is the thermal velocity of holes. Normally use of the more complex diode boundary condition makes no substantial difference in the solution. This has been verified for several typical examples.

The mobility is a strong function of the doping in the range 10^{16} to 10^{19} . Caughey and Thomas⁽¹⁾ give a useful analytic approximation to the best existing experimental data as:

$$\mu = \mu_{\min} + (\mu_{\max} - \mu_{\min})/[1 + (N/N_R)^\alpha] \quad (9)$$

where the parameters are summarized in Table 1 for electrons and holes.

TABLE 1

PARAMETERS FOR EQUATION (9)
(See References 1 and 2)

	<u>Electrons</u>	<u>Holes</u>
μ_{\max}	1360 cm ² /U sec	495 cm ² /U sec
μ_{\min}	92 cm ² /U sec	47.7 cm ² /U sec
N_R	1.3 x 10 ¹⁷ cm ⁻³	6.3 x 10 ¹⁶ cm ⁻³
α	0.91	0.76

N is the total concentration of ionized donors and acceptors. The values in Table 1 for electrons are based on a summary of the literature by Caughey and Thomas and for holes on the data of Baccarami and Ostojia.⁽²⁾ For reference, Equation (3) is repeated in explicit form for the one-dimensional solution with $U_p = p/\gamma$ as the approximation to the bulk recombination term.

$$\begin{aligned} \frac{q}{KT} \frac{1}{u} G_p + \frac{\partial^2 P}{\partial Z^2} = & \left(\frac{q}{KT} \right) \left\{ P \frac{\partial E}{\partial Z} + \frac{\partial P}{\partial Z} E \right\} \\ & + \frac{P}{\tau} \frac{q}{KT} \frac{1}{u} + \frac{1}{u} \frac{2u}{2Z} \left(PE - \frac{Kr}{q} \frac{\partial P}{\partial Z} \right) \frac{q}{KT} \end{aligned} \quad (10)$$

This equation will be solved for a set of generation functions

$$G_p = A\delta(Z-Z_o) \quad (11)$$

where $\delta(z)$ is the Dirac delta function. These are solutions for generation at a set of points z_o . Typically solutions for about 100 z_o 's will be generated. From these solutions the collection probability $P(z)$ for each z_o is obtained. As discussed in the previous quarterly report $P(z)$ can be related to the electron beam gain by

$$\text{Gain} = \frac{1}{e_i} \int_0^\infty dz P(z) q(z + T_{ox}) E_B \quad (12)$$

where $g(z, E_B)$ is the characteristic energy loss function for electron beams (see 1st quarterly report), e_i is the average electron-hole pair generation energy ($e_i = 3.64$ ev) and T_{ox} is the thickness of the top silicon dioxide layer as shown in Figure 1. Oxide thickness here means any material with a mass density near silicon and an atomic number less than about 30. For materials outside this range, it is still a reasonably good approximation to use the thickness of the material as an equivalent thickness of material T^e with the same mass thickness as silicon, i.e.

$$T^e = (\rho_{si}/\rho) T \quad (13)$$

where T is the actual thickness of the top layer with mass density ρ , and ρ_{si} is the mass density of silicon. Note that silicon and thermal silicon dioxide have almost exactly the same mass density.

Solutions to the differential equation were found using 1st ordered Merson differential equation solver; DASCURU in the International Mathematical and Statistical Subroutines Library. It is possible to obtain all the solutions for all z_0 's from a single run of DASCURU, which significantly reduces computer time. The program solves Equation (10) for P and $\partial P/\partial Z$ with $G_p = 0$. The equation is solved twice using each boundary condition separately. The solution using the $Z = 0$ boundary condition Equation (7) is designated as P_L or the left solution and the solution using the $Z = W$ condition or Equation (8) as P_R or the right solution. Since the equations are linear, the slope $\frac{\partial P}{\partial Z}$ at each end can be chosen arbitrarily and P determined by the boundary condition.

$$\frac{\partial P_L(0)}{\partial Z} = 1 \quad (14a)$$

$$P_L(0) = \frac{\left(\frac{KT}{q_e}\right) \mu \frac{\partial P_L}{\partial Z}(0)}{\mu E(0) + S_v} \quad Z = 0 \quad (14b)$$

$$\frac{\partial P_R}{\partial Z} (W) = -1 \quad (14c)$$

$$P_R (W) = 0 \quad (14d)$$

To generate a solution for the generation function $G_p = A_g(Z-Z_o)$, the left and right solutions are made continuous at $Z = Z_o$ and a complete solution constructed as follows

$$P = \begin{cases} \alpha P_L & Z \leq Z_o \\ \beta P_R & Z \geq Z_o \end{cases} \quad (15)$$

$$\frac{\alpha}{\beta} \text{ chosen so that } \alpha P_L(Z_o) = \beta P_R(Z_o) \quad (16)$$

$$\text{and } \alpha \text{ is chosen so that } \frac{1}{q_e} \nabla \cdot J_p(Z_o) = A \quad (17)$$

The collection probability can be expressed as:

$$P(Z_o) = J_p(Z=W) / [J_p(Z_o^+) - J_p(Z_o^-)] \quad (18)$$

where $J_p(Z_o^+)$ and $J_p(Z_o^-)$ are calculated from the right and left solutions respectively. Using Equations (15) through (17) it is possible to express Equation (18) directly in terms of the initial solutions P_L and P_R without actually solving for α and β . This calculation yields:

$$P(Z_o) = \frac{\mu(W)/\mu(Z_o)}{\left[\frac{\partial P_L}{\partial Z}(Z_o) \frac{P_R(Z_o)}{P_L(Z_o)} - \frac{\partial P_R}{\partial Z}(Z_o) \right]} \quad (19)$$

where it should be understood that the notation $\mu(Z)$ means the value of the mobility evaluated at the doping at depth z .

For $z > W$, it is assumed that $P(z) = 1$. If the distance to the backside contact is large compared to $z-W$, this is a good approximation in the absence of bulk recombination. In the presence of uniform bulk recombination it can be shown that the collection probability on the other side of the junction is $\exp\left(-\frac{(z-W)}{L_p}\right)$ where $L_p = (D\tau)^{1/2}$ is the recombination length. For good quality silicon $L_p > 25 \mu\text{m}$ so that for typical maximum beam penetrations past the diode junction ($\sim 1 \mu\text{m}$) the collection probability is almost exactly 1 as assumed. However poor quality silicon or damage due to the junction formation could cause high recombination and invalidate this assumption. Some evidence for high recombination near the junction will be discussed in a following section. The computer program also calculates and displays the two components to the minority carrier particle current in Equation (1)

$$J_{\text{cond}}/q = F_{\text{cond}} = \mu PE \quad (20)$$

$$J_{\text{diff}}/q = F_{\text{diff}} = -\mu (KT/q) \partial P/\partial Z \quad (21)$$

as well as the total particle current:

$$J/q = F_T = F_{\text{cond}} + F_{\text{diff}} \quad (22)$$

The importance of these separate contributions to the carrier flux will be investigated during the following quarter. In the absence of bulk recombination the total carrier flux F_T must be a constant for the right and left solutions since neither of these solutions has any carrier generation. This provides a useful check on the quality of the solution. Normally this flux is constant to better than 0.1% over the entire range of the solution.

B. Detailed Description of the Computer Program

The following describes in more detail the operation from the user point of view of the computer program for solving the carrier collection probability problem just described.

In its present version a large amount of data is input at run time in an interactive fashion. The program accepts a doping profile of the type shown in Figure 2. All of the

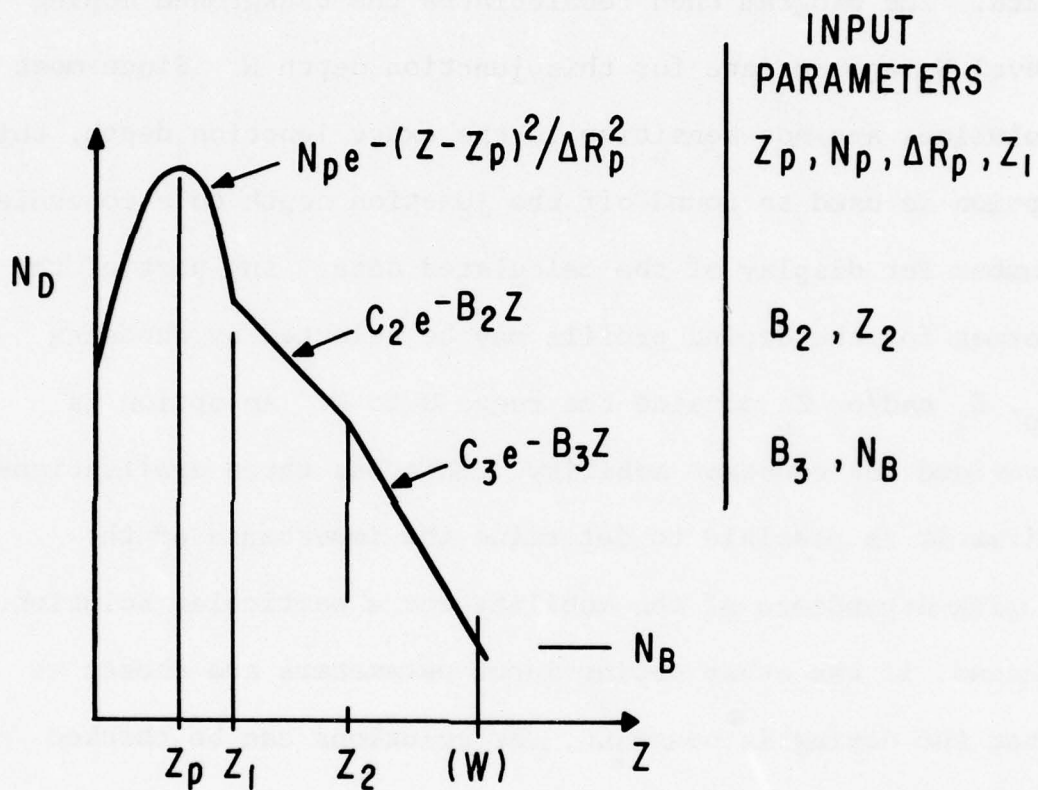


Figure 2. Format for Specification of Doping Profile

parameters listed on the right must be provided by the user. The other parameters (C_2 , C_3 , and W) are calculated by the program and displayed. The one exception is the junction depth W which at the users option can be provided as input data. The program then recalculates the background doping level N_B appropriate for this junction depth W . Since most solutions are not sensitive to the exact junction depth, this option is used to round off the junction depth to a convenient number for display of the calculated data. Any part of the format for the doping profile may be selected by choosing Z_p , Z_1 and/or Z_2 outside the range 0 to W . An option is provided for constant mobility. This has three applications. First it is possible to determine the importance of the doping dependence of the mobility for a particular solution. Second, if the other doping input parameters are chosen so that the doping is constant, the solutions can be checked against the closed form BEAMOS solutions. Third, if the doping parameters are chosen so that the electric field is constant, then the solutions may be checked against the closed form solutions due to Guildberg and Schroter⁽³⁾ which assume constant mobility.

In the present program bulk recombination is assumed to follow

$$U_p = p/\tau \quad (23)$$

At run time the following recombination data must be provided

$$\tau = \begin{cases} \tau_1 & Z < Z_\tau \\ 1 \text{ sec} & Z > Z_\tau \end{cases} \quad (24)$$

This is a very rudimentary form and serves only for preliminary exploration of the effects of bulk recombination. The abrupt discontinuity causes some convergence problems for DASCUR. These are not believed to seriously affect the final solutions except near the discontinuity, but during next quarter this convergence problem will be eliminated either by providing a more realistic functional form for $\tau(z)$ or by an algorithm to step across the discontinuity. Such a procedure is used for the doping profile as discussed below.

Note that the doping profile has slope discontinuities at Z_1 and Z_2 . This produces a discontinuity in the values of the electric field E . Equation (10) contains the term $\partial E/\partial Z$ which is undefined at Z_1 and Z_2 . A more physical way to handle this would be to smooth out the doping profile so that this discontinuity did not occur. A simpler method is to step across such discontinuities using the condition that the carrier flux is constant. This is a good approximation, if the distance of the step is small enough. The present program has a step size

across the discontinuity of $V = 10^{-9}$ cm.

The program contains a backscatter correction factor F . This is the amount of electron beam energy backscattered from the target. For materials with atomic number $Z \sim 13$, $F \approx 0.08$ (ref. 5). Note that F is the energy backscatter fraction and not the usually quoted number backscatter fraction which is typically twice as large since the mean average backscatter energy is about 0.5 times the beam energy for low Z materials. The present program has $F = 0.08$ built-in, since this is appropriate for targets with Al, SiO_2 or Si surfaces.

The surface recombination velocity S_v must be provided along with the initial doping and recombination data. New values of S_v can be provided without inputting new doping and recombination data. An additional option permits providing non-zero values for the oxide thickness T_{ox} in Figure 1. The collection probability and gain versus energy data is always calculated first for $T_{\text{ox}} = 0$. Since the collection probability is not affected by the oxide thickness (at least in the model where any effects of the passivating oxide on the surface recombination must be provided by the user) only the gain versus energy curve is displayed for each oxide thickness.

Both n and p type top layers can be accommodated. The program is written for n-type material. Responding to the

question n or p type with 2 for p type causes the use of the appropriate values for the mobility (from Table 1). The electric field is then calculated using $E = -(kT/q)N_A$ where the sign is deliberately taken incorrectly as minus. This incorrect choice of sign causes Equations (7) and (8) to be correct for p type top layers. This version of the program also displays the electric field with this deliberate sign inversion.

Figure 3 is a listing of the program and a typical program input and output sequence. User responses are circled. The diagnostic output is suppressed by responding with any other integer besides 1 to the request for diagnostic output. The important part of the calculation is the collection probability and the gain versus beam energy derived from it.

C. Application of the Model

As mentioned earlier, the program will also display the total particle current F for both the left and right solutions. In the absence of bulk recombination these currents must be constant and this is normally observed (see Figure 3 fourth column in diagnostic output). This is probably the strongest indication of correct program operation. A second check was run against the closed form

THIS PAGE IS BEST QUALITY PRACTICABLE
FROM COPY FURNISHED TO DDG

```

SYSTEM'YFOR
old or new-OLD GADP6
ready
*LIST

002**RUN =(JLIB)LIBRARY/IMSL,R
004 * CALCULATES COLLECTION PROB AND GAIN VERS E FROM DOPING
006 * PROFILE AND RECOMBINATION PROFILE-CORRECTED TO INCLUDE
008 *BACKSCATTER FRACTION 9/27/76
010 * DEPENDANCE OF MOBILITY ON DOPING INCORPORATED 10/12/76
012 * OXIDE ON TOP OF TARGET OPTION INCORPORATED 10/16/76
013 * CORRECTED FOR ERROR IN HANDLING SECOND SINGULARITY 11/8/76
014 EXTERNAL DERIV
016 INTEGER DIAG,TYPE
018 REAL NP,NB,MCD,LJ,LJC,LJD,MUMAX,MUMIN,MU,MUD,MUW,MOBILITY
020 DIMENSION WK(8),XO(2),CP(300),PL(300),DPL(300),PR(300),DPR(300)
022 DIMENSION ZSING(10)
024 COMMON QKT,TAUI,ZTAUI,NP,B2,B3,ZP,DELRP,Z1,Z2,W,C2,C3,
026 & MUMAX,MUMIN,CR,ALPHA
028 LAMDA(ZR)=0.6+6.21*ZR-12.40*ZR^2+5.69*ZR^3
030 RANGE(E)=(0.00430/2320.0)*E^1.75
032 F=0.08
034 * DATA INPUT
036 20 PRINT,"DOPING TYPE 1-N, 2-P, 3-CONSTANT MU": READ,TYPE
038 * FOR P-TYPE ELECTRIC FIELD IS WRONG SIGN BUT REST WILL BE OKAY
040 IF(TYPE.EQ.3) GO TO 94: IF(TYPE.EQ.1) GO TO 92
042 MUMAX=1367
044 MUMIN=92
046 ALPHA=0.91
048 CR=1.3E17
050 GO TO 93
052 92 MUMAX=495
054 MUMIN=47.7
056 ALPHA=0.76
058 CR=6.3E16: GO TO 93
060 94 PRINT,"CONSTANT MU":READ,MU:MUMAX=MU:MUMIN=MU:ALPHA=1:CR=1E15
062 93 PRINT,"INPUT DOPING PARAMETERS IN MICRONS AND #/CM^3"
064 PRINT,"ZP,DELRP,Z1,Z2"
066 READ,ZP,DELRP,Z1,Z2
068 PRINT,"NP,NB,B2,B3"
070 READ,NP,NB,B2,B3
072 PRINT,"RECOMB PARAMETERS TAUI,ZTAUI IN SEC AND MICRONS"
074 READ,TAUI,ZTAUI
076 ZTAUI=ZTAUI*1E-4
078 ZP=ZP*1E-4
080 DELRP=DELRP*1E-4
082 Z1=Z1*1E-4
084 Z2=Z2*1E-4

```

Figure 3a. Computer Program for Solution of Carrier Diffusion Equation in Planar Diode Structures

```

080 C2=NP*EXP(B2*Z1-((Z1-ZP)/DEL RP)^2)
086 C3=C2*EXP(Z2*(B3-B2))
090 IF(NB.GT.MCD(Z1)) GO TO 55
092 IF(NB.GT.MCD(Z2)) GO TO 56
094 GO TO 16
096 55 W=ZP+DEL RP*SQRT(ALOG(NP/NB)); GO TO 90
098 56 W=ALOG(C2/NB)/B2; GO TO 90
100 16 W=ALOG(C3/NB)/B3
102 90 PRINT,"SURFACE RECOMBINATION VEL CM/SEC?"; READ,S0
104 1 FORMAT(1H ,2F10.3)
106 2 FORMAT(1H ,13,5E12.3,F7.3)
108 3 FORMAT(1H ,E12.3,F10.4,2E14.3)
110 4 FORMAT(1H ,E12.4,F12.4)
112 5 FORMAT(1H ,5F10.4)
114 6 FORMAT(1H ,4E12.3)
116 7 FORMAT(5H S0= ,E10.2,7H CM/SEC)
118 8 FORMAT(5H TAU1=,E10.2,4H SEC)
120 9 FORMAT(6H ZTAU1=,F10.3,8H MICRONS)
122 10 FORMAT(1H ,2E12.3)
124 61 FORMAT(5H TOX= ,F10.3,8H MICRONS)
126 PRINT," "
128 IF(TYPE.EQ.1) PRINT," N-TYPE"; IF(TYPE.EQ.2) PRINT," P-TYPE"
130 IF(TYPE.EQ.3) PRINT,"MOBILITY=",MUMAX
132 17 PRINT," ZP DEL RP Z1 Z2 W ALL IN MICRONS"
134 PRINT 5, ZP*1E4,DEL RP*1E4,Z1*1E4,Z2*1E4,W*1E4; PRINT," "
136 PRINT," NP CM-3 NB CM-3 C2 CM-3 C3 CM-3 "
138 PRINT 6, NP,NB,C2,C3; PRINT," "
140 PRINT," B2 CM-1 B3 CM-1 "
142 PRINT 10,B2,B3; PRINT," "
144 PRINT 7,S0
146 PRINT 8,TAU1; PRINT 9,ZTAU1*1E4
148 PRINT,"OPTIONS - NEW DATA-1, NEW JCT DEPTH-2,CONTINUE-3"
150 READ,DIAG; IF(DIAG.EQ.1) GO TO 20; IF(DIAG.EQ.2) GO TO 14
152 GO TO 15
154 14 PRINT,"NEW VALUE FOR JCT DEPTH W"
156 READ,W; W=1E-4*W; PRINT,"W=",W*1E4," MICRONS"; NB=MCD(W)
158 PRINT,"NB= ",NB," CM-3"
160 15 PRINT," NUMBER OF DISPLAYED POINTS AND COMPUTED POINTS PER PT."
162 READ,MD,MP; M=MP*MD; IF(M.GT.300) PRINT," TOO MANY POINTS-ERROR!"
164 PRINT,"IF YOU WISH DIAGNOSTIC OUTPUT INPUT 1"; READ,DIAG
166 * CALCULATE PARAMETERS RELATING TO ELECTRIC FIELD
168 OKT=0.025
170 EZERO=ELECT(0)
172 EW=ELECT(W)
174 DEL=W/M
176 EG=3.65
178 *SET UP SINGULARITIES
180 JI=0
182 IF(Z1.LT.0.(OR.Z1.GT.W) GO TO 11

```

Figure 3a. Computer Program for Solution of Carrier Diffusion Equation in Planar Diode Structures (continued)

THIS PAGE IS BEST QUALITY PRACTICABLE
FROM COPY FURNISHED TO DDC

```

184 JT=JT+1; ZSING(JT)=Z1
186 11 IF(Z2.LT.0.OR.Z2.GT.W) GO TO 12
188 JT=JT+1; ZSING(JT)=Z2
190 12 V=1E-9
192 *LEFT SOLUTION - IF B=ZS THEN DPL IS FOR ZS-
194 I=0; H=W/1000; OLDH=H/2; J=1
196 ZS=1E4; IF(JT.GT.0) ZS=ZSING(J)
198 DPLZERO=1; XO(2)=DPLZERO
200 CD=MCD(0); MUO=MOBILITY(CD); D=QKT*MUO
202 PLZERO=DPLZERO*D/(MUO*EZERO+S0); XO(1)=PLZERO
204 DPLZERO=1; XO(2)=DPLZERO
206 B=0
208 30 A=B; B=(I+1)*DEL
210 IZS=2
212 IF(ABS(B-ZS).LT.V) GO TO 34
214 IZS=1
216 IF(B-ZS.GT.0) GO TO 34
218 IZS=3
220 34 IF(IZS.GT.1) GO TO 31
222 CALL DASCUR(DERIV,A,ZS-V,H,2,XO,WK,IER)
224 XO(2)=XO(2)+XO(1)*(ELECT(ZS+V)-ELECT(ZS-V))/QKT
226 CALL DASCUR(DERIV,ZS+V,B,H,2,XO,WK,IER)
228 GO TO 33
230 31 IF(IZS.GT.2) GO TO 32
232 CALL DASCUR(DERIV,A,ZS-V,H,2,XO,WK,IER)
234 GO TO 33
236 32 CALL DASCUR(DERIV,A,B,H,2,XO,WK,IER)
238 GO TO 33
240 33 I=I+1
242 PL(I)=XO(1); DPL(I)=XO(2)
244 IF(IZS.EQ.2) XO(2)=XO(2)+XO(1)*(ELECT(ZS+V)-ELECT(ZS-V))/QKT
246 IF(IZS.EQ.3) GO TO 35
248 J=J+1; ZS=ZSING(J); IF(J.GT.JT) ZS=1E4
250 35 IF(IER.EQ.33.OR.IER1.EQ.33) PRINT,"NO CONV-LEFT SOL I=",I
252 IER1=0
254 IF(I.NE.M) GO TO 30
256 *RIGHT SOLUTION-IF B=ZS THEN DPR FOR ZS-
258 I=M; H=W/1000; J=JT
260 ZS=-1E4; IF(JT.GT.0) ZS=ZSING(J)
262 DPR(I)=-1; XO(2)=DPR(I)
264 PR(I)=0; XO(1)=PR(I)
266 B=W
268 36 A=B; B=(I-1)*DEL
270 IZS=2
272 IF(ABS(B-ZS).LT.V) GO TO 37
274 IZS=3
276 IF(B-ZS.GT.0) GO TO 37
278 IZS=1
280 37 IF(IZS.GT.1) GO TO 38

```

Figure 3a. Computer Program for Solution of Carrier Diffusion Equation in Planar Diode Structures (continued)

```

282 CALL DASCUR(DERIV,A,ZS+V,H,2,XO,WK,IER)
284 XO(2)=XO(2)+XO(1)*(ELECT(ZS-V)-ELECT(ZS+V))/QKT
286 CALL DASCUR(DERIV,ZS-V,B,H,2,XO,WK,IER)
288 GO TO 43
290 38 IF(IZS.GT.2) GO TO 39
292 CALL DASCUR(DERIV,A,ZS+V,H,2,XO,WK,IER)
294 XO(2)=XO(2)+XO(1)*(ELECT(ZS-V)-ELECT(ZS+V))/QKT
296 GO TO 43
298 39 CALL DASCUR(DERIV,A,B,H,2,XO,WK,IER)
300 GO TO 44
302 43 J=J-1; ZS=ZSING(J); IF(J.LT.1) ZS=-1E4
304 44 IF(IER.EQ.33.OR.IER1.EQ.33) PRINT," NO CONV RIGHT SOL I=",I
306 I=I-1; IF(I.EQ.0) GO TO 45
308 PR(I)=XO(1); DPR(I)=XO(2); GO TO 36
310 45 PRZERO=XO(1); DPRZERO=XO(2)
312 CD=MCD(W); MUW=MOBILITY(CD)
314 DO 40 I=1,M,1
316 CD=MCD(I*DEL); MU=MOBILITY(CD); TOP=MUW/MU
318 40 CP(I) = -1*TOP/(DPR(I)-DPL(I)*(PR(I)/PL(I)))
320 TOP=MUW/MUO
322 CPZERO=-1*TOP/(DPRZERO-DPLZERO*(PRZERO/PLZERO))
324 IF(DIAG.NE.1) GO TO 27
326 PRINT," M=",M," MP=",MP; PRINT," "
328 PRINT," RIGHT SOLUTION
330 PRINT," I PR DPR TOTAL CURRENTS" COND DIFF
332 & Z-MICRONS"
334 I=0; RJC=MUO*EZERO*PRZERO; RJD=-1*MUO*QKT*DPRZERO; RJ=RJC+RJD
336 PRINT 2,I,PRZERO,DPRZERO,RJ,RJC,RJD,I*DEL*1E4
338 DO 19 I=MP,M,MP
340 CD=MCD(I*DEL); MU=MOBILITY(CD)
342 RJC=MU*ELECT(I*DEL-V)*PR(I); RJD=-1*MU*QKT*DPR(I); RJ=RJC+RJD
344 19 PRINT 2,I,PR(I),DPR(I),RJ,RJC,RJD,I*DEL*1E4
346 PRINT," "
348 PRINT," LEFT SOLUTION
350 PRINT," I PL DPL TOTAL CURRENTS" COND DIFF
352 & Z-MICRONS"
354 I=0; LJC=MUO*EZERO*PLZERO; LJD=-1*MUO*QKT*DPLZERO; LJ=LJC+LJD
356 PRINT 2,I,PLZERO,DPLZERO,LJ,LJC,LJD,I*DEL*1E4
358 DO 28 I=MP,M,MP
360 CD=MCD(I*DEL); MU=MOBILITY(CD)
362 LJC=MU*ELECT(I*DEL-V)*PL(I); LJD=-1*MU*QKT*DPL(I); LJ=LJC+LJD
364 28 PRINT 2,I,PL(I),DPL(I),LJ,LJC,LJD,I*DEL*1E4
366 18 IF(JT.EQ.0) GO TO 27
368 PRINT," "; PRINT," ZSING(J) J"
370 DO 29 J=1,JT,1
372 29 PRINT,ZSING(J),J
374 *PRINT RESULTS
376 PRINT," "
378 27 PRINT," COLL PROB Z-MICRONS"

```

Figure 3a. Computer Program for Solution of Carrier Diffusion Equation in Planar Diode Structures (continued)

THIS PAGE IS BEST QUALITY PRACTICABLE
FROM COPY FURNISHED TO DDC

```

380 PRINT 4, CPZERO,0
382 DO 41 I=MP,M,MP
384 41 PRINT 4, CP(I), I*DEL*IE4
386 IOX=0; GO TO 96
388 95 PRINT,"OXIDE THICKNESS IN MICRONS"; READ,TOX
390 TOX=TOX*IE-4; IOX=INT(TOX/DEL)
392 96 TOX=IOX*DEL; PRINT 61,TOX*IE4
394 PRINT,"      GAIN      E-KEV"
396 IE=0
398 23 IE=IE+1; ENERGY=0.5*IE
400 RDEL=RANGE(ENERGY)/DEL
402 IM=INT(RDEL); IF(IM-IOX.LE.4) GO TO 23
404 CPR=1; IF(IM-IOX.LE.M) CPR=CP(IM-IOX)
406 SUM=CPZERO*LAMDA(IOX/RDEL)+CPR*LAMDA(IM/RDEL)
408 DO 24 I=IOX+1,IM-1,1
410 CPR=1; IF(I-IOX.LE.M) CPR=CP(I-IOX)
412 24 SUM=SUM+2*CPR*LAMDA(I/RDEL)
414 GAIN=(ENERGY*1000*(1-F)/(EG*2*RDEL))*SUM
416 PRINT 1,GAIN,ENERGY
418 IF(IE.GT.9)IE=IE+1; IF(IE.LT.30)GO TO 23
420 42 PRINT," OPTIONS, 1-NEW DATA, 2-QUIT, 3-ELECT&DOPING, 4-NEW SV,
421 & 5-OXIDE"
422 READ,K; IF(K-2)20,99,22
424 22 IF(K.EQ.4) GO TO 90; IF(K.EQ.5) GO TO 95
426 PRINT,"      E V/CM      Z-MICRONS      N-DOPING CM^-3      MOBILITY"
428 DO 13 I=1,M+1,MP; Z=(I-1)*DEL
430 CD=MCD(Z)
432 13 PRINT 3, ELECT(Z),Z*IE4,CD,MOBILITY(CD)
434 GO TO 42
436 99 PRINT," ALL DONE"
438 STOP
440 END
442 FUNCTION MCD(Z)
444 REAL MCD
446 *CALCULATES MAJORITY CARRIER OR DOPING DENSITY IN CM^-3
448 REAL NP
450 COMMON QKT,TAUI,ZTAUI,NP,B2,B3,ZP,DELRP,Z1,Z2,W,C2,C3
452 IF(Z.LT.Z1) GO TO 71; IF(Z.LT.Z2) GO TO 72; GO TO 73
454 71 MCD = NP*EXP(-1*((Z-ZP)/DELRP)^2); GO TO 74
456 72 MCD = C2*EXP(-1*Z*B2); GO TO 74
458 73 MCD = C3*EXP(-1*Z*B3); GO TO 74
460 74 RETURN
462 END
464 FUNCTION ELECT(Z)
466 REAL ELECT,NP
468 COMMON QKT,TAUI,ZTAUI,NP,B2,B3,ZP,DELRP,Z1,Z2,W
470 * CALCULATION OF ELECTRIC FIELD EZ AT Z
472 IF(Z .LT. Z1) GO TO 51
474 IF(Z .LT. Z2) GO TO 52

```

Figure 3a. Computer Program for Solution of Carrier Diffusion Equation in Planar Diode Structures (continued)

```

476 GO TO 53
478 51 EZ=QKT*2*(Z-ZP)/DELRP^2; GO TO 54
480 52 EZ=QKT*B2; GO TO 54
482 53 EZ=QKT*B3
484 54 ELECT=EZ
486 RETURN
488 END
490 * DERIVATIVE EVALUATION
492 SUBROUTINE DERIV(XO,Z,N,XP)
494 DIMENSION XO(N),XP(N)
496 REAL NP,MU,MUMAX,MUMIN
498 COMMON QKT,TAUI,ZTAUI,NP,B2,B3,ZP,DELRP,Z1,Z2,W,C2,C3,
500 & MUMAX,MUMIN,CR,ALPHA
502 * CALCULATION OF ELECTRIC FIELD EZ AT Z
504 IF(Z.LT.Z1) GO TO 51
506 IF(Z.LT.Z2) GO TO 52; GO TO 53
508 51 EZ=QKT*2*(Z-ZP)/DELRP^2; GO TO 54
510 52 EZ=QKT*B2; GO TO 54
512 53 EZ=QKT*B3
514 * CALCULATION OF TAU
516 54 TAU=1
518 IF(Z.LT.ZTAUI) TAU=TAUI
520 * CALCULATION OF DIV OF ELECTRIC FIELD
522 IF(Z.LT.Z1) GO TO 81; IF(Z.LT.Z2) GO TO 82; GO TO 83
524 81 DEZ = QKT*2/DELRP^2; GO TO 84
526 82 DEZ = 0; GO TO 84
528 83 DEZ = 0; GO TO 84
530 *CALCULATION OF CARRIER DENSITY & MOBILITY
532 84 IF(Z.LT.Z1) GO TO 71; IF(Z.LT.Z2) GO TO 72; GO TO 73
534 71 CD = NP*EXP(-1*((Z-ZP)/DELRP)^2); GO TO 74
536 72 CD = C2*EXP(-1*Z*B2); GO TO 74
538 73 CD = C3*EXP(-1*Z*B3)
540 74 MU=MUMIN+(MUMAX-MUMIN)/(1+(CD/CR)^ALPHA)
542 DMU=(MUMIN-MUMAX)*ALPHA*(CD/CR)^(ALPHA-1)/(1+(CD/CR)^ALPHA)^2
544 DMU=-1*DMU*EZ*(CD/CR)/QKT
546 XP(1)=XO(2)
548 XP(2)=(EZ*XO(2)+(DEZ+1/(TAU*MU))*XO(1))/QKT+(DMU/MU)*
550 & (XO(1)*EZ/QKT-XO(2))
552 RETURN
554 END
556 FUNCTION MOBILITY(CD)
558 REAL MOBILITY,MUMAX,MUMIN
560 COMMON QKT,TAUI,ZTAUI,NP,B2,B3,ZP,DELRP,Z1,Z2,W,C2,C3,
562 & MUMAX,MUMIN,CR,ALPHA
564 MOBILITY=MUMIN+(MUMAX-MUMIN)/(1+(CD/CR)^ALPHA)
566 RETURN
568 END

```

Figure 3a. Computer Program for Solution of Carrier Diffusion Equation in Planar Diode Structures (continued)

THIS PAGE IS BEST QUALITY PRACTICABLE
FROM COPY FURNISHED TO DDC

1
DOPING TYPE 1-N, 2-P, 3-CONSTANT MU
=1
INPUT DOPING PARAMETERS IN MICRONS AND #/CM³
ZP, DELRP, Z1, Z2
=0.075, 0.042, 0.125, 1
NP, NB, B2, B3
=1.1E19, 1E15, 2E5, 10
RECOMB PARAMETERS TAU1, ZTAU1 IN SEC AND MICRONS
=1, 1
SURFACE RECOMBINATION VEL CM/SEC?
=1E7

N-TYPE TOP LAYER
DOPING PROFILE
RECOMBINATION PARAMETERS
SURFACE RECOMBINATION VELOCITY

N-TYPE					W ALL IN MICRONS
ZP	DELRP	Z1	Z2		
0.0750	0.0420	0.1250	1.0000		0.5194
NP CM-3	NB CM-3	C2 CM-3	C3 CM-3		
0.110E 20	0.100E 16	0.325E 20	0.670E 11		
B2 CM-1	B3 CM-1				
0.200E 06	0.100E 02				

SO= 0.10E 08 CM/SEC
TAU1= 0.10E 01 SEC
ZTAU1= 1.000 MICRONS
OPTIONS - NEW DATA-1, NEW JCT DEPTH-2, CONTINUE-3
=2
NEW VALUE FOR JCT DEPTH W
=3
W= 0.30000000E 00 MICRONS
NB= 0.80512860E 17 CM-3
NUMBER OF DISPLAYED POINTS AND COMPUTED POINTS PER PT.
=15, 10
IF YOU WISH DIAGNOSTIC OUTPUT INPUT 1
=1

CHARGE JUNCTION DEPTH
REQUEST DIAGNOSTIC OUTPUT OPTION

RIGHT SOLUTION			CURRENTS					Z-MICRONS
I	PR	DPR	TOTAL	COND	DIFF			
0	0.796E-03	-0.679E 03	0.626E 01	-0.219E 04	0.219E 04	0.		
10	0.179E-03	-0.115E 03	0.622E 01	-0.213E 03	0.224E 03	0.020		
20	0.598E-04	-0.277E 02	0.625E 01	-0.369E 02	0.431E 02	0.040		
30	0.272E-04	-0.900E 01	0.626E 01	-0.662E 01	0.129E 02	0.060		
40	0.156E-04	-0.355E 01	0.626E 01	0.124E 01	0.502E 01	0.080		
50	0.110E-04	-0.112E 01	0.626E 01	0.462E 01	0.164E 01	0.100		
60	0.116E-04	0.224E 01	0.626E 01	0.101E 02	-0.380E 01	0.120		
70	0.119E-04	-0.830E 00	0.626E 01	0.464E 01	0.162E 01	0.140		
80	0.103E-04	-0.798E 00	0.626E 01	0.451E 01	0.175E 01	0.160		
90	0.871E-05	-0.751E 00	0.626E 01	0.438E 01	0.189E 01	0.180		
100	0.726E-05	-0.701E 00	0.626E 01	0.422E 01	0.204E 01	0.200		
110	0.590E-05	-0.663E 00	0.626E 01	0.401E 01	0.225E 01	0.220		
120	0.458E-05	-0.654E 00	0.626E 01	0.366E 01	0.261E 01	0.240		
130	0.325E-05	-0.691E 00	0.626E 01	0.304E 01	0.323E 01	0.260		
140	0.178E-05	-0.796E 00	0.626E 01	0.193E 01	0.433E 01	0.280		
150	0.	-0.100E 01	0.626E 01	0.	0.626E 01	0.300		

DIAGNOSTIC OUTPUT

Figure 3b. Typical Input-Output Sequence for
Computer Program shown in Figure 3a

LEFT SOLUTION			CURRENTS				
I	PL	DPL	TOTAL	COND	DIFF	Z-MICRONS	
0	0.446E-06	0.100E 01	-0.446E 01	-0.123E 01	-0.323E 01	0.	
10	0.222E-05	0.901E 00	-0.446E 01	-0.270E 01	-0.176E 01	0.020	
20	0.426E-05	0.118E 01	-0.446E 01	-0.263E 01	-0.183E 01	0.040	
30	0.721E-05	0.189E 01	-0.446E 01	-0.176E 01	-0.270E 01	0.060	
40	0.126E-04	0.387E 01	-0.446E 01	0.101E 01	-0.547E 01	0.080	
50	0.254E-04	0.102E 02	-0.446E 01	0.106E 02	-0.151E 02	0.100	
60	0.654E-04	0.350E 02	-0.447E 01	0.566E 02	-0.611E 02	0.120	
70	0.122E-03	0.266E 02	-0.446E 01	0.475E 02	-0.519E 02	0.140	
80	0.187E-03	0.394E 02	-0.446E 01	0.821E 02	-0.865E 02	0.160	
90	0.283E-03	0.584E 02	-0.446E 01	0.142E 03	-0.147E 03	0.180	
100	0.427E-03	0.868E 02	-0.446E 01	0.248E 03	-0.253E 03	0.200	
110	0.640E-03	0.129E 03	-0.446E 01	0.435E 03	-0.440E 03	0.220	
120	0.957E-03	0.193E 03	-0.446E 01	0.764E 03	-0.768E 03	0.240	
130	0.143E-02	0.287E 03	-0.446E 01	0.134E 04	-0.134E 04	0.260	
140	0.214E-02	0.428E 03	-0.446E 01	0.232E 04	-0.233E 04	0.280	
150	0.319E-02	0.639E 03	-0.446E 01	0.400E 04	-0.400E 04	0.300	

DIAGNOSTIC OUTPUT

ZSING(J)
0.12500000E-04

J
1

COLL PROB	Z-MICRONS
0.7800E-03	0.
0.1710E-01	0.0200
0.9098E-01	0.0400
0.2716E 00	0.0600
0.5328E 00	0.0800
0.7640E 00	0.1000
0.8879E 00	0.1200
0.9349E 00	0.1400
0.9624E 00	0.1600
0.9786E 00	0.1800
0.9880E 00	0.2000
0.9935E 00	0.2200
0.9966E 00	0.2400
0.9984E 00	0.2600
0.9994E 00	0.2800
0.1000E 01	0.3000

TOX= 0. MICRONS

GAIN	E-KEV
1.056	1.000
5.393	1.500
24.703	2.000
83.231	2.500
197.585	3.000
351.216	3.500
521.767	4.000
694.839	4.500
864.712	5.000
1189.536	6.000
1494.176	7.000
1784.094	8.000
2164.440	9.000
2337.788	10.000
2505.825	11.000
2570.490	12.000
3132.741	13.000
3493.234	14.000
3651.717	15.000

COLLECTION PROBABILITY
P(z)

GAIN VS BEAM ENERGY
FROM ABOVE P(z)

Figure 3b. Typical Input-Output Sequence for Computer Program shown in Figure 3a (continued)

THIS PAGE IS BEST QUALITY PRACTICABLE
FROM COPY FURNISHED TO DDC

OPTIONS, 1-NEW DATA, 2-QUIT, 3-ELECT&DOPING, 4-NEW SV, 5-OXIDE
 (=5)
 OXIDE THICKNESS IN MICRONS SELECTION OF NON-ZERO TOP OXIDE THICKNESS
 (=0.04)
 TOX= 0.040 MICRONS

GAIN	E-KEV
0.442	2.000
7.013	2.500
42.884	3.000
137.027	3.500
282.981	4.000
454.712	4.500
635.142	5.000
792.294	6.000
1328.309	7.000
1543.871	8.000
1744.342	9.000
2233.426	10.000
2513.879	11.000
2788.472	12.000
3058.774	13.000
3325.889	14.000
3589.892	15.000

GAIN VS BEAM ENERGY
WITH 0.04 MICRON OF TOP OXIDE

OPTIONS, 1-NEW DATA, 2-QUIT, 3-ELECT&DOPING, 4-NEW SV, 5-OXIDE
 (=3)

E V/CM	Z-MICRONS	N-DOPING CM ⁻³	MOBILITY
-0.213E 05	0.	0.453E 18	0.129E 03
-0.156E 05	0.0200	0.198E 19	0.780E 02
-0.992E 04	0.0400	0.549E 19	0.622E 02
-0.425E 04	0.0600	0.968E 19	0.572E 02
0.142E 04	0.0800	0.108E 20	0.565E 02
0.709E 04	0.1000	0.772E 19	0.590E 02
0.128E 05	0.1200	0.349E 19	0.679E 02
0.500E 04	0.1400	0.198E 19	0.781E 02
0.500E 04	0.1600	0.132E 19	0.879E 02
0.500E 04	0.1800	0.688E 18	0.101E 03
0.500E 04	0.2000	0.595E 18	0.116E 03
0.500E 04	0.2200	0.399E 18	0.136E 03
0.500E 04	0.2400	0.267E 18	0.160E 03
0.500E 04	0.2600	0.179E 18	0.187E 03
0.500E 04	0.2800	0.120E 18	0.218E 03
0.500E 04	0.3000	0.805E 17	0.251E 03

DISPLAY OF
ELECTRIC FIELD
DOPING AND MOBILITY

OPTIONS, 1-NEW DATA, 2-QUIT, 3-ELECT&DOPING, 4-NEW SV, 5-OXIDE
 (=2)
 ALL DONE

Figure 3b. Typical Input-Output Sequence for Computer Program shown in Figure 3a (continued)

solution due to Guldberg and Schroter⁽⁴⁾ which was discussed in the first quarter report. Table 2 compares the results of the computer calculation with an evaluation of the exact closed form expression for the collection probability. The built-in electric field was 5×10^3 V/cm and the junction depth 0.5 microns. The surface recombination velocity was 10^7 cm/sec. As can be seen the agreement was exact to at least four significant figures.

TABLE 2

COMPARISON OF COMPUTER RESULTS WITH CLOSED FORM SOLUTION FOR CONSTANT MOBILITY OF $E = 5 \times 10^3$ V/cm.

<u>Z</u>	Constant μ <u>P(Z)-Computer</u>	<u>P(Z)-Closed Form</u>	μ -Doping Depend. <u>P(Z)-Computer</u>
0 μ	0.1667	0.1667	0.0559
0.05	0.6935	0.6935	0.7609
0.1	0.8873	0.8873	0.9387
0.15	0.9585	0.9585	0.9831
0.2	0.9848	0.9848	0.9949
0.4	0.9998	0.9998	0.9999

The last column compares the computer program result for the same case with the mobility dependent on the doping and with a doping at the surface of 10^{19} cm⁻³ and a exponential doping profile to give a constant electric field of 5×10^3 V/cm. As can be seen the results are quite different near the surface indicating the value of including the mobility dependence of doping in the calculation.

During the second quarter the computer model described in the previous section was applied to some As^+ implanted samples. The doping profile used is shown in Figure 4. This is based on data due to Schwettmann for 120 keV As implants at 10^{14} cm^{-2} fluence into $\langle 111 \rangle$ Czochralski silicon annealed at 725°C for 1 hour. In Figure 4 this profile has been scaled to 100 keV ion energy by scaling the depth scale proportional to the energy ratio and adjusting the carrier density to maintain the same total number of ions. The slope of the tail region was kept the same because according to the data of Schwettmann⁽⁵⁾ and Dearnaley⁽⁶⁾ its slope is independent of ion energy. Schwettmann also cites experiments of As implants through 200Å and 600Å of anodic oxide which gave the same tail depth. For the following model calculations, the profile of Figure 4 will be used for implants through any top thermal oxide thickness t_{ox} with the depth scale shifted by t_{ox} .

A following section describes a series of implant experiments using 100 keV As into float zone silicon and annealed at several temperatures. The results from this experiment are compared to the model calculation in Figures 5 through 7. The annealing temperature for all the experiments was 770°C . Figure 5 compares the model calculations to

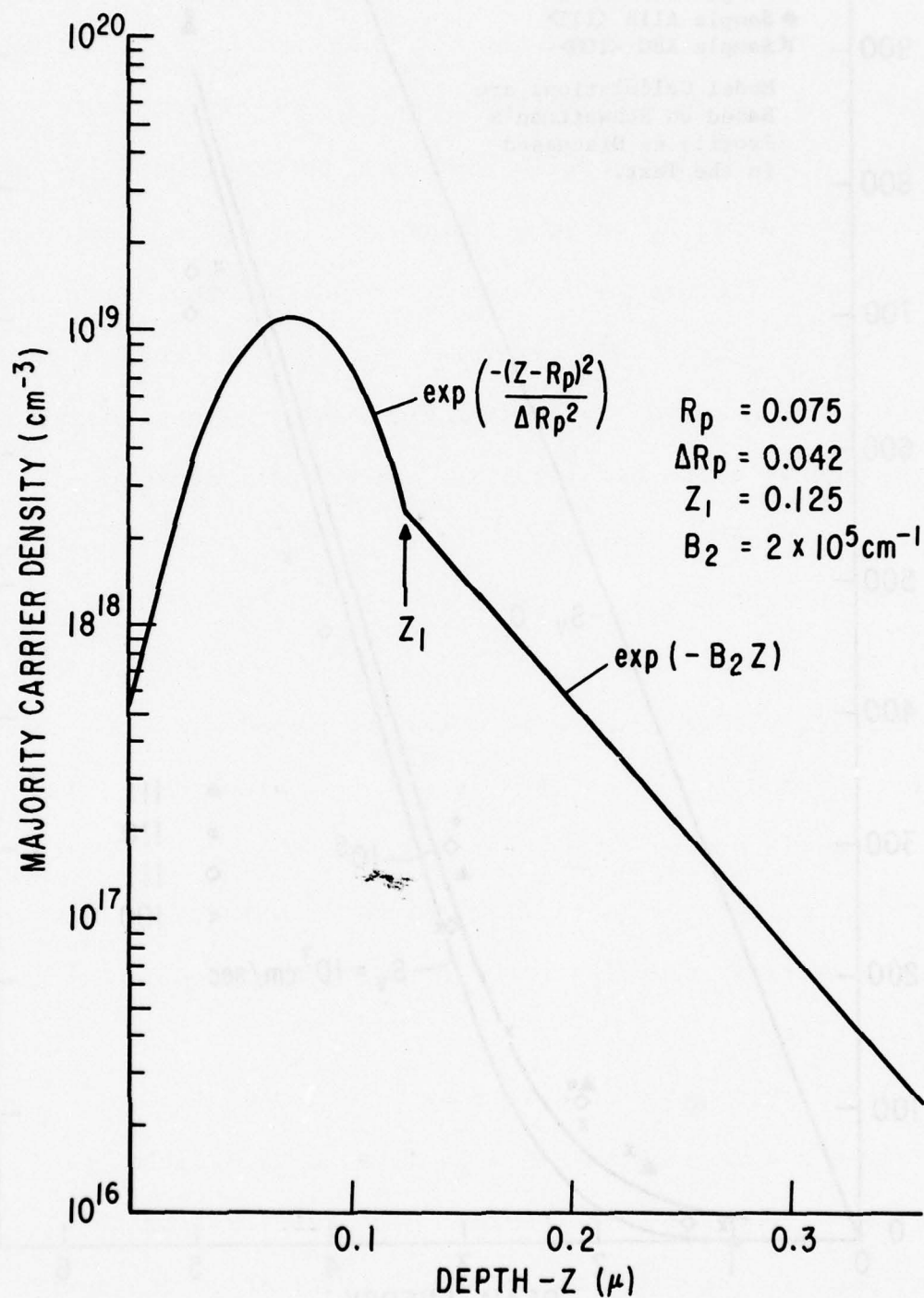


Figure 4. Carrier Density Profile for 100 keV As. Implant at 10^{14} cm^{-2} into $\langle 111 \rangle$ Si After Annealing at 725°C for 1 hr. Based on Schwettmann's Data at 120 keV by Anodic Oxidation and Four-Point Probe (Ref. 5).

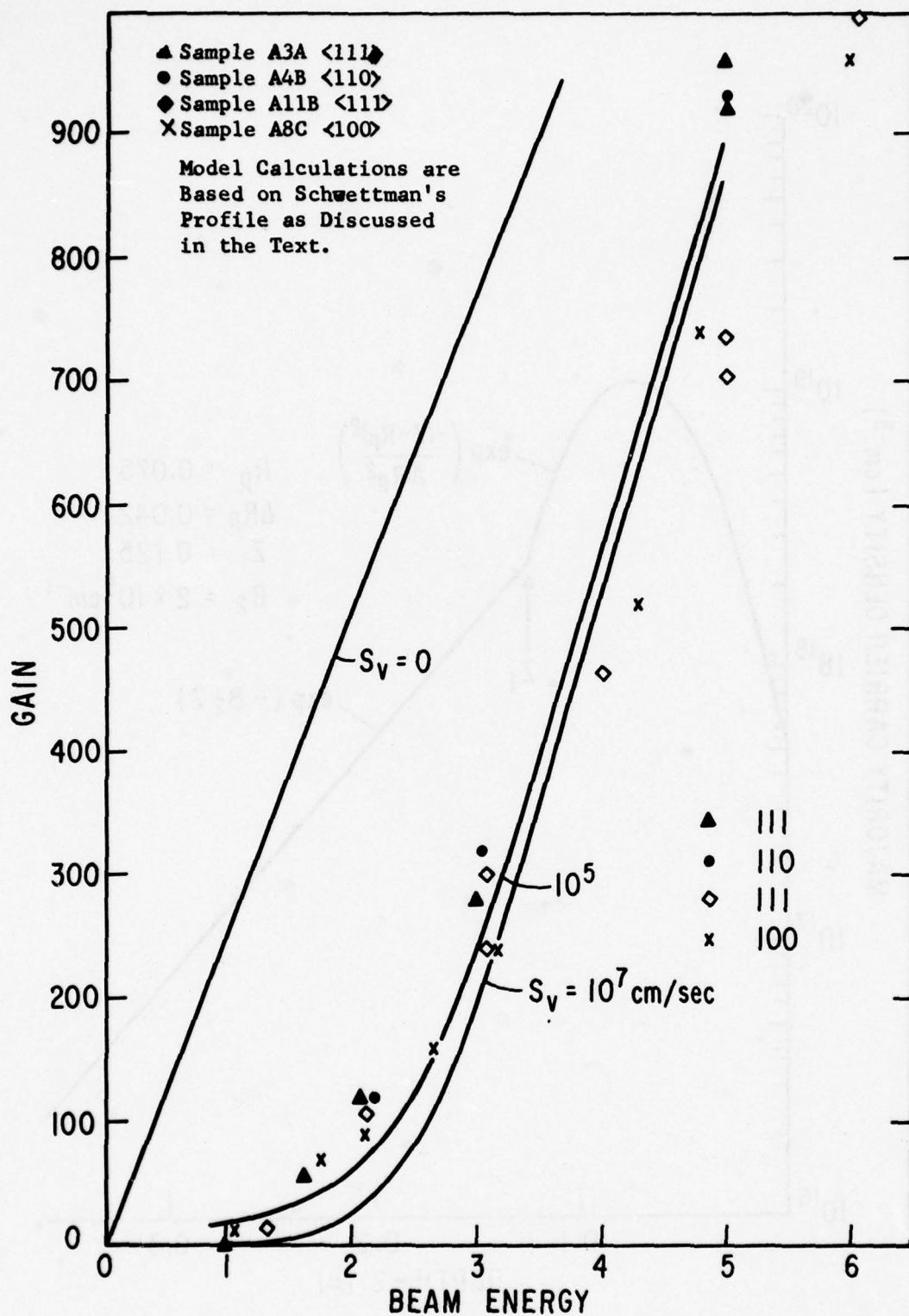


Figure 5. Measured Gain Versus Electron Beam Energy for Four Samples Implanted (100 keV As^+) at 10^{14} cm^{-2} and Annealed at 770°C for 1 hr. in Ar.

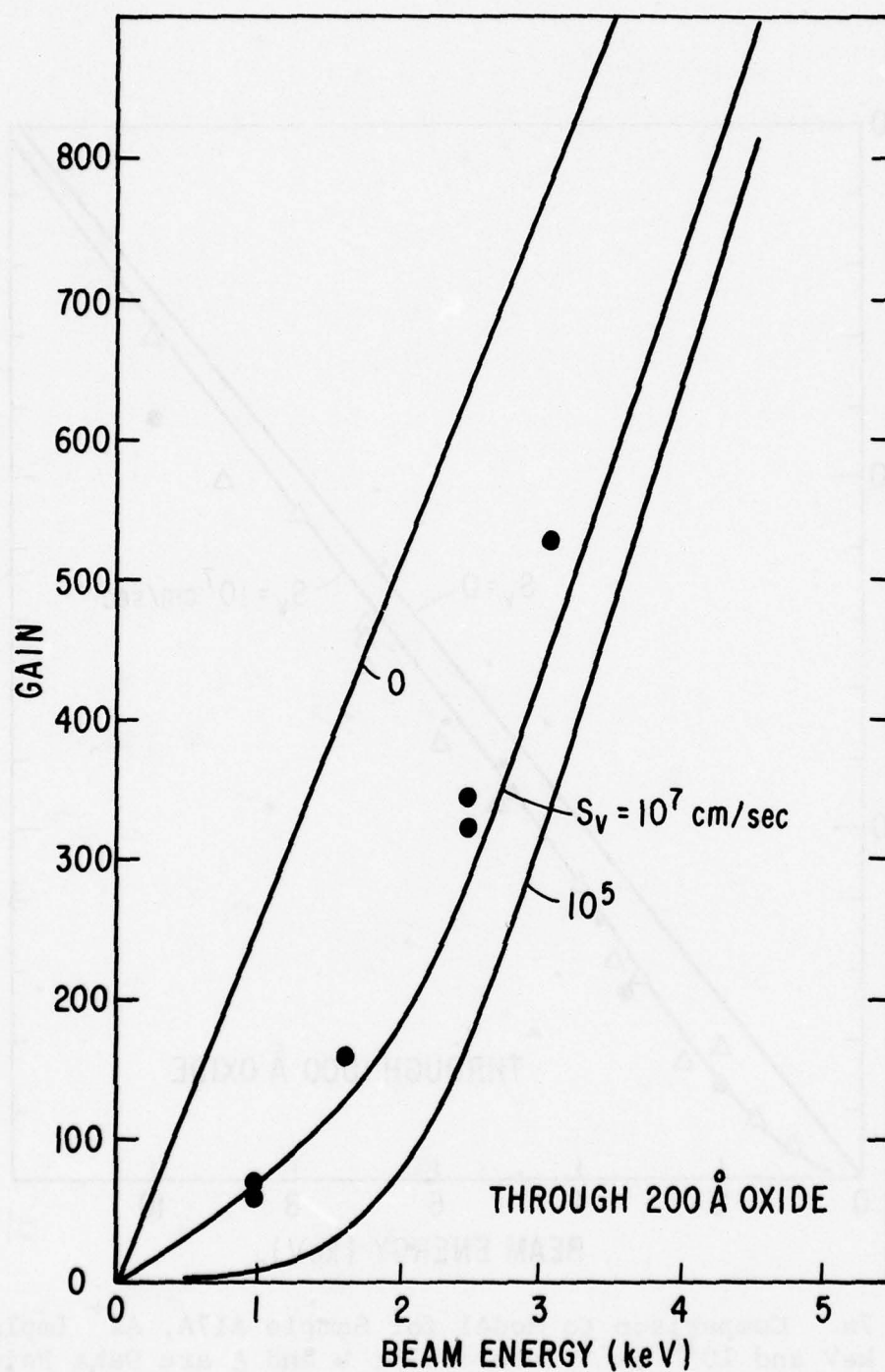


Figure 6. Comparison to Model Calculation for Sample A9C, As^+ Implant at 100 keV and 10^{14} cm^{-2} Through 200 Å of Thermal Oxide into $\langle 111 \rangle$.

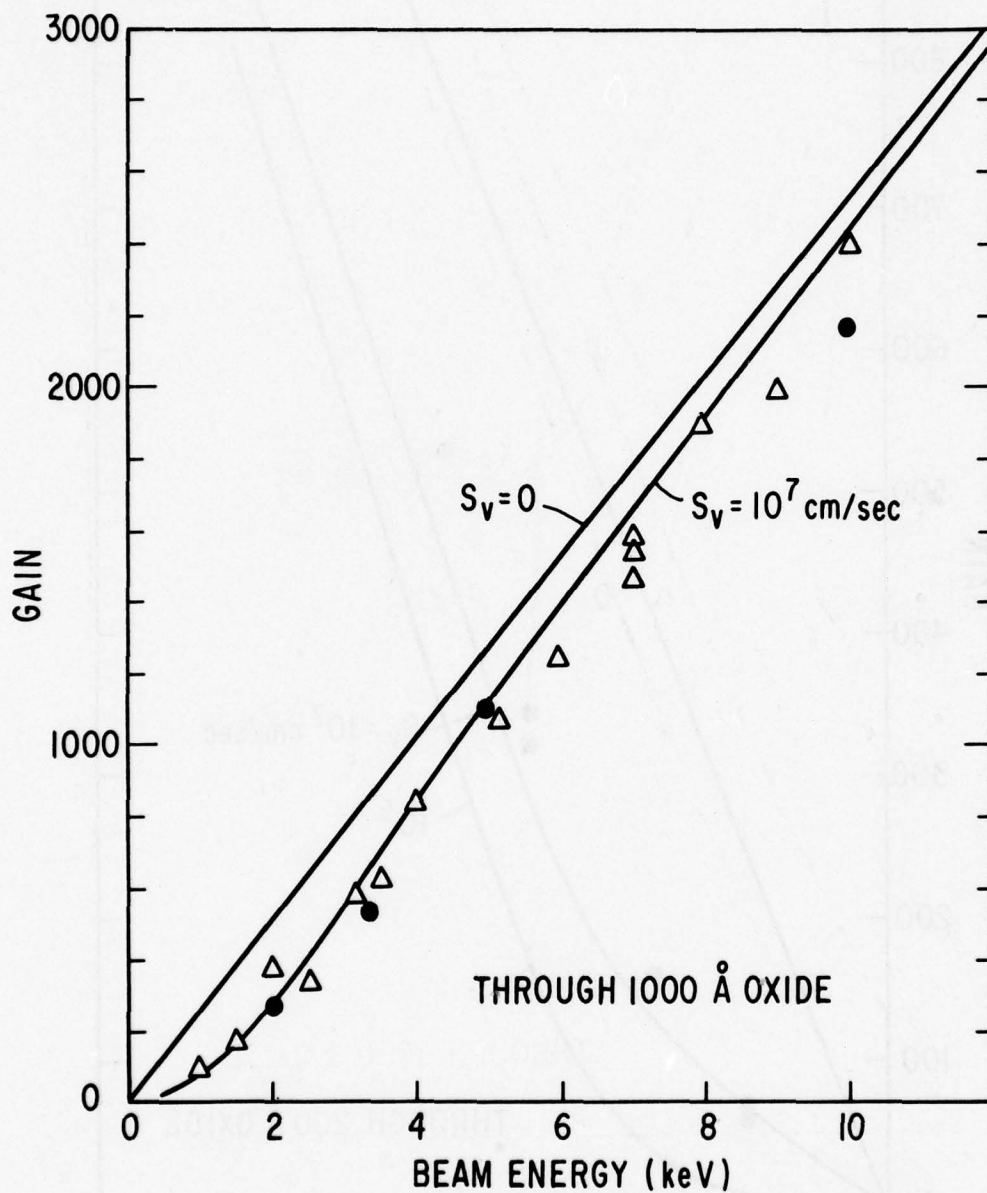


Figure 7a. Comparison to Model for Sample Al7A, As⁺ Implant at 100 keV and 10^{14} cm^{-2} Into $\langle 111 \rangle$; • and Δ are Data Points Measured on Two Different Days.

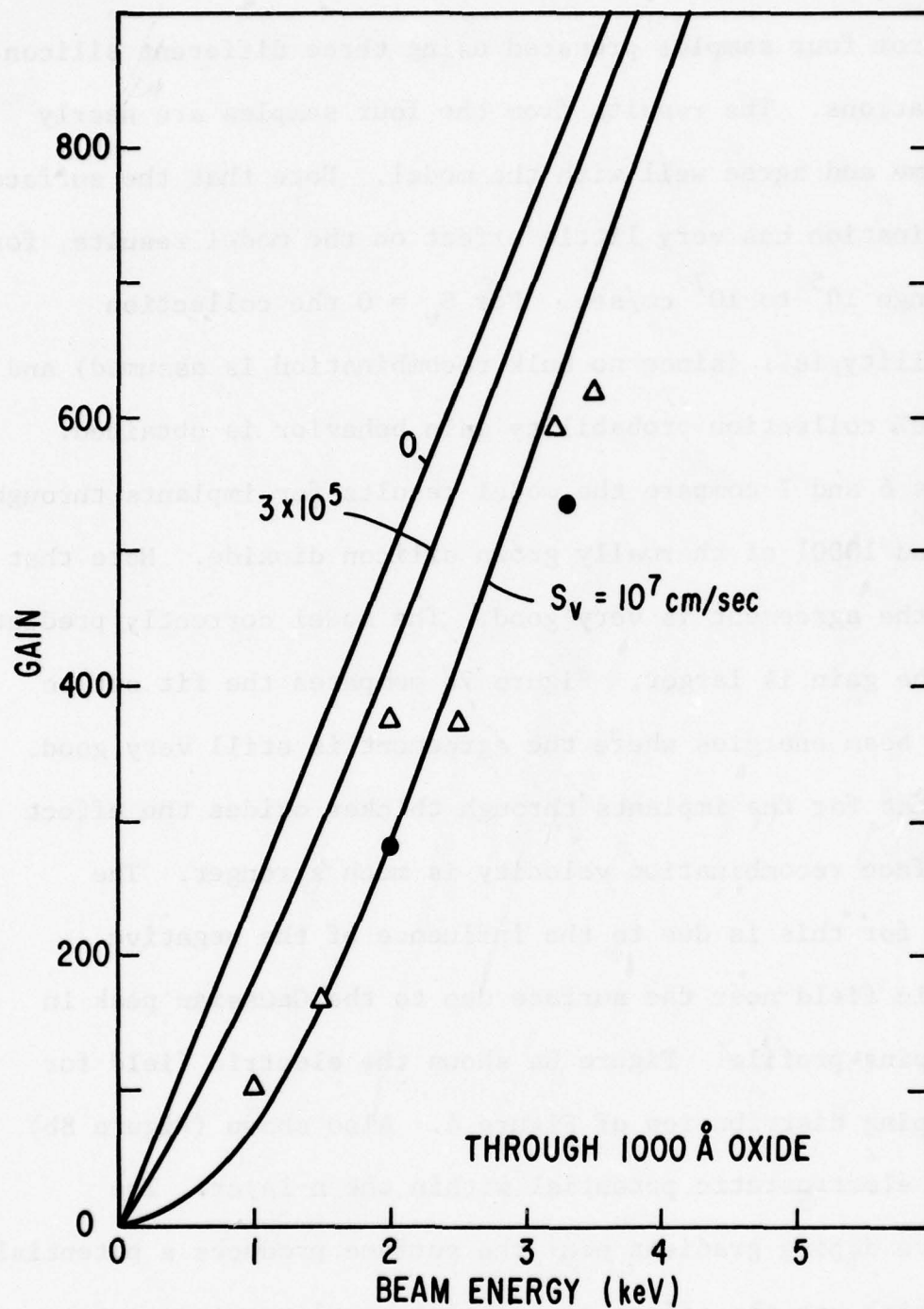


Figure 7b. Comparison to Model for Sample A17A, As⁺ Implant at 100 keV and 10^{14} cm^{-2} Into $\langle 111 \rangle$ (● and Δ are Data Points Measured on Two Different Days).

data from four samples prepared using three different silicon orientations. The results from the four samples are nearly the same and agree well with the model. Note that the surface recombination has very little effect on the model results, for the range 10^5 to 10^7 cm/sec. For $S_v = 0$ the collection probability is 1 (since no bulk recombination is assumed) and the 100% collection probability gain behavior is obtained. Figures 6 and 7 compare the model results for implants through 200Å and 1000Å of thermally grown silicon dioxide. Note that again the agreement is very good. The model correctly predicts that the gain is larger. Figure 7b compares the fit out to higher beam energies where the agreement is still very good. Note that for the implants through thicker oxides the effect of surface recombination velocity is much stronger. The reason for this is due to the influence of the negative electric field near the surface due to the Gaussian peak in the doping profile. Figure 8a shows the electric field for the doping distribution of Figure 4. Also shown (Figure 8b) is the electrostatic potential within the n-layer. The positive doping gradient near the surface produces a potential well which has the effect of trapping carriers near surface. This increases the average residence time near the surface and increases the probability of surface recombination. For this

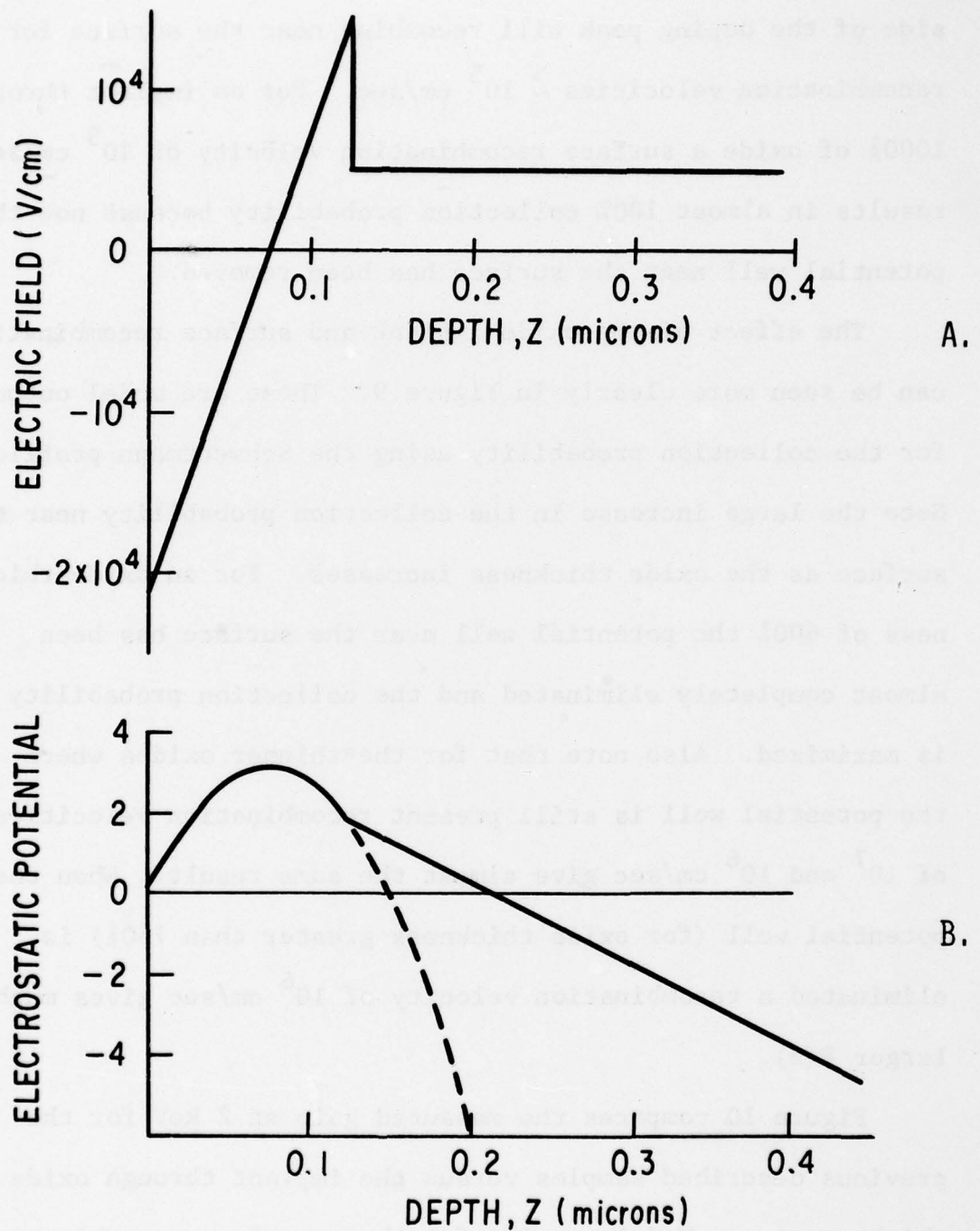


Figure 8. Electric Field and Electrostatic Potential for the Doping Profile of Figure 4 Calculated Using Equation (4)

particular case most of the carriers generated on the surface side of the doping peak will recombine near the surface for recombination velocities $\gtrsim 10^5$ cm/sec. For an implant through 1000Å of oxide a surface recombination velocity of 10^5 cm/sec results in almost 100% collection probability because now the potential well near the surface has been removed.

The effect of the oxide implant and surface recombination can be seen more clearly in Figure 9. These are model outputs for the collection probability using the Schwettmann profiles. Note the large increase in the collection probability near the surface as the oxide thickness increases. For an oxide thickness of 600Å the potential well near the surface has been almost completely eliminated and the collection probability is maximized. Also note that for the thinner oxides where the potential well is still present recombination velocities of 10^7 and 10^6 cm/sec give almost the same result. When the potential well (for oxide thickness greater than 750Å) is eliminated a recombination velocity of 10^6 cm/sec gives much larger $P(z)$.

Figure 10 compares the measured gain at 2 keV for the previous described samples versus the implant through oxide thickness t_{ox} . Model results for three surface recombination velocities are as shown. There is no reason to expect that the

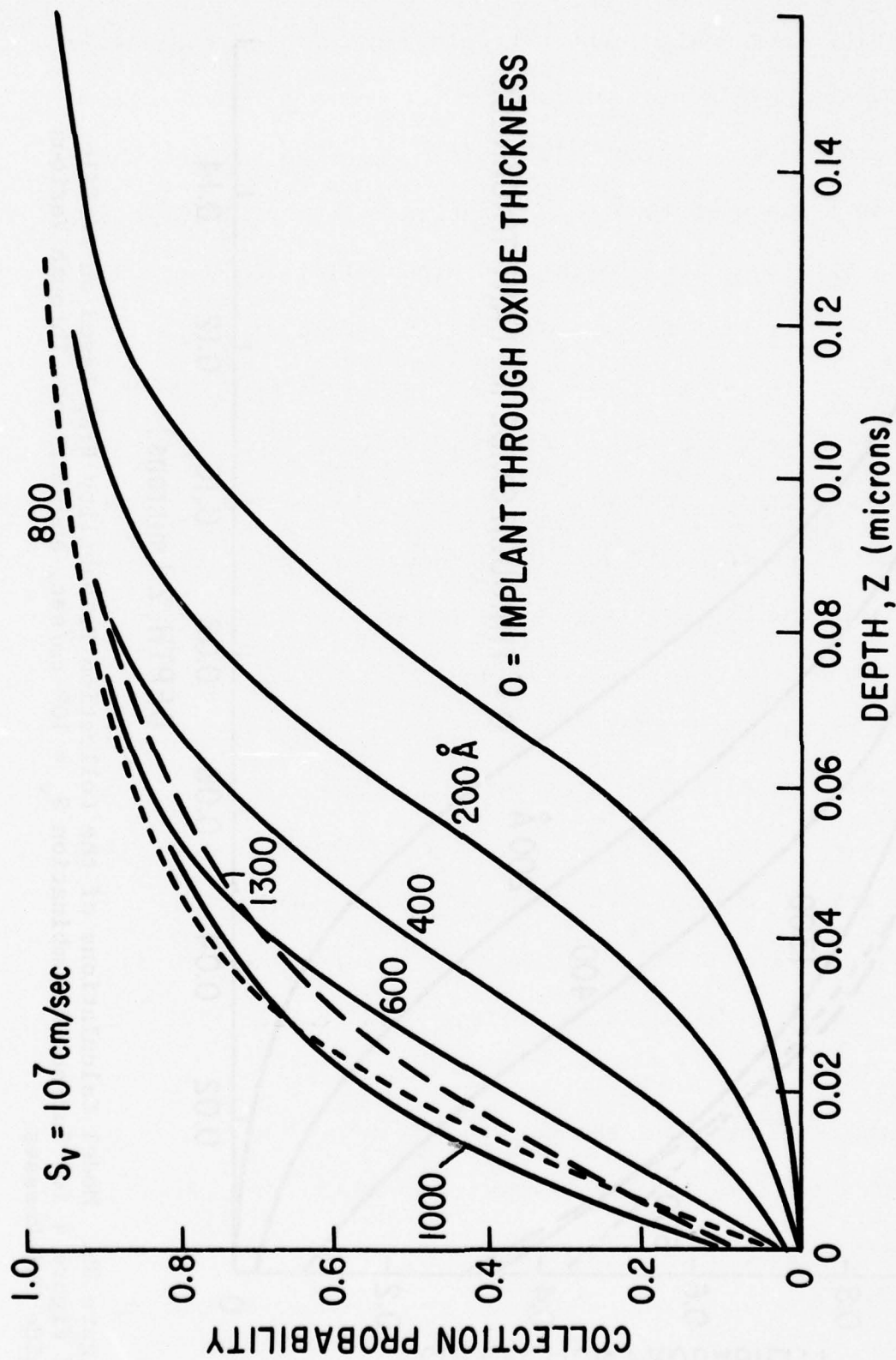


Figure 9a. Model Calculations of the Collection Probability $P(z)$ Based on Profile of Figure 4 for Surface Recombination $S_v = 10^7$ cm/sec, and Implants Through Various Oxide Thicknesses

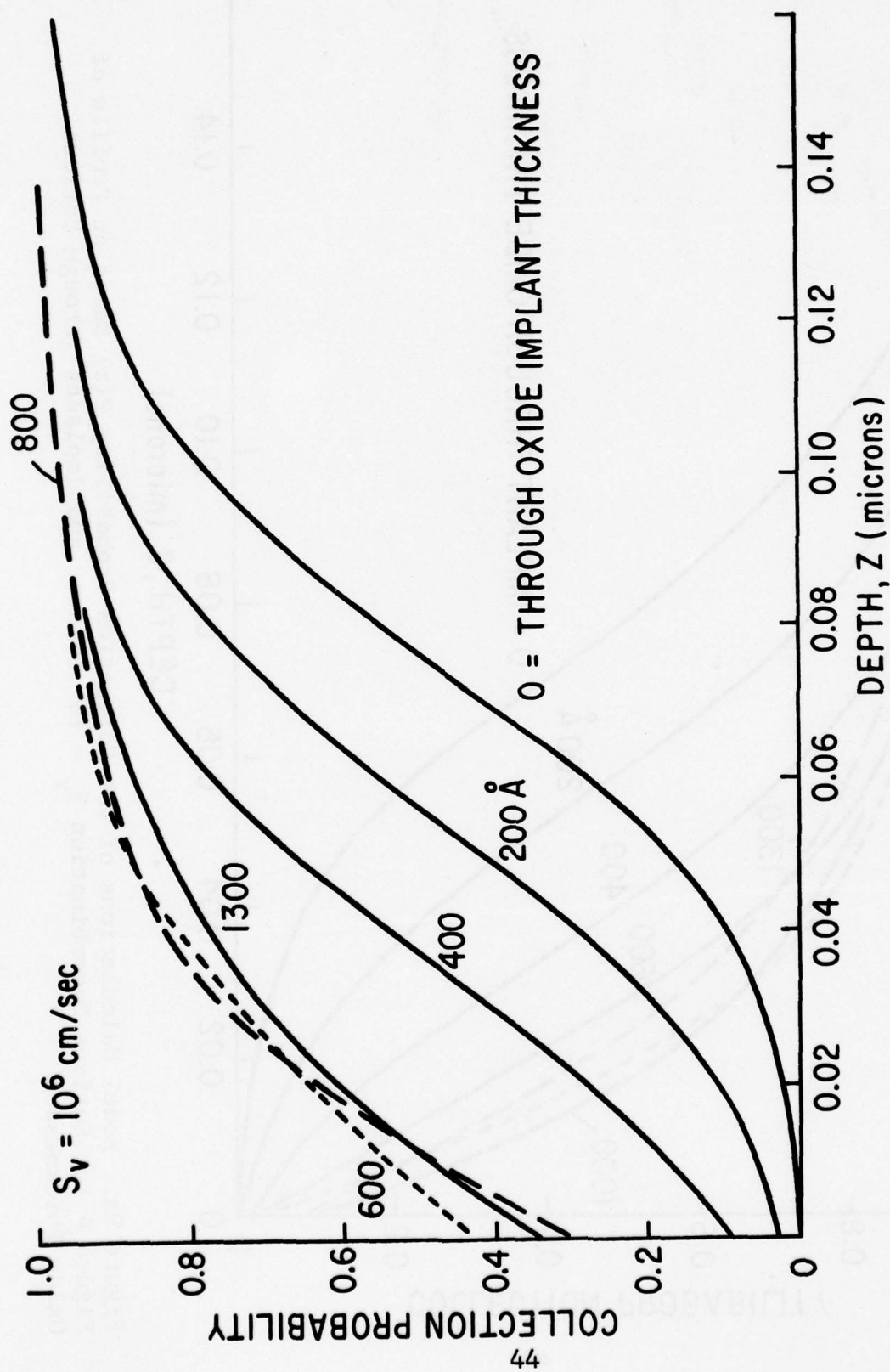


Figure 9b. Model Calculations of the Collection Probability $P(z)$ Based on Profile of Figure 4 for Surface Recombination $S_v = 10^6$ cm/sec, and Implants Through Various Oxide Thicknesses

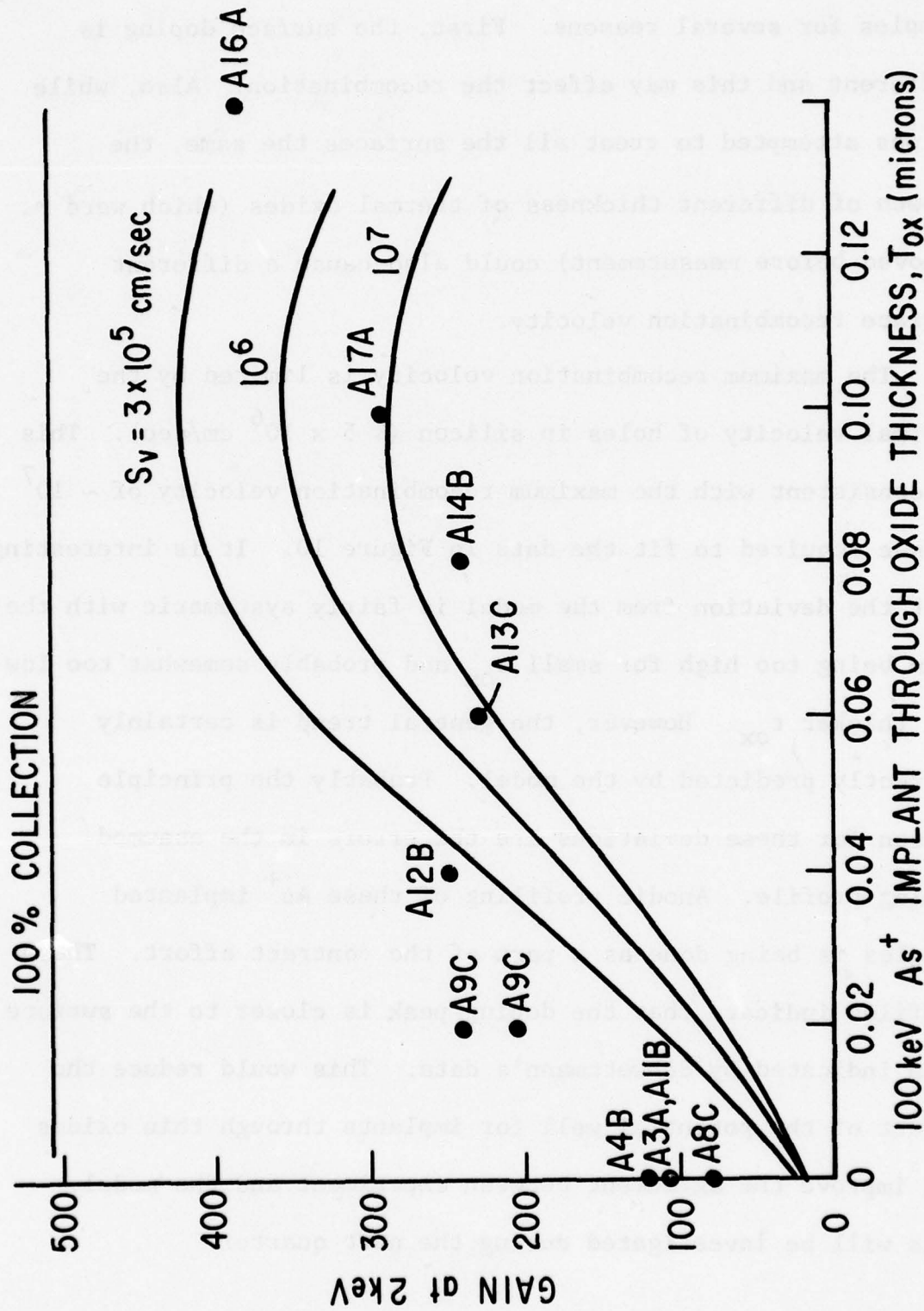


Figure 10. Gain at 2 keV Based on Model Calculation Using Profile of Figure 4 Versus Implant Through Oxide Thickness. Solid Points are Experimental Measurements on Various Samples

recombination velocity should be the same for all these samples for several reasons. First, the surface doping is different and this may affect the recombination. Also, while it was attempted to treat all the surfaces the same, the growth of different thickness of thermal oxides (which were removed before measurement) could also cause a different surface recombination velocity.

The maximum recombination velocity is limited by the thermal velocity of holes in silicon ($\leq 5 \times 10^6$ cm/sec). This is consistent with the maximum recombination velocity of $\sim 10^7$ cm/sec required to fit the data in Figure 10. It is interesting that the deviation from the model is fairly systematic with the gain being too high for small t_{ox} and probably somewhat too low for thicker t_{ox} . However, the general trend is certainly correctly predicted by the model. Probably the principle reason for these deviations are the errors in the assumed doping profile. Anodic profiling of these As^+ implanted samples is being done as a part of the contract effort. These profiles indicate that the doping peak is closer to the surface than indicated by Schwettmann's data. This would reduce the effect of the potential well for implants through thin oxides and improve the agreement between experiment and the model. This will be investigated during the next quarter.

The good agreement between the model and the As^+ implanted samples was obtained without assuming any bulk recombination. It is proposed that with proper processing and choice of the correct annealing temperatures it is possible to produce planar diodes where the effect of bulk recombination near the surface is negligible.

The model can be used to quantify this statement. Figure 11 shows the result of a model calculation using the Schwettmann profiles for implant through 800\AA of oxide. Three curves for the collection probability and gain versus energy are shown. The region between $Z = 0$ and 0.02 microns is assumed to have a minority carrier lifetime of $\tau = \tau_1$ and the rest of the n-layer has $\tau = 0$. One case is for $S_v = 10^7$ cm/sec and $\tau_1 = 0$. This corresponds to the typical cases in the previous discussion where bulk recombination was ignored and the surface recombination velocity was chosen to be large. The other two cases show the effect of introducing recombination near the surface. One curve is for $\tau_1 = 10^{-12}$ sec and $S_v = 10^7$ cm/sec. This corresponds to the first case but with bulk recombination introduced near the surface. The effect on the collection probability is small. The third case is again for $\tau_1 = 10^{-12}$ sec. and $S_v = 0$. If $\tau_1 = 0$, the collection probability would be identically 1. In this case the effect of non-zero bulk recombination is very large. Choosing $\tau_1 = 10^{-11}$ sec produces

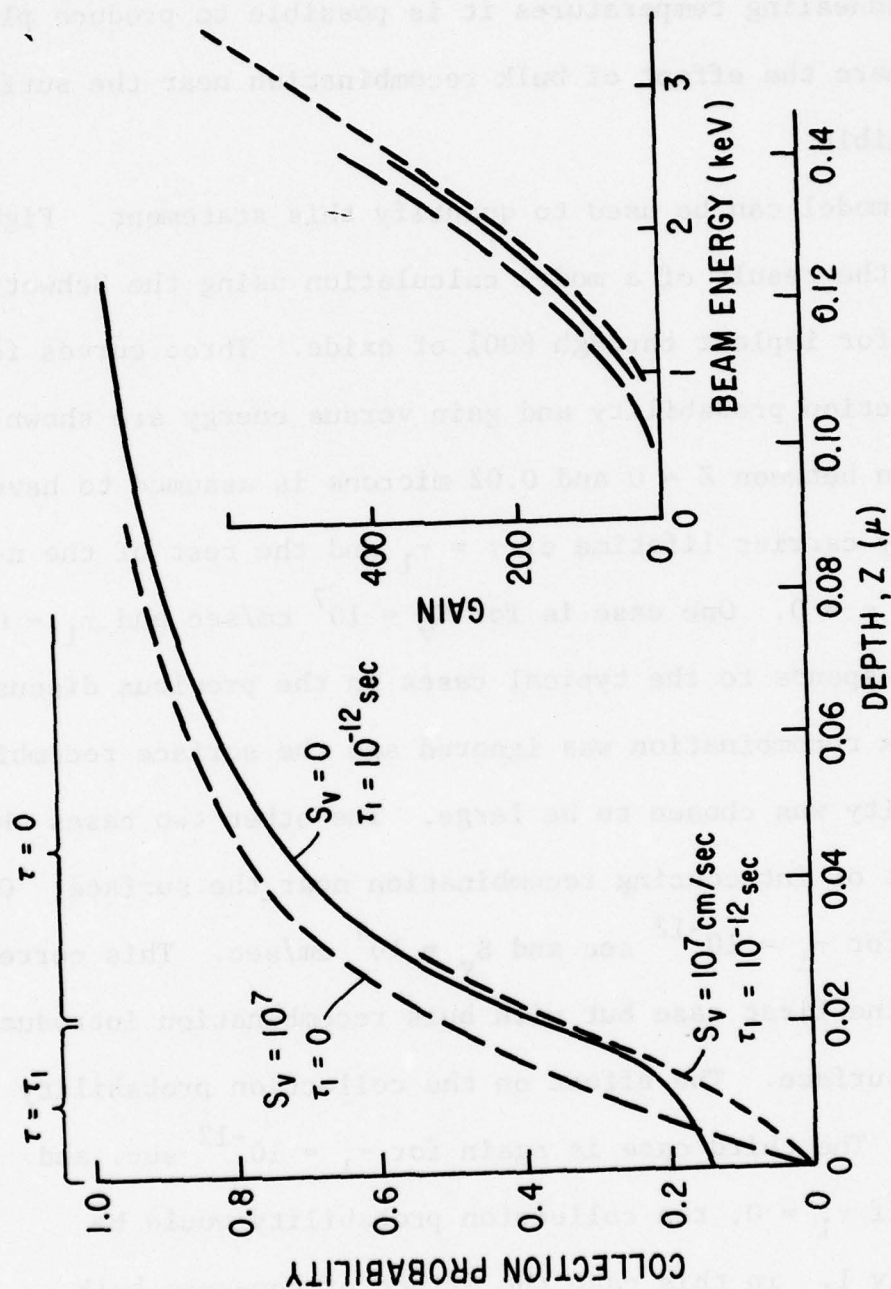


Figure 11. Effect of Bulk Recombination on Collection Probability. Model Calculation of the Collection Probability and the Gain Versus Beam Energy (insert) For Profile of Figure 4 Modified for Implant Through 800 Å of Oxide. Minority Carrier Lifetime is τ_1 for $z < 0.02 \mu\text{m}$ and 0 for $z > 0.02 \mu\text{m}$

only small changes in the collection probability. This determines the amount of bulk recombination that would be required to produce an observable effect. Very high bulk recombination rates ($\sim 10^{-12}$ sec) are required because of the short residence time of the minority carriers near the surface due to the high electric fields and short distance to the collecting diode.

Note that the collection probability and its associated gain versus energy curve is almost indistinguishable between the case $S_v = 10^7$ and $\tau_1 = 0$ and the case $S_v = 0$ and $\tau_1 = 10^{-12}$ sec. This points to the problem of distinguishing the difference between high bulk recombination near the surface and surface recombination from a single set of measurements of gain versus energy, since some distribution of bulk recombination can always be found to fit the data.

A possible way to clearly distinguish between bulk and surface recombination effects on the observed gain versus beam energy curves is to fabricate a BEAMOS-like target⁽⁷⁾ from one of the As^+ implanted samples. The geometry is shown in Figure 12. This sample was fabricated by implanting As^+ through 800Å of thermal oxide and annealing the sample for 1 hour at 770°C in Ar. This is the same process used for all the As^+ samples just described, except that the oxide is normally stripped

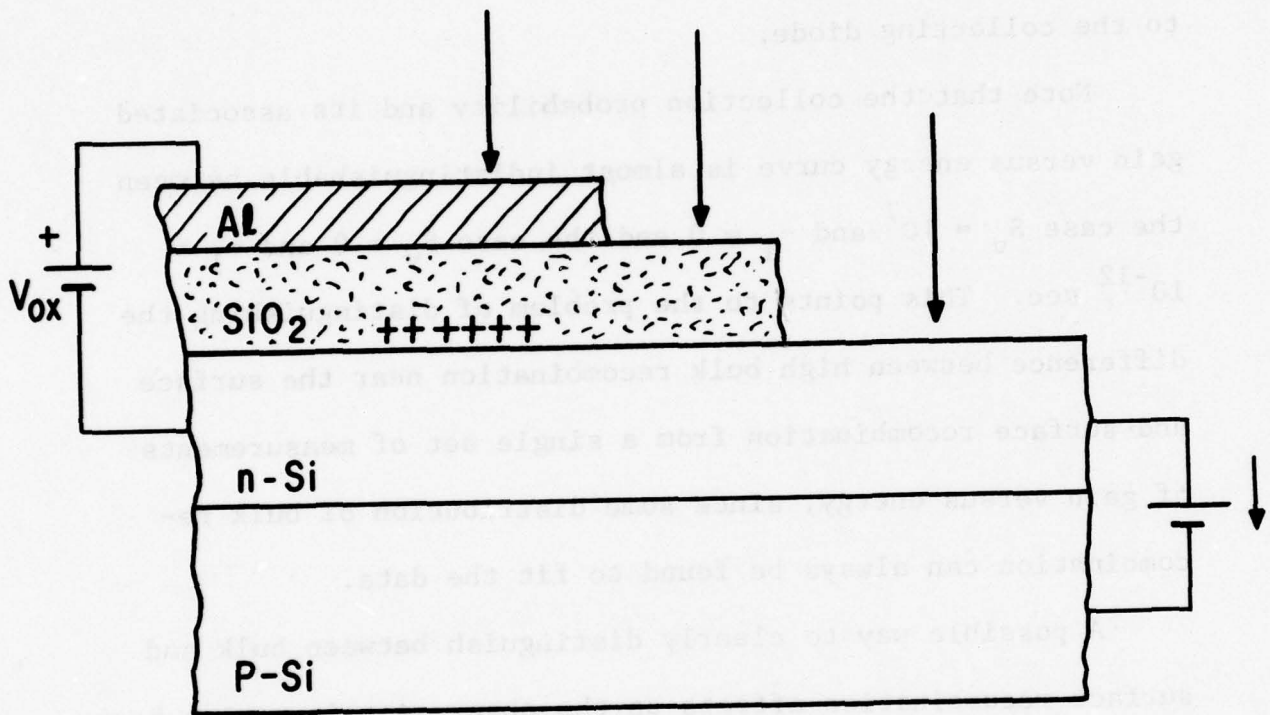


Figure 12. Schematic of Surface Recombination Modulation Experiment

either before anneal or after anneal. (During the first quarter, the order of stripping and annealing was found to make an insignificant difference in the measured gain versus energy curves.) About 400Å of Al was sputter deposited on the oxide and the metallization patterned into small areas, some of which resulted in unshorted MOS capacitors. Such a structure can be operated as a BEAMOS target. By irradiating the MOS structure with positive bias on the Al layer, relative to the silicon, and with an electron beam energy (~ 3 Kev) sufficient to penetrate through the oxide, positive charge will build up in the oxide near the silicon interface. The field due to this charge and the applied bias is known to be in excess of 5×10^6 V/cm with the metal bias still applied. This field produces a large reduction in the surface recombination velocity. BEAMOS targets have an oxide thickness of 2800Å and an n-layer doping of $\sim 10^{16}$ cm⁻³. Measurements on BEAMOS targets show that the surface recombination velocity varies between $\sim 4 \times 10^3$ cm/sec and $\sim 4 \times 10^6$ cm/sec between the maximum stored charge state and the minimum field state (which occurs for negative bias irradiation). While the exact range of modulated surface recombination is not known for the thinner oxide thickness and higher doping level in this experiment, it would be expected that the modulation would still be very

large, at least between 10^4 and 10^6 cm/sec.

Figure 13 shows the experimental results. Again Schwettmann's profiles were used, modified for implant through 800Å of oxide. Three sets of curves are shown for a top oxide thickness of 0, 0.06 and 0.11 microns. These correspond to the electron beam impinging on areas with no top oxide, where there is oxide only and where there is oxide and metal. The thicknesses chosen were adjusted slightly to provide a better fit with the model. There is some deviation from the model at the higher beam energies where the beam is penetrating past the diode junction. This is probably due to recombination in the diode depletion region or in the p side of the diode. This has been noticed on several samples and will be discussed later.

The (▲) points are the gain versus energy data for the area with no oxide. The fit is reasonably good at least at the low beam energies. The (●) points are for the area with just oxide and again the fit is reasonably good although the oxide thickness was chosen slightly thinner than indicated by the processed oxide thickness. The ■ and □ points are the gain versus energy for the complete structure with an Al and oxide layer. The ■ points are for irradiation with -10 volts on the Al and the □ points are for +10 volts on the Al. The

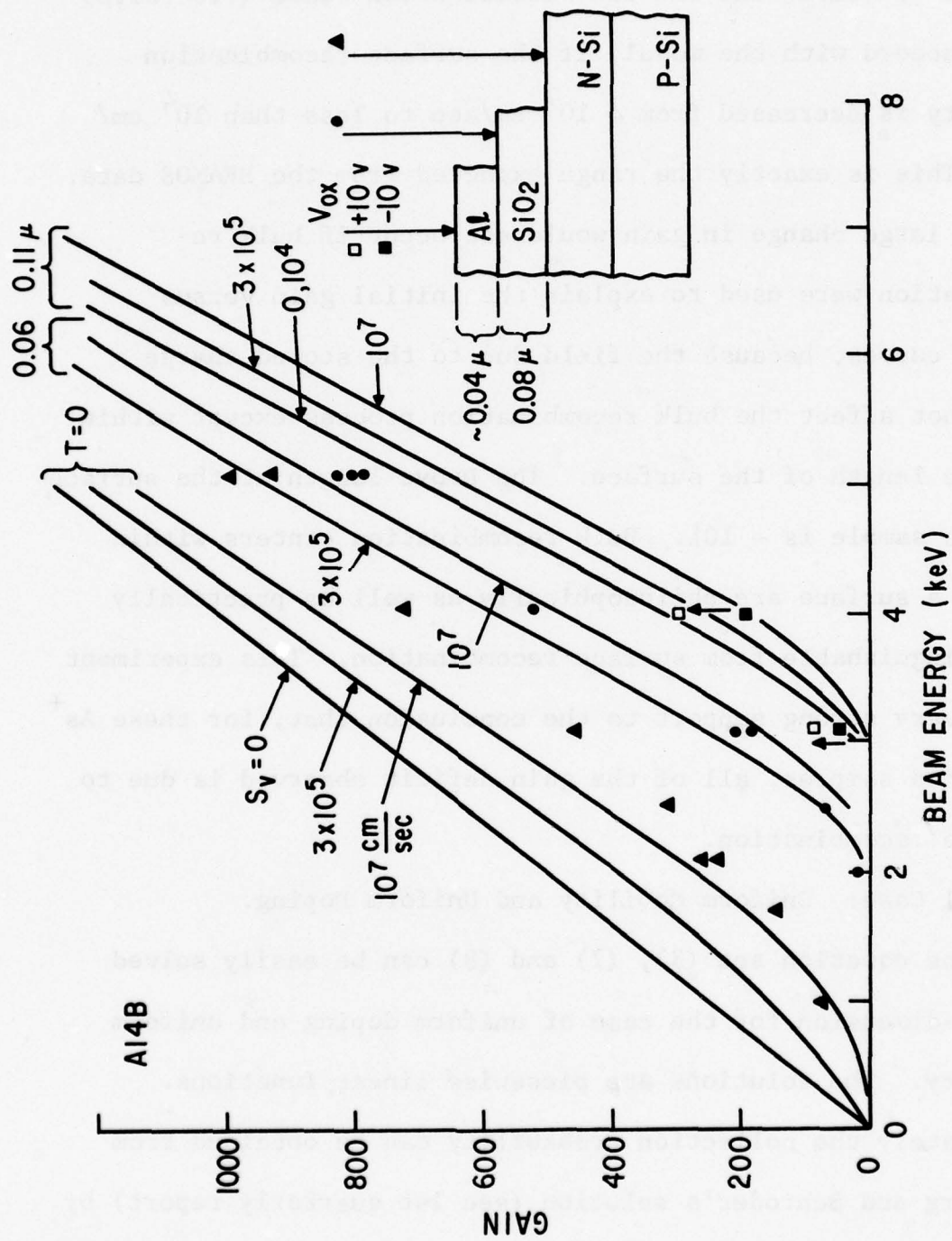


Figure 13. Model Calculations and Experimental Results for Surface Recombination Velocity Modulation Experiment

agreement with the model, especially at 4 keV is very good. The amount of gain increase between the high recombination state (-10 volts) and the low recombination state (+10 volts) is in accord with the model, if the surface recombination velocity is decreased from $\sim 10^7$ cm/sec to less than 10^4 cm/sec. This is exactly the range expected from the BEAMOS data. Such a large change in gain would not occur if bulk recombination were used to explain the initial gain versus energy curves, because the field due to the stored charge would not affect the bulk recombination process except within a Debye length of the surface. The Debye length at the surface of this sample is $\sim 10\text{\AA}$. Bulk recombination centers within 10\AA of a surface are philosophically as well as practically indistinguishable from surface recombination. This experiment lends very strong support to the conclusion that, for these As^+ implanted samples, all of the gain deficit observed is due to surface recombination.

Special Case: Uniform Mobility and Uniform Doping.

The equation set (3), (7) and (8) can be easily solved in one-dimension for the case of uniform doping and uniform mobility. The solutions are piecewise linear functions. Alternately the collection probability can be obtained from Guldberg and Schroder's solution (see 1st quarterly report) by

taking the limit of zero electric field. The collection probability is:

$$P(Z) = \begin{cases} 1 + (\frac{S_v}{D})Z & Z \leq W \\ 1 + (\frac{S_v}{D})W & Z \geq W \end{cases} \quad (25)$$

$$D = (KT/q_e)\mu \quad Z \geq W$$

where again bulk recombination in the n and p layers is being ignored. Because the collection probability is linear in Z, the integration of Equation (25) and (12) has a very simple form if the electron beam generation $g(Z, E_B)$ is negligible zero for $Z > W$. In this case the gain can be written as:

$$\frac{\text{Gain}}{G_M} = \frac{1 + (\frac{S_v}{D})T^A}{1 + \frac{S_v}{D}W} \quad (26)$$

$$G_M = \frac{1}{e_i} \int_0^W dz g(z + T_{ox}, F_B) \quad (27)$$

where:

$$T^A = \int_0^W zg(z, E_B) dz / \int_0^W g(z, E_B) dz \quad (28)$$

T^A is the average penetration of the beam penetration (centroid of the electron hole pair generation distribution

in the n-layer). ($S_V = 0$). The dependence of T^A and G_M on the oxide thickness T_{ox} is shown in Figures 14 and 15.

As an example of the application of this solution consider the geometry in Figure 16. This corresponds to the structure used in some of the alloy writing experiments. The region between $Z = 0$ and $Z = -T_D$ is assumed to be an electrically inactive region due to the writing process so that carriers generated in this region by the electron beam do not contribute to the diode signal. This region could be composed of a layer of deposited metal or a region of semiconductor damaged by the writing process (e.g. heavily alloyed with metal) or a combination of both. Normally the recombination velocity at $Z = 0$ is taken to be $\sim 10^6$ cm/sec since the metal/silicon interface will usually have high surface recombination. Using Equations (26) through (28) it is possible to construct curves of electron beam gain versus beam energy for various thicknesses T_D . The junction depth W is normally determined from the best fit to the model in a region where T_D is known, e.g. an unwritten region with just a deposited metal or a region where the metal has been stripped. If the varying T_D is due to some writing process which consumes silicon, then it is necessary to hold $W + T_D$ constant rather than W constant. Normally $W \gg T_D$ so this correction is not

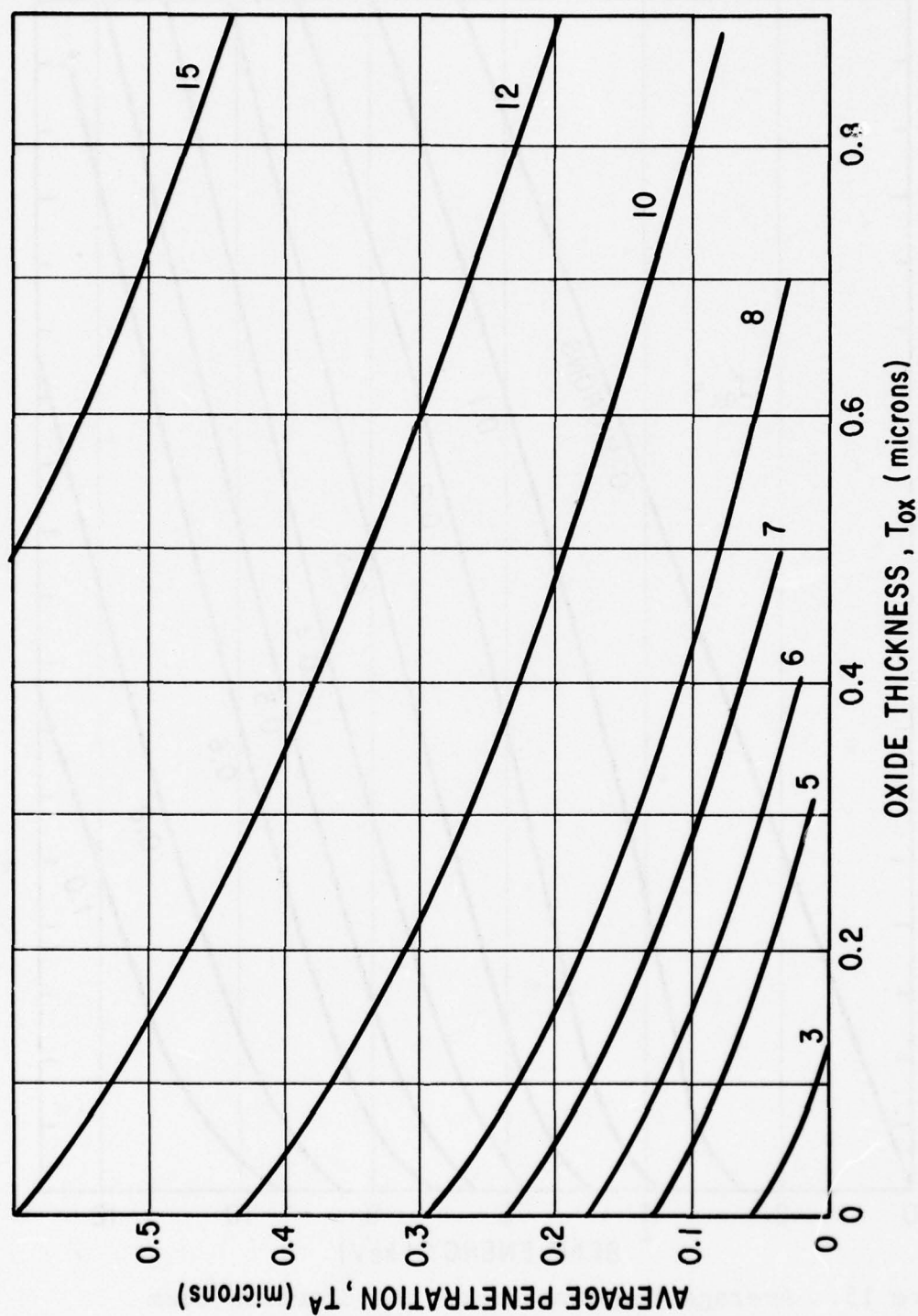


Figure 14. Maximum Gain versus Beam Energy and Oxide Thickness Based on Equation (27)

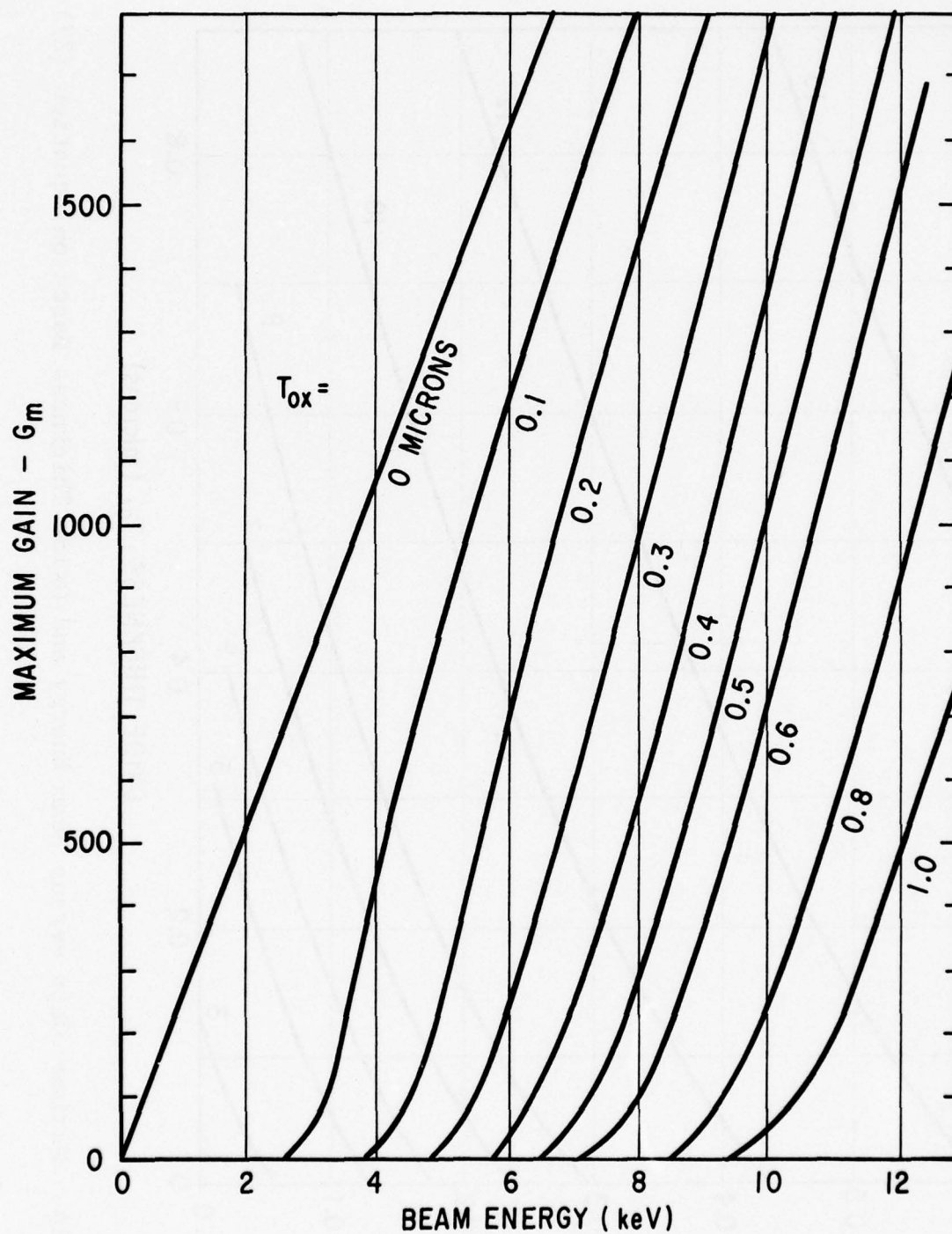


Figure 15. Average Penetration of the Electron Beam in Silicon vs. Oxide Thickness and Beam Energy

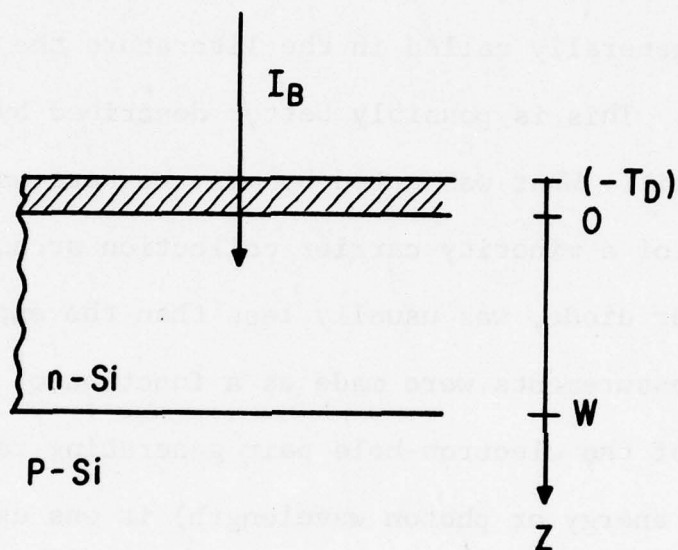


Figure 16. Schematic of Sample Geometry for Typical Application of Uniform Doping and Mobility Model to Alloy Writing Experiments

required. Figure 17 shows such a set of curves for a sample where the junction depth $W = 2.8$ microns, which is appropriate for most of the samples used for the alloy junction writing experiments.

Comparison to Other Work

The question that has been addressed in this section is what has been generally called in the literature the "dead-layer" problem. This is possibly better described by the term gain deficit. What was noted by many workers was that the signal out of a minority carrier collection structure, such as a planar diode, was usually less than the expected ideal. When measurements were made as a function of penetration depth of the electron-hole pair generating radiation (electron beam energy or photon wavelength) it was usually found that the results could be explained by the concept of a region near the surface which was not contributing to the signal, i.e., a "dead-layer". While it is often possible to fit experimental data by this simple assumption, this is no guarantee that this is the correct explanation. Some of the experimental structures reported on by the early investigators used heavy P diffusion to produce doping gradients near the surface. Since P diffusion is known to produce damage⁽⁸⁾ in the surface region, it is quite possible that the dead-layer

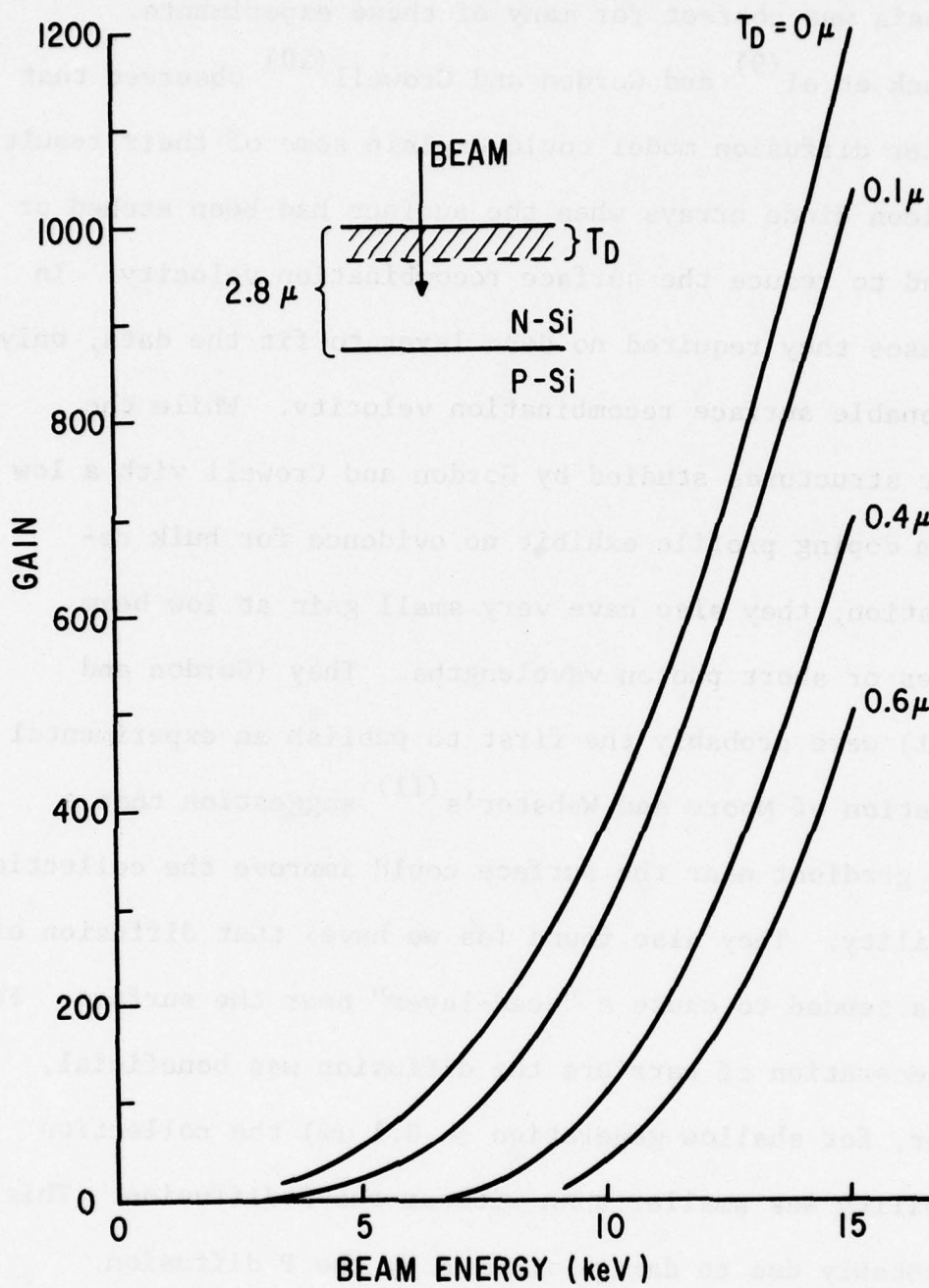


Figure 17. Dependence of Gain on Beam Energy for $S_v 10^7$ cm/sec for Various Damaged Depths T_D based on Model of Figure 16 and Equations (26) through (28)

hypothesis was correct for many of these experiments.

Buck et al⁽⁹⁾ and Gordon and Crowell⁽¹⁰⁾ observed that a carrier diffusion model could explain some of their results on silicon diode arrays when the surface had been etched or oxidized to reduce the surface recombination velocity. In some cases they required no dead layer to fit the data, only a reasonable surface recombination velocity. While the simpler structures studied by Gordon and Crowell with a low uniform doping profile exhibit no evidence for bulk recombination, they also have very small gain at low beam energies or short photon wavelengths. They (Gordon and Crowell) were probably the first to publish an experimental realization of Moore and Webster's⁽¹¹⁾ suggestion that a doping gradient near the surface could improve the collection probability. They also found (as we have) that diffusion of dopants tended to cause a "dead-layer" near the surface. For deep generation of carriers the diffusion was beneficial, however, for shallow generation ($\sim 0.1 \mu\text{m}$) the collection probability was smaller than without the P diffusion. This was probably due to damage induced by the P diffusion.

Buck et al also observed that for their lightly doped N-type material surface inversion could occur causing a depletion layer depth of $\sim 1 \mu\text{m}$. This explained the very thick

"dead-layers" ($\sim 1 \mu\text{m}$) they sometimes observed before P diffusion. These "dead-layers" were dependent on surface treatment; for example a HF etch which could eliminate the surface inversion.

Attempts at the analysis of the effect of the P diffusion by Buck, et al, consisted of continuing to assume a thin "dead-layer" (typically $\sim 0.1 \mu\text{m}$) and assigning a small effective surface recombination velocity to a phantom surface at the boundary of the "dead-layer" with the bulk material. Guldberg and Schroter⁽³⁾ attempted a more sophisticated analysis which included the effect of the built-in electric field past the "dead-layer" and assigned a large surface recombination to the same phantom surface. The result of this analysis essentially showed that the small effective surface recombination velocity assumed by Buck, et al, and Gordon and Crowell was due to the effect of the built-in electric field.

While the analysis used by Guldberg and Schroter was more sophisticated than previous work they still concluded that "dead-layers" were required to explain their experimental results. Even when the heavily doped region near the surface was stripped, they concluded that about a 400\AA thick "dead-layer" was required to fit the data. This, they concluded, was

the minimum "dead-layer" for a real silicon surface. This does not seem sensible and contradicts the results of Buck, et al, for more lightly doped n-material.

The results of our analysis show that for As^+ implanted samples, properly annealed, there is no "dead-layer", i.e., no region of very high bulk recombination near the surface. We have found for As^+ implanted samples with surface concentrations of $\sim 10^{19} \text{ cm}^{-3}$ that the gain deficit observed can be explained by surface recombination coupled with solutions of the carrier continuity equation which include the effects of doping gradients, dependence of mobility on doping, and the correct electron beam carrier generation profile. This conclusion was further supported by the experiment using surface recombination velocity modulation due to charge buildup in an overlying oxide. (BEAMOS-like structure) This experiment clearly demonstrated that the effect of surface recombination velocity on the gain deficit was as predicted by the model. We believe this to be the first demonstration that n^+ layers can be produced which maximize the readout signal or gain from planar diode structures without invoking a "dead-layer" hypothesis to explain the reduced gain at low beam energies.

Future Plans

Similar one-dimensional modeling will be applied to the P^+ implanted samples, which were described in the planar diode experiments section. The As^+ data will be analyzed further using the As profiles obtained by anodic oxidation and 4-point probe measurements. Preliminary indications are that this will provide an even better fit to the data. These results will probably further substantiate the validity of the model assumptions. Assuming this is the case, the model can be used to analyze and design further experiments related to the writing process.

The model, as it now stands, is well suited to studying damage writing by ion beams and alloy writing. These applications will be further pursued. The model can also be used to provide insight into the two-dimensional carrier diffusion equations for application to the bit packing density problem, by analysis of the field driven and diffusion driven components of the particle current. This application will be further explored.

SECTION III

FABRICATION OF PLANAR DIODES

The planar diode studies initiated during the first quarter were continued. Both P^+ and As^+ implants were studied. Tables 3 and 4 summarize the additional samples which were evaluated in the SEM.

Modeling studies and early As^+ implant work indicated that moving the implanted ion distribution peak near the surface would increase the gain (reduce the "dead-layer"). This peak can be moved near the surface by implantation through an oxide layer.

The starting material for these experiments was $\langle 111 \rangle$ orientation Boron-doped float zone silicon wafers with resistivity between 10 and 20 ohm-cm. Dry thermal oxides were grown at $1100^\circ C$ over a range of thicknesses between 400\AA and 1400\AA . These were implanted at 100 keV with As^+ at a fluence of 10^{14} cm^{-2} . As can be seen from Table 3 implants through $\sim 1000\text{\AA}$ of oxide produces planar diodes with gains of 400 to 500 at 2.5 keV. This is 70% of the maximum possible gain at this beam energy and corresponds to an equivalent dead-layer of $\sim 200\text{\AA}$. As discussed in Section II this is not an actual thickness of damaged material but is a gain deficit due

TABLE 3

SUMMARY OF PLANAR DIODE EXPERIMENTS FOR 100 keV,
 10^{14} CM $^{-2}$ As $^{+}$ IMPLANTS INTO < 111 >, FZ, 10-20 μ -CM
 P-TYPE Si. ALL ANNEALS WERE IN Ar AT 770°C FOR 1 HR.

Sample Number	Surface Prep.	Anneal Conditions	Gain at 2.5 keV	(T _D)	5 keV	(T _D)
A11B	-	770°C 1 hr.	160	540Å	740	1000Å
A12B	400Å oxide before implant	770°C 1 hr.	320	360Å	830	900Å
A13C	600Å oxide before implant	770°C 1 hr.	290	400Å	870	840Å
A14B	800Å oxide before implant	770°C 1 hr.	350	330Å	950	700Å
A17A	1000Å oxide before implant	770°C 1 hr.	400	280Å	1100	440Å
A16A	1200Å oxide before implant	770°C 1 hr.	500	180Å	1100	440Å
A39C	-	770°C 1 hr.	160	540Å	880	920Å

TABLE 4

SUMMARY OF PLANAR DIODE EXPERIMENTS FOR 100 keV,
 $10^{14} \text{ CM}^{-2} \text{ P}^+$ IMPLANTS INTO $\langle 111 \rangle$, FZ 10-20 μ -CM
 P-TYPE Si.* ANNEALS WERE PERFORMED IN Ar ATMOSPHERE

Sample Number	Surface Prep.	Anneal Conditions	Gain at 2.5 keV	(T_D)	5 keV	(T_D)
P16A	1600Å oxide before implant	770°C 1 hr.	NE		NE	
P17A	1800Å oxide before implant	770°C 1 hr.	350	330Å	950	720Å
P18C*	-	770°C 1 hr.	110	620Å	400	1640Å
P22B	-	770°C 1 hr.	100	630Å	470	1500Å
P23B	1180Å oxide after implant	-	125	590Å	640	1200Å
P25B	2730Å oxide after implant	-	NE		NE	
P26B	3665Å oxide after implant	-	90	650Å	500	1440Å
P27	1800Å oxide after implant	-	NE		NE	
P28B	4290Å oxide after implant	-	110	620Å	570	1300Å

* P18 was 400 μ -cm $\langle 111 \rangle$ p-type Si

to carrier diffusion towards the silicon surface. Figure 18 shows the gain versus beam energy data for one of the better As^+ samples. During the next quarter 100 keV As^+ implants through 800Å of thermal oxide will be used for most experiments both for ion implant and alloy junction writing.

Table 4 summarizes some additional P implant experiments. These experiments were not actively pursued because of the success with the As^+ implants. In addition, P^+ implants can show undesirably deep tailing in the profiles. On several samples, oxide growth after implant was attempted. It was thought that this might reduce the "dead-layer" effects by removing damaged silicon near the surface or annealing out the damage due to the high temperature oxide growth conditions. As can be seen from Table 4 the results were not encouraging. This approach is not now expected to be useful because the modeling studies indicate that surface damage is not important in controlling the low voltage gain in these targets.

Just as for the As^+ implanted samples, the best results for phosphorus implants were obtained by implanting through oxide layers. See, for example, sample P17A in Table 4 and samples P9, 10 and 11 in the first interim report. Figures 19 and 20 show typical gain versus beam energy measurements for two of the P^+ implanted samples. Most of the measurements for the As samples are included in the modeling section

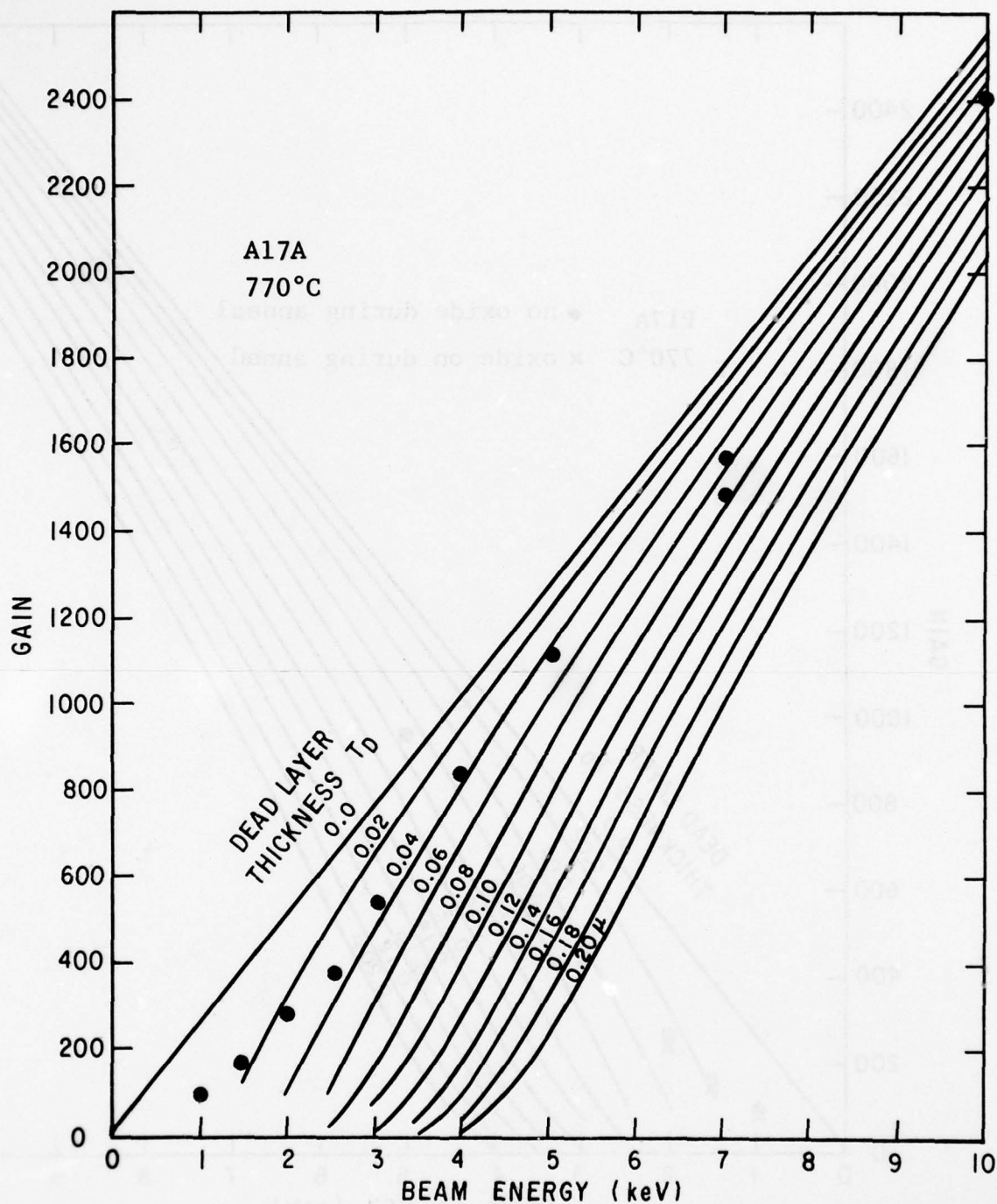


Figure 18. Gain versus Beam Energy Measurements for As^+ Implanted at 100 keV, 10^{14} cm^{-2} Fluence, 7° Off Axis at Room Temperature. A 1000\AA Thermal Oxide was Grown on the $12-18\Omega\text{-cm} \langle 111 \rangle$ FZ p-Si Substrate Prior to Implant. Annealing was for 1 hr. at 770°C in Ar After Implantation

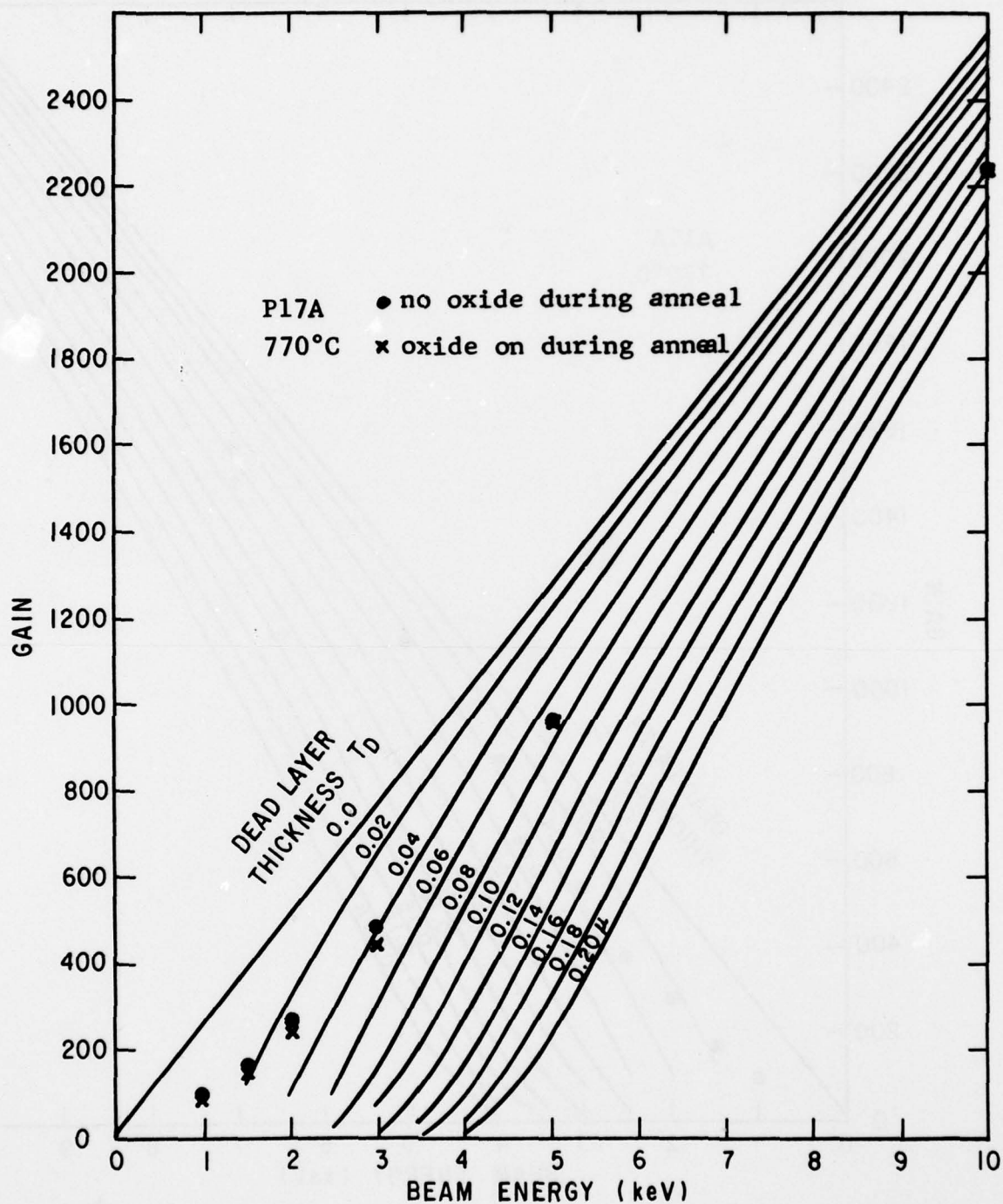


Figure 19. Gain vs. Beam Energy Measurements for P^+ Implanted at 100 keV, 10^{14} cm^{-2} Fluence, 7° Off-Axis at Room Temperature. A 1800\AA Thermal Oxide Was Grown on the $12-18\text{-}\mu\text{-cm} \langle 111 \rangle$ FZ p-Si Substrate Prior to Implant. Annealing Was for 1 hr. at 770°C in Ar After Implantation

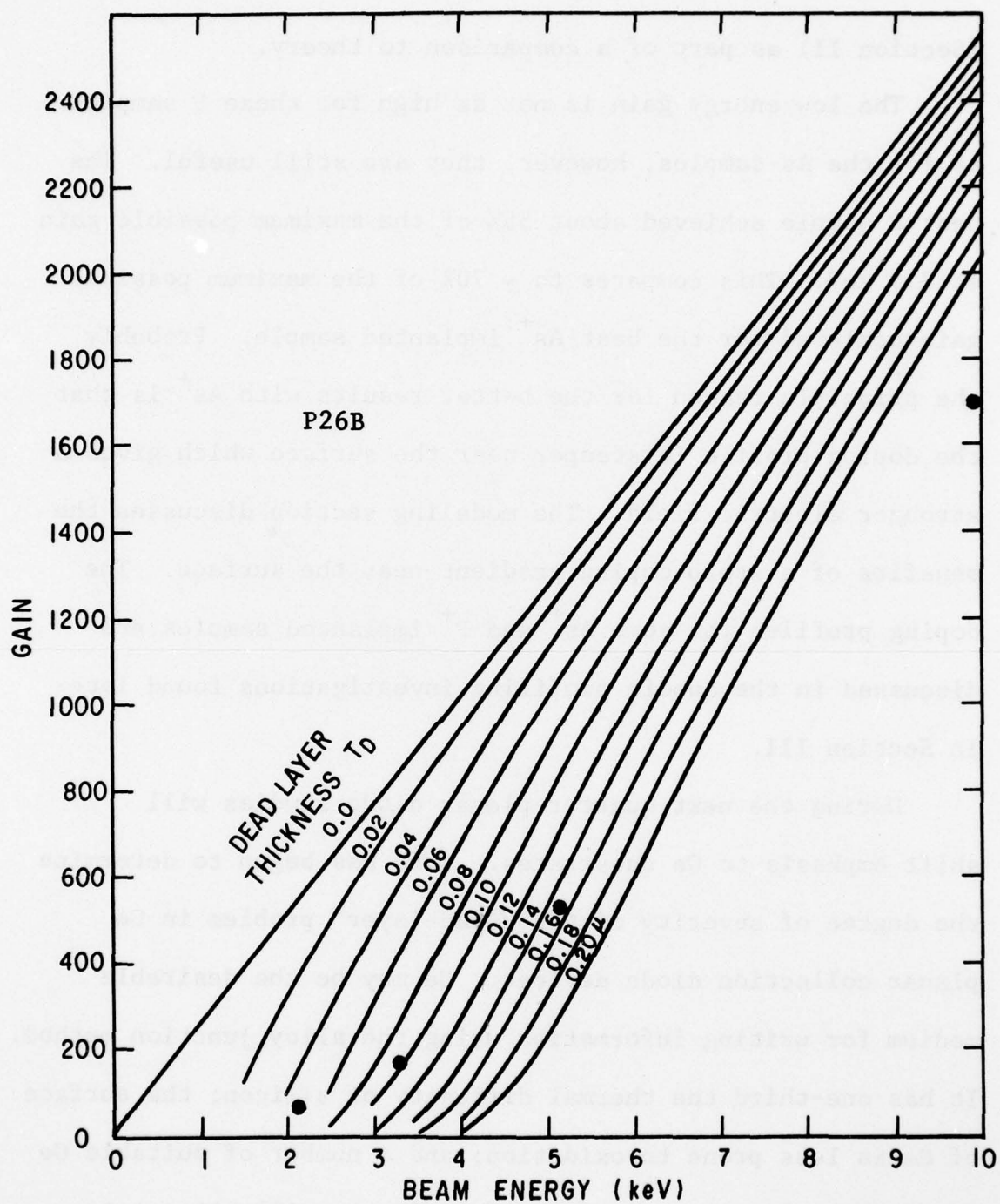


Figure 20. Gain vs. Beam Energy Measurements for P^+ Implanted at 100 keV, 10^{14} cm^{-2} Fluence, 7° Off-Axis at Room Temperature. A 3665\AA Thermal Oxide was Grown at 1100°C on the 12-18 $\mu\text{-cm}$. $\langle 111 \rangle$ FZ p-Si Substrate After Implantation

(Section II) as part of a comparison to theory.

The low energy gain is not as high for these P samples as for the As samples, however, they are still useful. The best P sample achieved about 55% of the maximum possible gain at 2.5 keV. This compares to ~ 70% of the maximum possible gain achieved for the best As⁺ implanted sample. Probably the principle reason for the better results with As⁺ is that the doping profile is steeper near the surface which gives a stronger electric field. The modeling section discusses the benefits of a steep doping gradient near the surface. The doping profiles for some As⁺ and P⁺ implanted samples are discussed in the anodic profiling investigations found later in Section III.

During the next quarter planar diode studies will shift emphasis to Ge substrates. Work has begun to determine the degree of severity of the "dead-layer" problem in Ge planar collection diode devices. Ge may be the desirable medium for writing information using the alloy junction method. It has one-third the thermal diffusivity of silicon; the surface of Ge is less prone to oxidation; and a number of suitable Ge metal eutectic systems exist. Experiments will attempt to achieve planar diodes with small gain deficits at ~ 4 keV. Because of the higher mass density of Ge, these targets can

be operated at somewhat higher beam energies without increasing the amount of electron scattering. The electron scattering and penetration will be the same at 4 keV for Ge as at 2.5 keV for Si.

Using ion implantation, planar collection diodes have been formed in p-type $< 100 >$ 1-3 ohm-cm Ga-doped Ge. P^+ and As^+ ions were implanted at energies of 50 keV and 100 keV to fluences of 10^{13} ions/cm². As^+ implanted at 50 keV and 100 keV, produced calculated projected ranges of 0.0214 μ and 0.038 μ and 0.0792 μ , respectively.⁽¹²⁾ An annealing schedule calling for 500° and 700°C, 1 hour anneals, in inert gas flow is being pursued currently, in order that these targets may be examined in the SEM to determine the resulting "dead-layer" thickness for Ge devices. A bank of furnaces dedicated solely to the Ge work has been established for this work.

Anodic Oxidation and Profile Measurement

As noted above, it is desired that the information storage side of the planar collection diode have a steep gradient in carrier concentration with the concentration decreasing by a factor of 50 to 100 in the 1000Å from the surface to the junction. These targets are produced by ion implantation and such parameters as ion species used, beam energy, and thermal oxide thickness on the surface must be chosen to yield

a suitable target gradient. In order to check the modeling of the collection efficiency, as well as the actual device structure, it is necessary to experimentally determine the carrier concentration achieved as a function of depth. The method chosen for doing this profiling is that of incremental sheet resistance measurement.^(13,14) Resistance is measured by a four-point probe as shown in Figure 21 where current flows through the outer probes and voltage is measured between the inner probes. A layer of silicon is removed and the process is repeated. Conductance as a function of depth is plotted and a smooth curve drawn to fit the data. The curve is digitized and is entered into a computer program which then calculates the profile. All of these procedures will be discussed in more detail below.

The four-probe resistance measurements are taken by first running a current through the voltage probes to "form" the contacts.⁽¹⁵⁾ A number of fixed currents are then passed through the current probes and the voltages are recorded for each. The current is reversed to help correct for any biasing effects. The probes are then reset to a new location on the wafer and the process repeated. Currents are supplied by a Digitek 3110 precision current source with resolution to micro-amperes. Voltages are measured on a Keithley 160B multimeter.

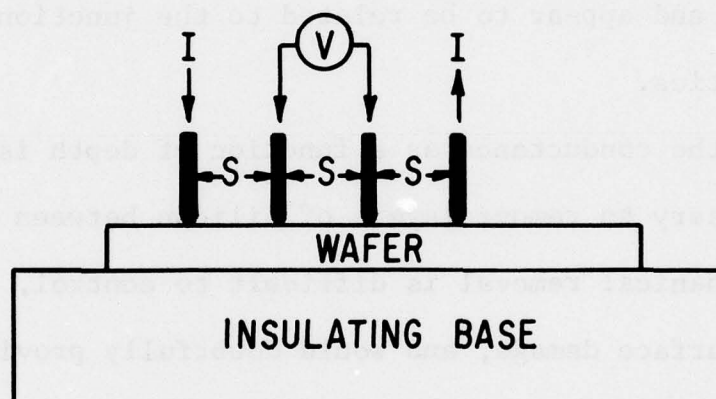


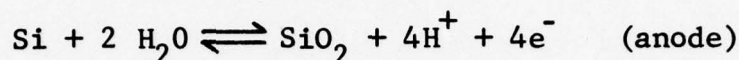
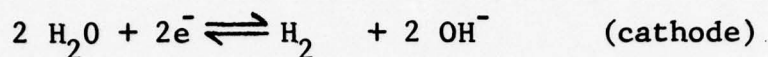
Figure 21. Four-Probe Resistivity Measurement. Current is Passed Through Outer Probes, Voltage Measured Through Inner Probes. Probe Spacing "S" is 0.0625 in.

The four-point probe station is by Signatron Corp. and has a probe spacing of 0.0625 in. and pressure of 45G.

In regions of high conductance (the first region of the profile) it has been found that the results are quite reproducible. Dependence of the resistance on current is very small. Systematic biasing effects are small, and resetting the probes yields results which agree to within a few percent. Measurements deep into the sample are not so reliable and appear to be related to the junction characteristics.

Since the conductance as a function of depth is needed, it is necessary to remove layers of silicon between measurements. Mechanical removal is difficult to control, may result in surface damage, and would doubtfully provide the resolution desired. A chemical means is more appropriate. Simple chemical etching is difficult to control precisely, so the method chosen is to oxidize the silicon surface, measure the oxide thickness, and then etch away the oxide without significantly affecting the underlying silicon. The last step is carried out using buffered HF.⁽¹⁶⁾ The technique of anodic oxidation is used, since the high temperatures used in the growth of a thermal oxide will likely affect the profile sought.

In anodic oxidation, the silicon wafer forms the anode in an electrolytic cell. Reactions⁽¹⁷⁾ at the cathode and anode which are independent of electrolyte used, are:



One might, therefore, expect that for a given number of coulombs passing through the cell, a well-defined thickness of oxide would be formed. The current efficiency, however, is only about 0.8% and depends on the conditions of the anodization.⁽¹⁶⁻²⁰⁾ Schmidt and Owen⁽²¹⁾ point out that the resistance of the oxide deposited at higher current densities is larger, due either to a thicker oxide layer (higher current efficiency) or a higher resistivity of the oxide.

A typical voltage-time curve is shown in Figure 22 which is taken from Ref. 16. Similar behavior was noted in our work although anodizations were usually terminated at roughly 100 volts, well below the maximum voltage obtainable. Typical values for V_0 that we have found were 12-18 volts, in agreement with those reported in the literature. According to Davies et al.,⁽¹⁶⁾ 3 volts is independent of current density and is the emf associated with the electrode reactions. The rest is proportional to current density and is the IR drop

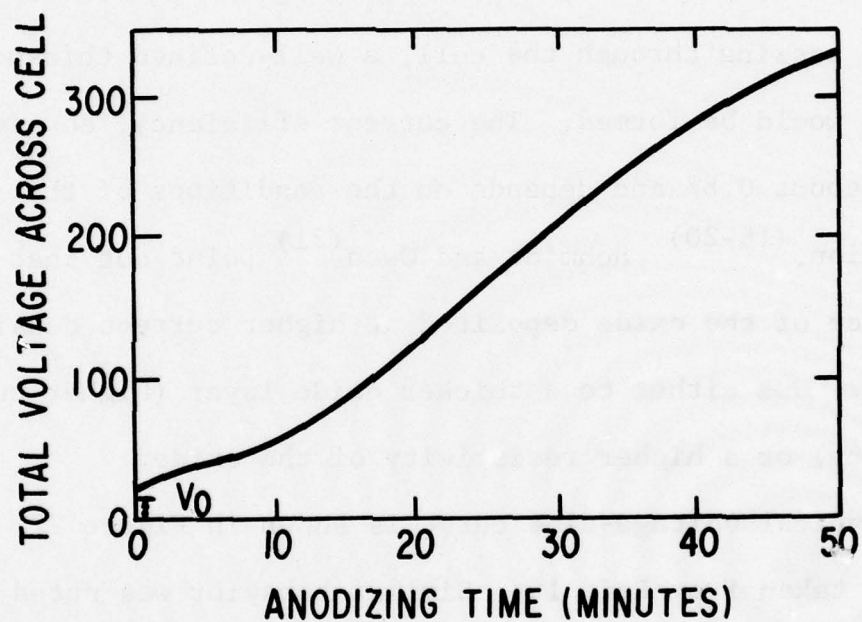


Figure 22. Typical Anodization Curve; Taken From Ref. 16.
Note the Initial Voltage V_0 . Present Anodizations are
Typically Taken to Roughly 100V

across the electrodes and electrolyte. V_o should be subtracted from V to give the voltage across the oxide layer.

The choice of an electrolyte is nontrivial. A variety of electrolytes are cited in the literature. One wishes to avoid or minimize detectable dissolution of either Si or SiO_2 . It is also important to avoid "creeping" of the electrolyte up the electrodes,⁽¹⁸⁾ a problem with N-methylacetamide, a popular electrolyte. Furthermore, water absorbed in the electrolyte will sometimes result in oxide layers of poor quality.⁽¹⁷⁾ We have obtained satisfactory results by using concentrated nitric acid (70%). At elevated temperatures, it is noted that the choice of an electrolyte depends somewhat on the samples involved since materials of higher conductivity and/or suffering radiation damage⁽²²⁾ may anodize differentially.

The anodization cell used in this work is illustrated in Figure 23. The wafer is mounted in a custom holder based on a design by R. A. Sigsbee.⁽²³⁾ This design enables the anodization of one side of the wafer only with an electrical contact to the rear of the wafer which is well insulated from the electrolyte. Schmidt and Michel⁽¹⁸⁾ and our preliminary experiments have shown that stop-off lacquers are unsatisfactory

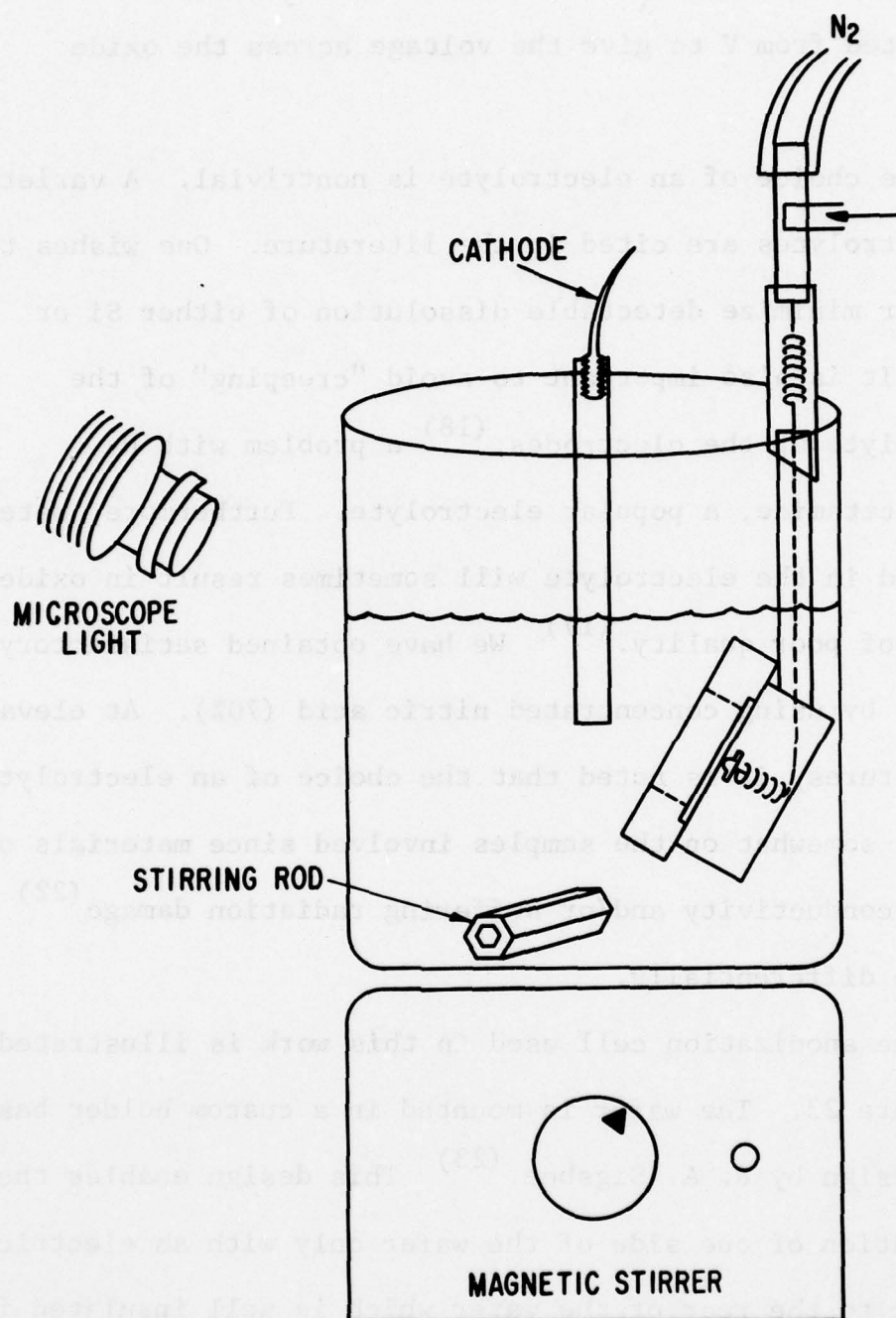


Figure 23. Schematic of Anodization Cell. Electrical Contact to Wafer is from Behind, within Teflon Holder. A Pressure of Nitrogen keeps Electrolyte from Entering Holder

for this purpose. Illumination of the wafer during the anodization process has been found to affect the current-voltage characteristics. It has been pointed out⁽¹⁸⁾ that for n-type silicon, the rate of growth is limited by the concentration of holes, largely generated by illumination.

The current is supplied by an HP-6209B regulated current and voltage source. Schmidt and Owen found that the quality of the oxide was dependent on the current density.⁽²¹⁾ Current densities of 7, 5, 2.8, and 2.3 mA/cm² have been used with little difference in oxide quality noticed. The anodizations went much more quickly in the case of the larger current densities, as expected. Typical times for anodizations were around 20 minutes.

The thickness of the oxide layer is measured by means of ellipsometry.⁽²⁴⁾ The ellipsometer reflects polarized light from the oxide surface and Si-SiO₂ interface through an analyzer to a photo cell. Minima of the reflected signal are obtained by rotation of the polarizer and analyzer. Computer analysis of the angular settings yields an oxide thickness and index of refraction of the oxide. Two measurements from different spots on each film are taken. These measurements typically agree to within 5 Å.

We noticed a systematic increase of index of refraction with decreasing oxide thickness. Examination of different

phases of SiO_2 along with their densities and indices of refraction indicates that the density of the oxide layer is increasing with decreasing film thickness. This is important since the thickness of the oxide must be related to the thickness of the silicon removed to obtain the profile. (25) Busen and Linzey (19) have studied directly the ratio of silicon consumed to SiO_2 thickness and have found results consistent with those above. Although there is substantial scatter in the data of Busen and Linzey, calculations based on their results yield Figure 24 which relates the thickness of oxide to the silicon consumed. The straight line in Figure 24 is based on a constant ratio of (thickness Si/thickness SiO_2) = 0.45 which assumes an oxide density of 2.27 g/cm^3 independent of thickness. The difference between the two curves is important for relatively thin oxide layers.

The sheet conductance, $G(x)$, is given by

$$G(x) = [\ln 2 / \pi] \cdot I/V = 0.2206 \cdot I/V \quad (29)$$

where I and V are the 4-point probe readings. This assumes:

- (1) Equal probe spacing.
- (2) Dealing with a semi-infinite volume.
- (3) No change in type and planar uniformity in doping in the depth probed. These assumptions should all

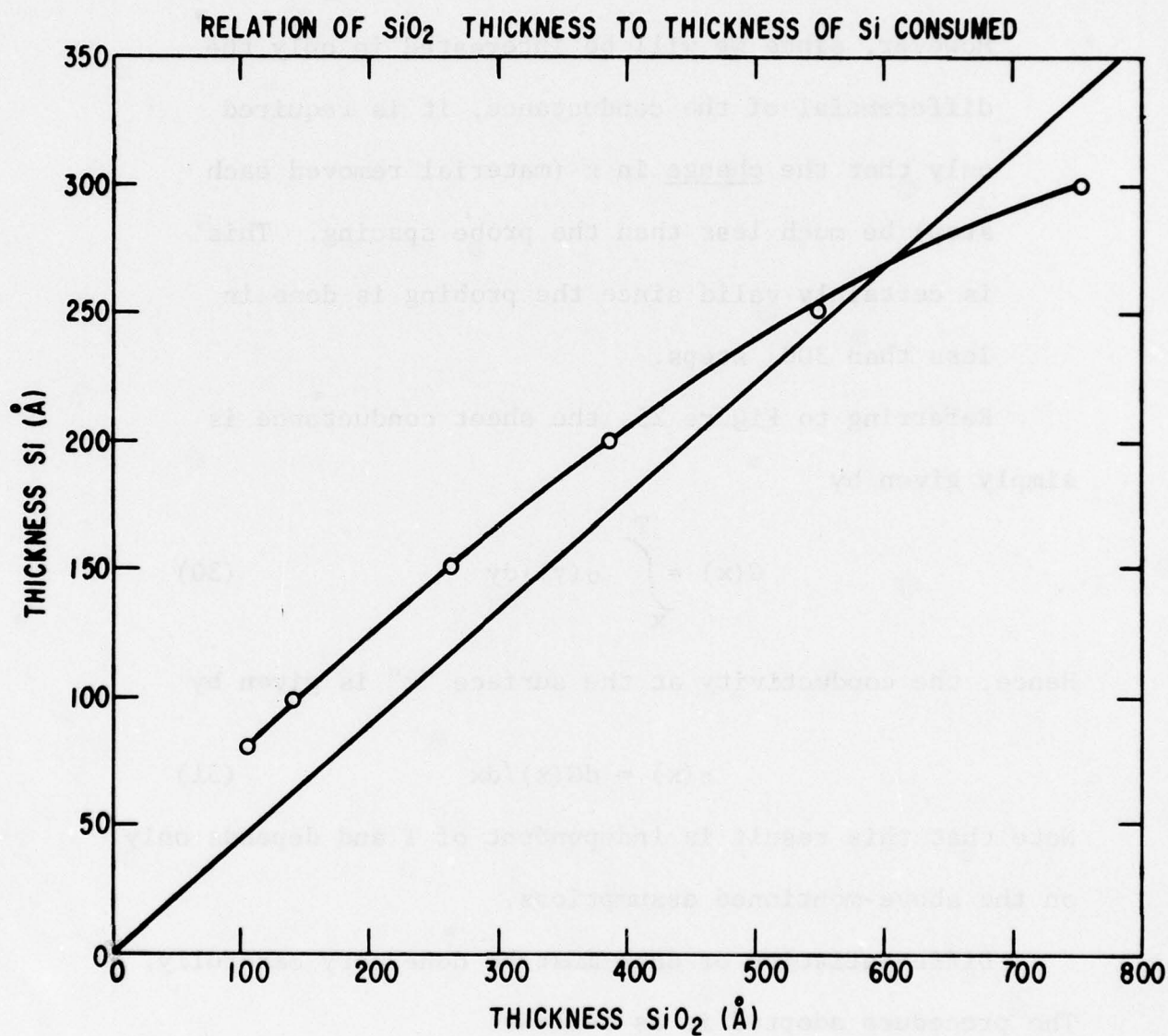


Figure 24. Thickness of Si as Function of Thickness of SiO_2 . Data Points are Adapted from Ref. 25. The Straight Line is Based on an Oxide Density of 2.27 g/cm^3 , Independent of Layer Thickness

be valid⁽²⁶⁾, except for the third which is not when the surface is near the junction. Strictly speaking, $G(x)$ is only the sheet conductance if T is much less than the probe spacing (see below and Figure 25.) However, since we will be interested in only the differential of the conductance, it is required only that the change in x (material removed each step) be much less than the probe spacing. This is certainly valid since the probing is done in less than 300Å steps.

Referring to Figure 25, the sheet conductance is simply given by

$$G(x) = \int_x^T \sigma(y) \cdot dy \quad (30)$$

Hence, the conductivity at the surface " x " is given by

$$\sigma(x) = dG(x)/dx \quad (31)$$

Note that this result is independent of T and depends only on the above-mentioned assumptions.

Differentiation of data must be done very carefully.

The procedure adopted is as follows:

- (1) $G(x)$ is plotted on semi-log paper as a function of x .
- (2) A smooth curve is drawn through the points. This performs a first averaging of the data.

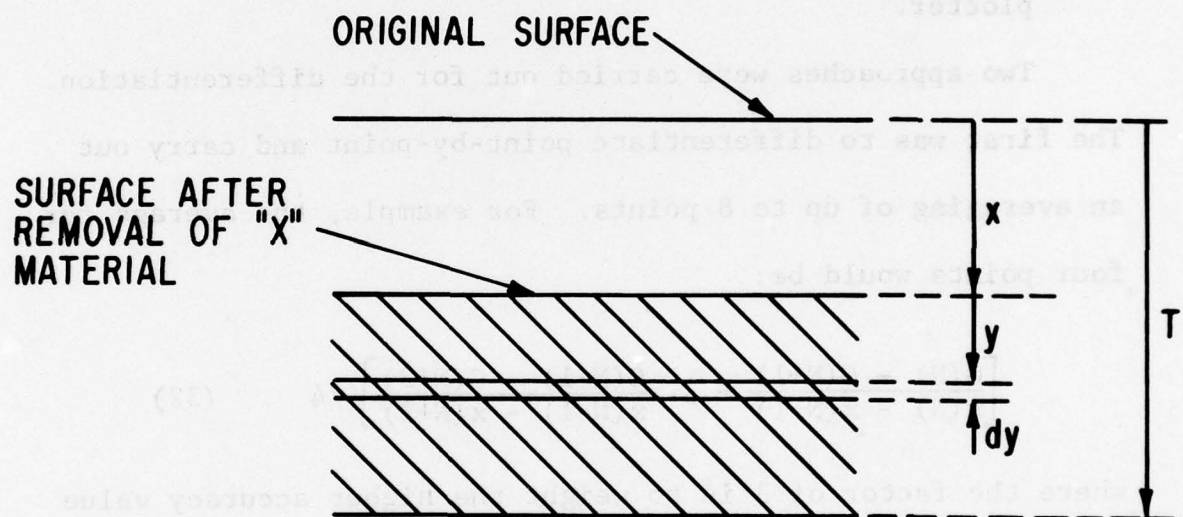


Figure 25. Schematic for Showing Derivation of the Conductivity, σ , As a Function of x . See Text

- (3) This smooth curve is then digitized using a Numonics Corporation digitizer inputting the data to a HP 9830A.
- (4) A computer program then performs three functions. First, it differentiates the inputted data; second, it converts the calculated conductivity to carrier concentration, $N(x)$; and third, it plots $N(x)$ as a function of x using a HP 9862A plotter.

Two approaches were carried out for the differentiation. The first was to differentiate point-by-point and carry out an averaging of up to 8 points. For example, the average for four points would be:

$$\left[\frac{G(N) - G(N+1)}{x(N) - x(N+1)} + 3 \cdot \frac{G(N-1) - G(N+2)}{x(N-1) - x(N+2)} \right] / 4 \quad (32)$$

where the factor of 3 is to weight the higher accuracy value and the factor of 4 is for normalizing the average. The second approach was to use the procedure of Evans and Donovan⁽²⁷⁾ where the identity

$$\sigma(x) = dG(x)/dx = 2.3 \cdot G(x) \cdot d[\log_{10} G(x)]/dx \quad (33)$$

is used. The derivative of the log is slowly varying, in practice, and is calculated by determining the slope of a least-squares fit line through 5 points centered on x .

The conversion of σ to N was carried out using the expression of Caughey and Thomas⁽²⁸⁾,

$$\mu = \mu_{\min} + \frac{(\mu_{\max} - \mu_{\min})}{[1 + (N/N_{\text{ref}})^{\alpha}]} \quad (34)$$

Their summary of the literature for p-type Si gives

$$\mu_{\min} = 47.7 \text{ cm}^2 \text{ V}^{-1} \text{ sec}^{-1}$$

$$\mu_{\max} = 495 \text{ cm}^2 \text{ V}^{-1} \text{ sec}^{-1}$$

$$N_{\text{ref}} = 6.3 \times 10^{16} \text{ cm}^{-3}$$

$$\alpha = 0.76$$

For n-type Si, the results of Baccarani and Ostoj⁽²⁹⁾ are used, namely

$$\mu_{\min} = 92 \text{ cm}^2 \text{ V}^{-1} \text{ sec}^{-1}$$

$$\mu_{\max} = 1360 \text{ cm}^2 \text{ V}^{-1} \text{ sec}^{-1}$$

$$N_{\text{ref}} = 1.3 \times 10^{17} \text{ cm}^{-3}$$

$$\alpha = 0.91$$

It is noted that these last values are for phosphorus doping. Different values would be expected for different dopants but within the experimental errors and desired accuracy, should not be critical. In the computer program, the conversion of σ to N is done by successive approximations. Seven inter-

actions are sufficient to obtain greater than 99% accuracy.

Figures 26 and 27 indicate the input and output of a test run. Figure 26 shows a semilog plot of a linearly decreasing conductance (note insert) which corresponds to a constant concentration of 10^{18} cm^{-3} (n-type Si). Figure 27 shows the output of the computer program. Here the circles are using the Evans and Donovan procedure while the x's use the point-by-point differentiation, averaging four points. Different digitizing inputs were used in each case so that the two sets of calculations cannot be directly compared. It is seen, however, that the procedure is valid to about $\pm 15\%$ with most of this error apparently related to the care with which the initial curve was plotted (by hand, not by computer). A larger-scale, more carefully drawn initial plot, and greater care in digitizing would reduce the scatter. These results, however, represent typical data handling procedures.

Profile measurements were made on five samples. Three of these were too small to use the regular anodization holder, and so a holder providing a smaller anodized area was used. The area exposed to all anodizations was smaller still, due to the impossibility of aligning the wafer identically each time. As a result, the data from these three wafers had

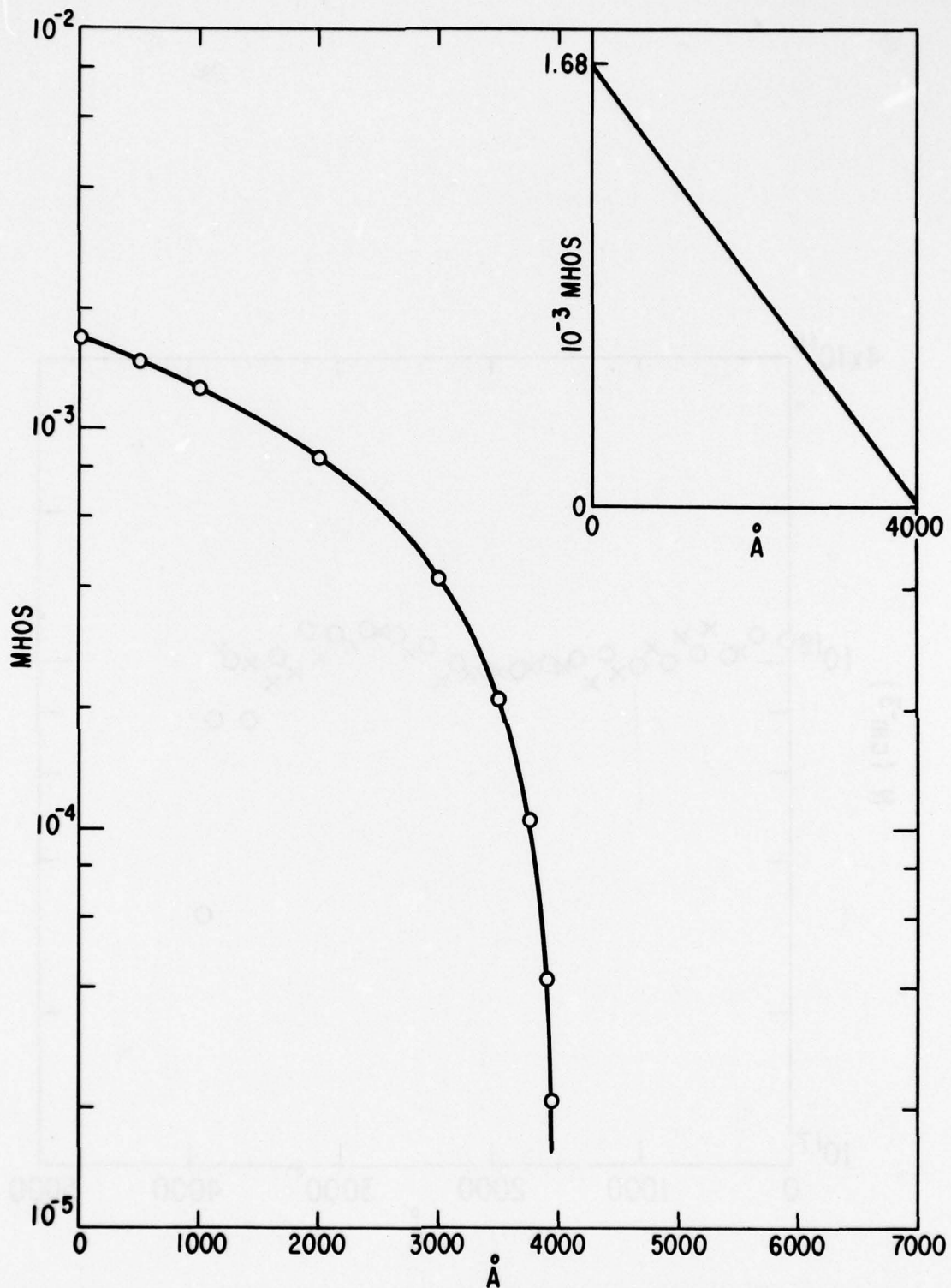


Figure 26. Semilog Plot of a Linearly Decreasing Conductance (see insert) As a Function of x . This Corresponds to a Constant Concentration of 10^{18} cm^{-3} (n-type Si) for 4000 Å and then Dropping to Zero

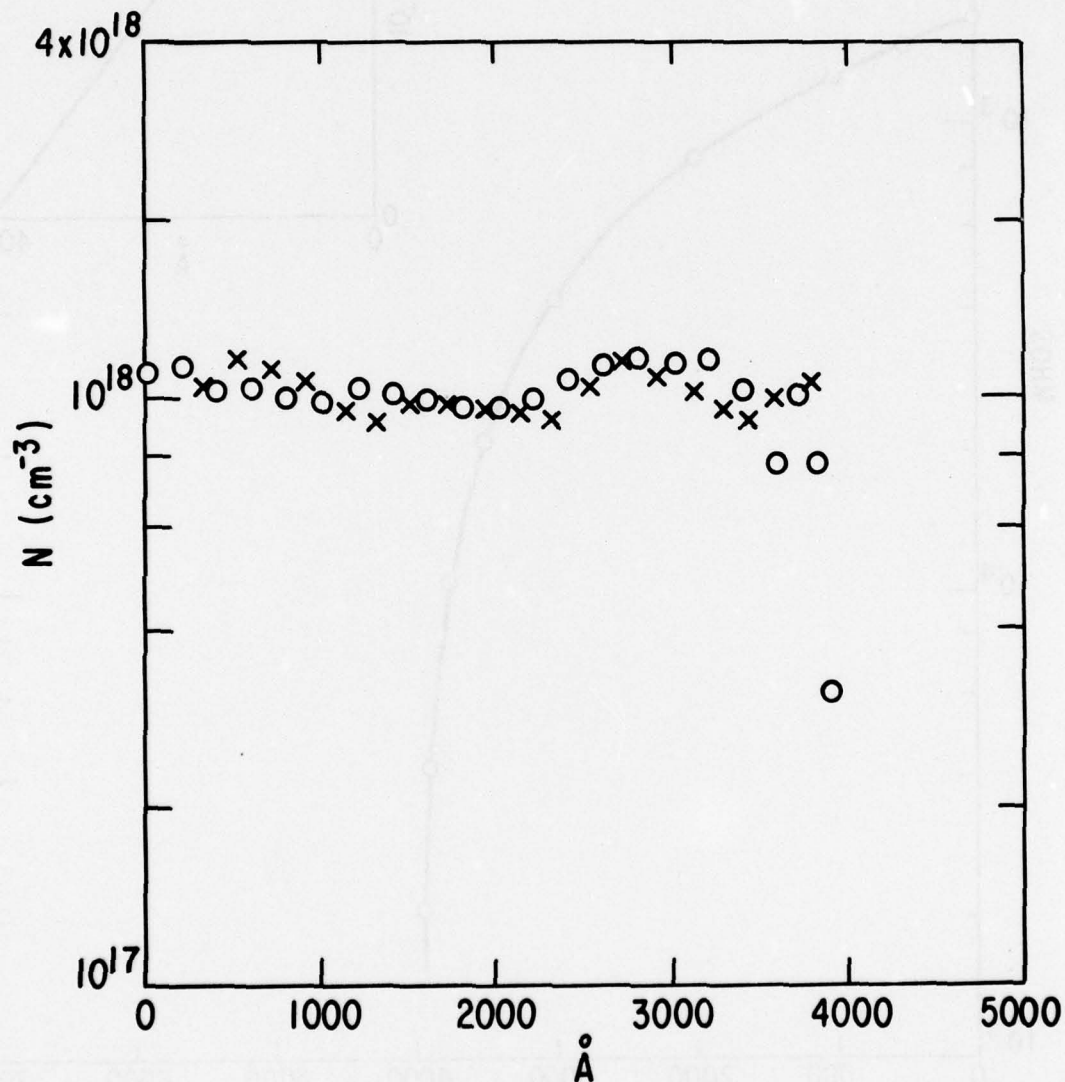


Figure 27. Computer Output of Calculated Carrier Concentrations Using Figure 26 As the Input

substantially more scatter than those from the other two larger wafers and quantitative profiles were not obtained. It was found, however, that the thermal oxide thickness prior to implantation plus the junction thickness, as determined from the data, added to roughly 1200Å for the three samples. This is the expected penetration for the implantation. Furthermore, the conductivity of two of the wafers, measured beyond the junction depth, approached the intrinsic value expected for the original material.

The two larger wafers, P18A (ion: P, energy:100 keV, dose: $10^{14}/\text{cm}^2$) and A22A (ion: As, energy:100 keV, dose: $10^{14}/\text{cm}^2$) gave more precise results. There was no thermal oxide grown on either. The conductivities and computed profiles are shown in Figures 28 through 31. Note that the phosphorus profile is nearly flat for the first several thousand angstroms, while the arsenic profile peaks near 500Å and drops off rapidly thereafter. These results would indicate that a wafer implanted with arsenic ions through an appropriate thermal oxide at an appropriate dose might well provide a workable archival memory target.

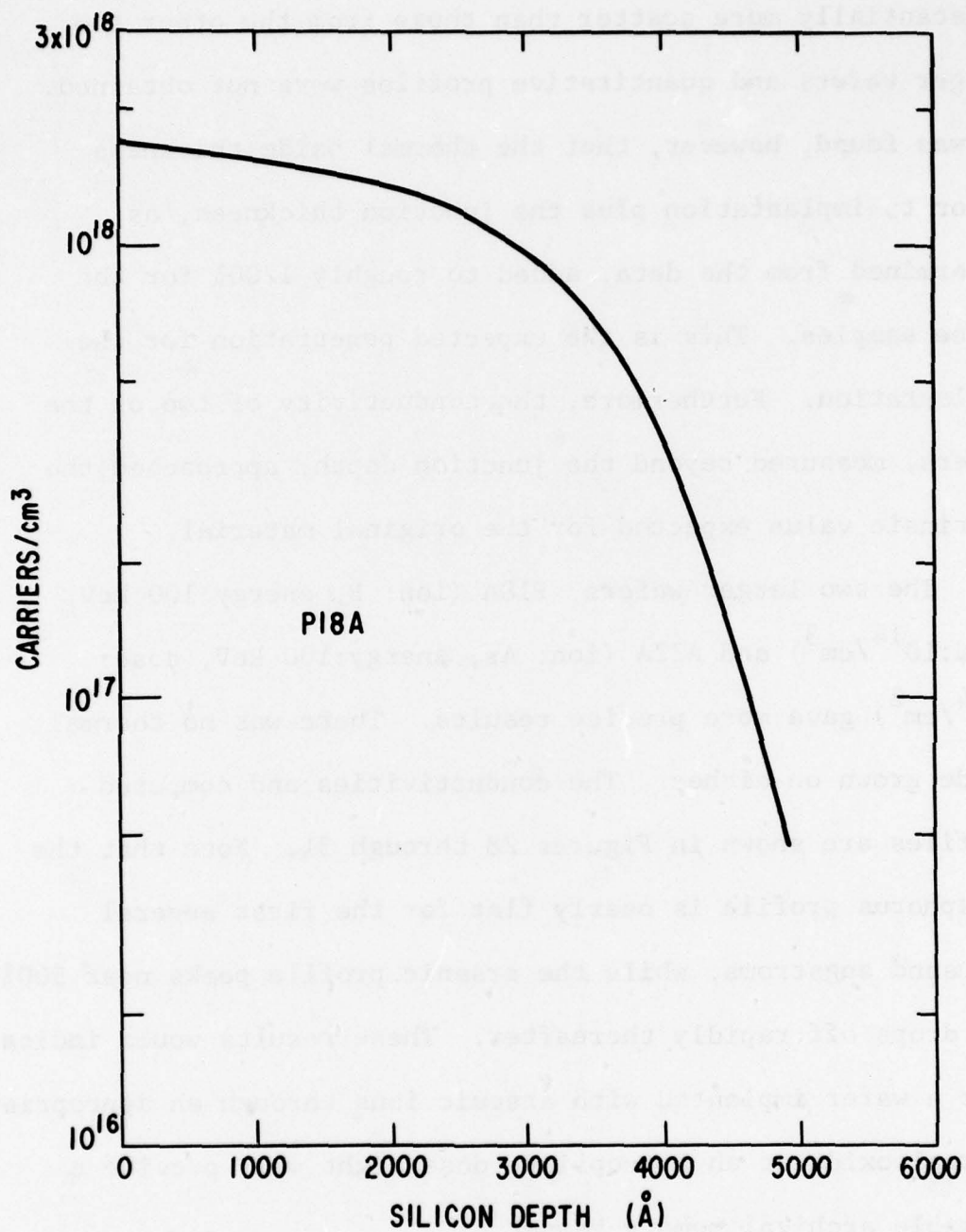


Figure 28. Conductance of Sample P18A as Function of Depth. Sample was Implanted with Phosphorus Ions. Conductance = $0.2206/(V/I)$

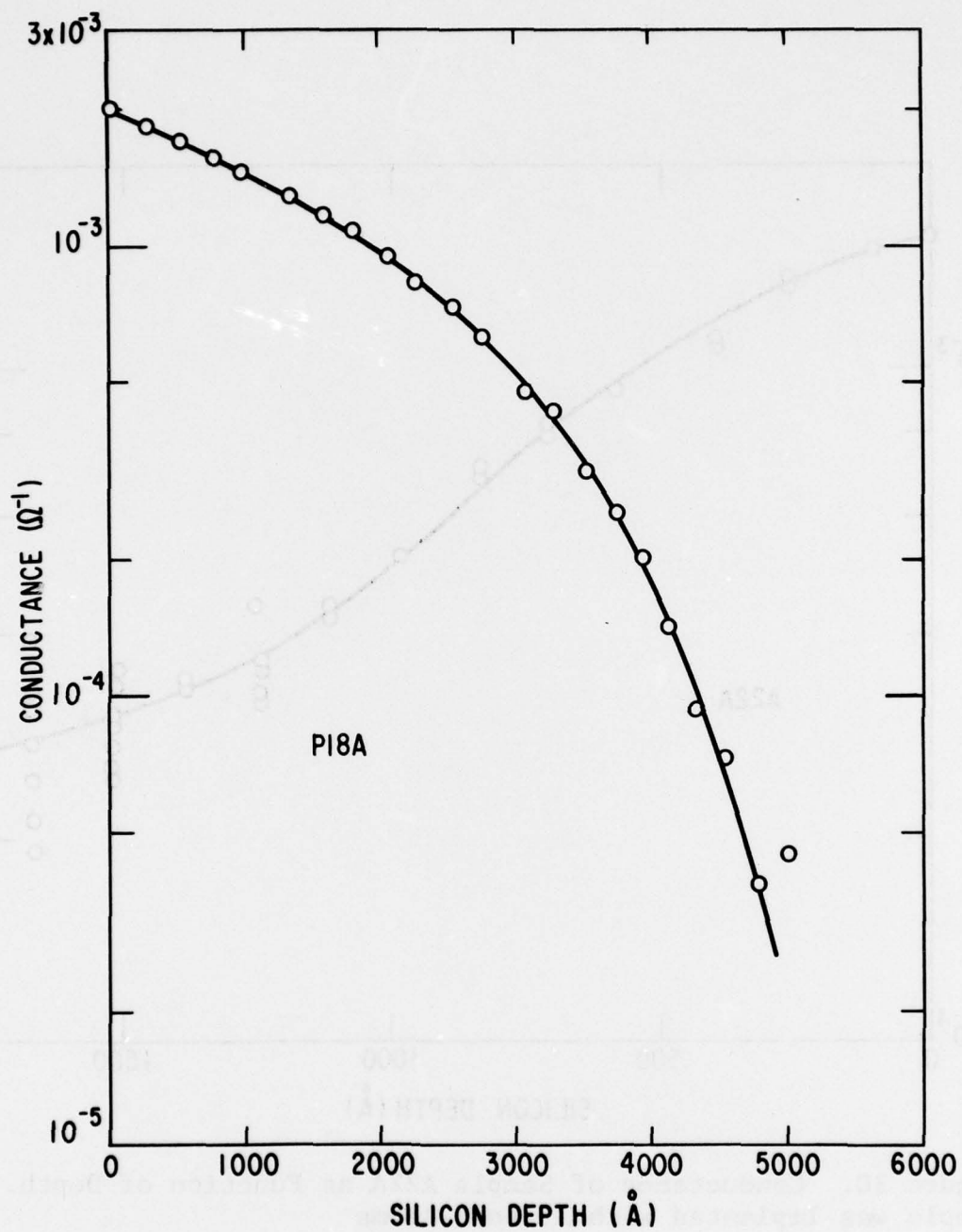


Figure 29. Profile of Sample P18A. Based on Smooth Conductivity Curve Drawn in Figure 25

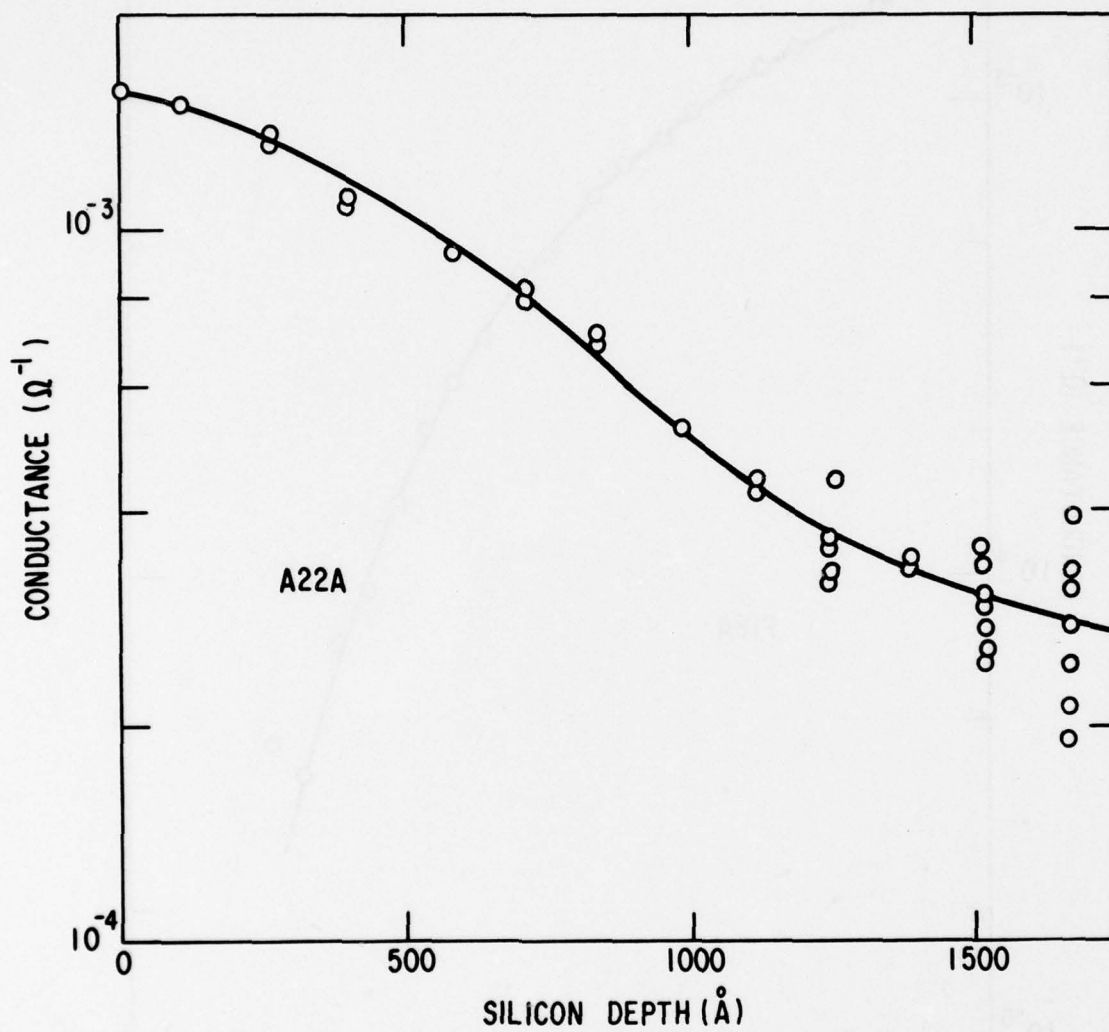


Figure 30. Conductance of Sample A22A as Function of Depth. Sample was Implanted with Arsenic Atoms

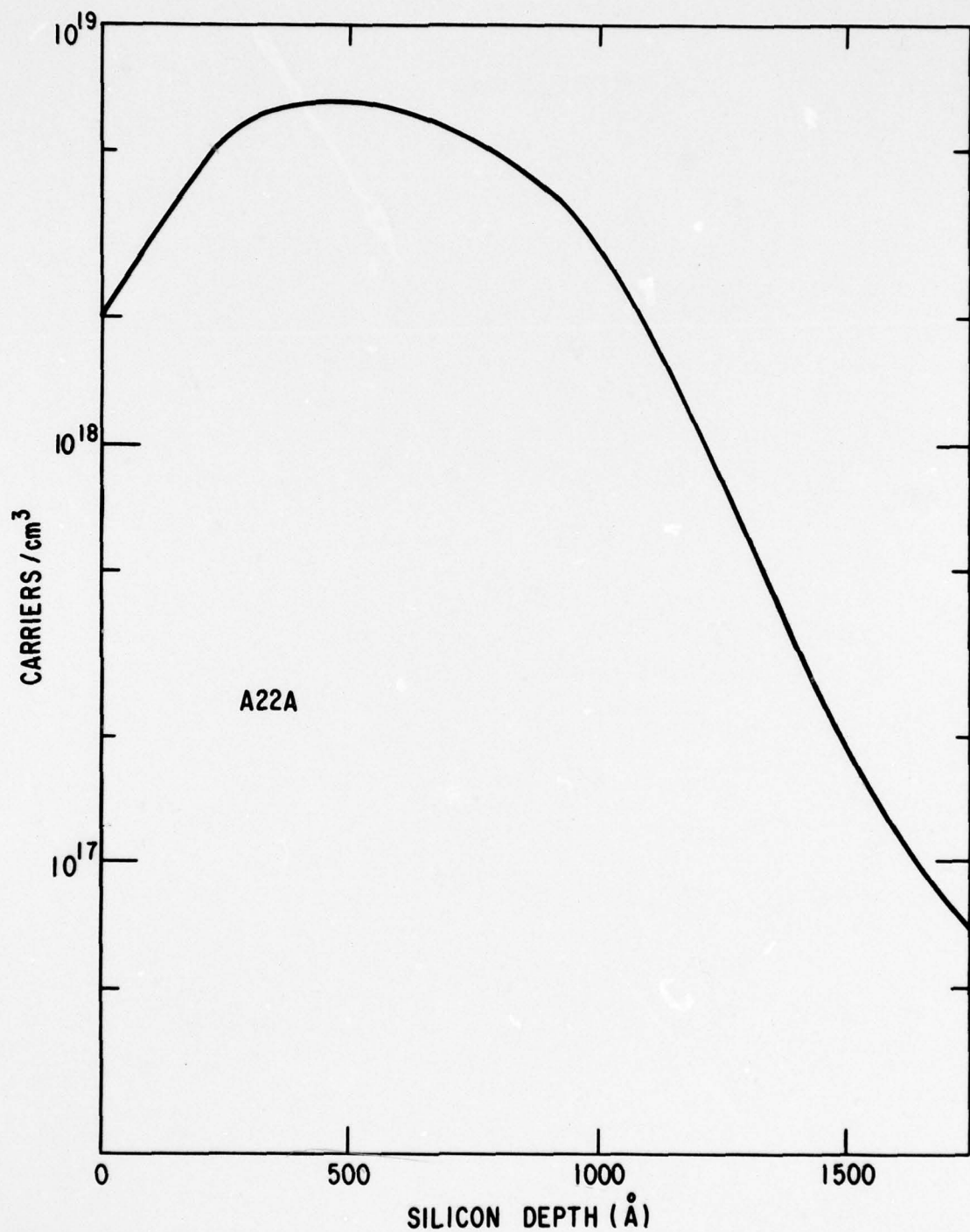


Figure 31. Profile of Sample A22A. Based on Smooth Conductivity Curve Drawn in Figure 27

SECTION IV

INFORMATION WRITING STUDIES

Inert Ion Writing Experiments

At the end of the first quarter, with the planar diode studies proceeding successfully, a set of ion writing experiments was conducted. These studies employed He ions to write a pattern using an ion damage mechanism, rather than the ion doping mechanism, initially proposed as the storage technique. The resulting device showed excellent reading characteristics akin to those produced by writing diode bits with a boron ion beam.

Damage writing, therefore, appears to have potential as the candidate writing method. The problem of depletion field spreading may be considerably less severe, since an actual diode is not formed during the writing process in Si (inert ions impinging on Ge can cause p-type conversion). Since less fluence may be required to sufficiently damage the semiconductor than dope it, higher writing rates may also be possible. The higher writing rates may be supported even more by the possible existence of a gain mechanism in the damage writing process. Experimental writing to date would indicate two orders of magnitude less fluence required for

damage writing than by doping writing. In addition, a wider variety of elements are potentially suitable for this method, giving greater latitude for selection of an ion appropriate to the electron optics. Yet, the damage writing may still retain the desired "archival" feature, with written data withstanding relatively high temperatures and rugged treatment.

In the initial ion doping writing using boron ions, the output signal is modulated by variation in the number of electron-beam induced carriers collected at the planar diode due to the presence of the boron implanted diodes in the surface of the substrate. Electron-hole pairs generated by the reading beam are trapped by the diode's depletion field until they recombine.

Damage-writing could result in local carrier recombination due to the resulting very short minority carrier lifetime. Incoming implanted ions significantly disrupt the crystalline order of the semiconductor, producing many defects which act as trapping sites, along the ion path.

For a crystalline target, the substrate atoms are bound to their lattice sites by a displacement energy. As the implanted ion travels through the crystal, it makes many violent collisions with atoms in the substrate. A displaced atom may act as a secondary projectile, if struck by an ion

with energy greater than its displacement energy. Such secondary projectiles come to rest through elastic and inelastic collisions, producing another generation of projectiles if they are sufficiently energetic, and so on. Thus the damage production is a cascade process, with the incident ion the primary disorder-causing projectile. The extent and character of the disorder zone or cluster illustrated in Figure 32 are governed by the mass of the implanted ion and its energy, the mass of the substrate atom, the substrate temperature and the ion fluence. For sufficiently high doses of implanted ions, these cascade clusters can overlap, forming an amorphous zone.

Light ions lose a large part of their energy through inelastic, electronic processes. They penetrate deep into a silicon substrate, surpassing the collision cascade's depth. Most of the displaced atoms form isolated defects along the ion track. Therefore light ion implantation results in the formation of large numbers of interstitials and vacancies. For a heavier ion such as phosphorus, a larger fraction of elastic collisions results in more lattice damage. There is a greater tendency for the disorder to occur within a damage core, surrounded by point defects.

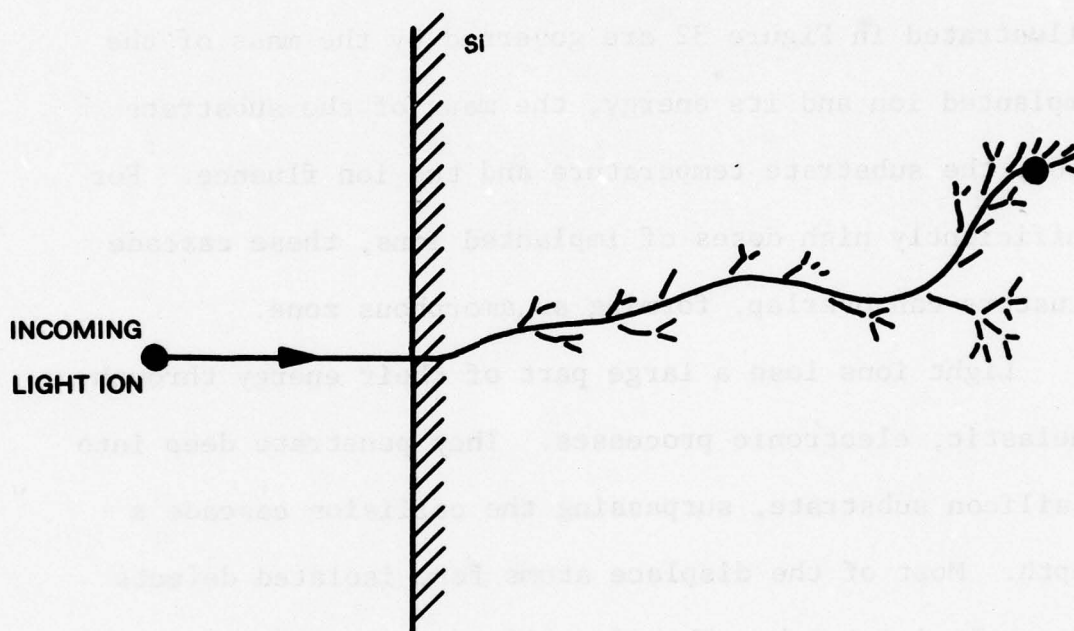


Figure 32. Damage Cluster Formed Along Path of Incoming Ion (after Gibbons*)

* J. F. Gibbons "Ion Implantation in Semiconductors-Part II: Damage Production and Annealing," Proc. IEEE, Vol. 60, September 1972, pp. 1062-1096

At present, several potentially important ion sources are being constructed and tested at the Oregon Graduate Center. Target tests are underway to determine writing efficiencies of various ions such as He, Xe, Ar, and Ga studied there, as well as others of interest.

Due to the successful He writing experiment, more inert ion writing experiments were undertaken this quarter to study the possible gain mechanism and target readout characteristics. Planar diode structures used for these studies were processed using As^+ ions implanted at 100 kV to a fluence of $10^{14}/\text{cm}^2$, 7° off axis at room temperature. Collection characteristics of targets made with this particular process had been evaluated extensively in the SEM. These devices were then annealed at 770°C in Ar for 1 hour and then coated with a thick coat of resist and patterned with the Air Force Resolution mask. The targets were then implanted with various inert ions through the resist mask with a range of fluences.

He studies included implants at 30 kV for fluences of 10^{13} , 10^{12} , 10^{11} and 5×10^{10} ions/ cm^2 . Preliminary SEM results indicate a writing fluence of 10^{11} ions/ cm^2 may be feasible.

Other experiments involving writing with inert ions such as Ne, Kr, Xe and Ar have been initiated. The ion energies for these elements were selected to produce a projected range of $\sim 0.1\mu$ in each case. Fluences of 10^{13} , 10^{12} , 10^{11} , and 5×10^{10} ions/cm² were again specified. The results of this work will be contained in the next quarterly report.

In addition, light ions such as N⁺ and B⁺, as well as Ga⁺ will probably be examined for writing feasibility in the near future, since they possess attractive features from an ion optical point of view:

- Reduced Aperture Sputtering
- Potentially Better Quality Sources
(includes Ga source)
- Higher Velocity Ions

The possibility of achieving a high current Ga⁺, or impurity doped Ga source make the use of this ion relevant.

Although at present, damage writing is viewed very favorably as the means of writing information with an ion beam, there is a possible drawback. In general, annealing samples written with a doping ion will improve the modulated signal, because more electrically active sites form. However, the same may not hold for damage-written targets. Annealing radiation damage tends to reduce the degree of disorder in a crystalline structure. Therefore, studies of the anneal

characteristics of the damage will be of considerable interest. Many of the ion-induced defects do not anneal out until relatively high temperatures are reached. Thus, the "archival" quality of such information may be more than sufficient for satisfactory reliability, but further experiments will be required before a firm conclusion can be reached.

SECTION V

ALLOY JUNCTION STUDIES

Laser Formed Alloy Junctions

The laser formed alloy junctions are being produced and studied in order to learn as much as possible about the feasibility of the alloy junction approach before the electron beam writing equipment becomes available. In particular, it is desired to determine:

1. Can a very short duration pulse of heat, sufficient to raise the temperature only slightly above the eutectic temperature, create a stable, well mixed alloy region?
2. Is the resulting alloy diode easily read by an electron beam?

To answer the first question, 1000Å Al films were evaporated onto freshly etched Ge and Si wafers. Films of this thickness are fairly easy to produce with good accuracy and uniformity and yet are thin enough to allow the desired ultimate diode spacing. The laser was described in detail in the first quarterly report. The actual spot (information diode) size produced by the laser cannot be made much smaller than about 5µm. Since the laser is capable

of delivery much more power than needed, it is possible to proceed with these experiments before thermal bias equipment is ready. (This equipment will be described later in this Section.) The large spot size undoubtedly tends to lead to optimistic results regarding heat loss during alloying but this is at least partly compensated for by the lack of thermal bias in these experiments. The power delivered by the laser is very sensitive to surface reflectivity which changes when the Al melts and becomes mixed with the underlying semiconductor. This makes the actual total power difficult to estimate.

Metallurgical Studies

Two different patterns of spots were produced by the laser. Figures 33 through 36 are photomicrographs of the top surface showing the results of gradually increasing power. Here, a large spot size was desired since they were to be used for Auger analysis. Each spot is the result of 160 separate laser pulses using a 0.080 inch aperture and slightly defocused beam.

Spots from Figures 33, 35 and 36 were subjected to a detailed analysis using Auger spectra and sputter ion milling to obtain spatial profiles of their metallurgical compositions. Tracings of the profiles done (Al on Si) are shown in Figures

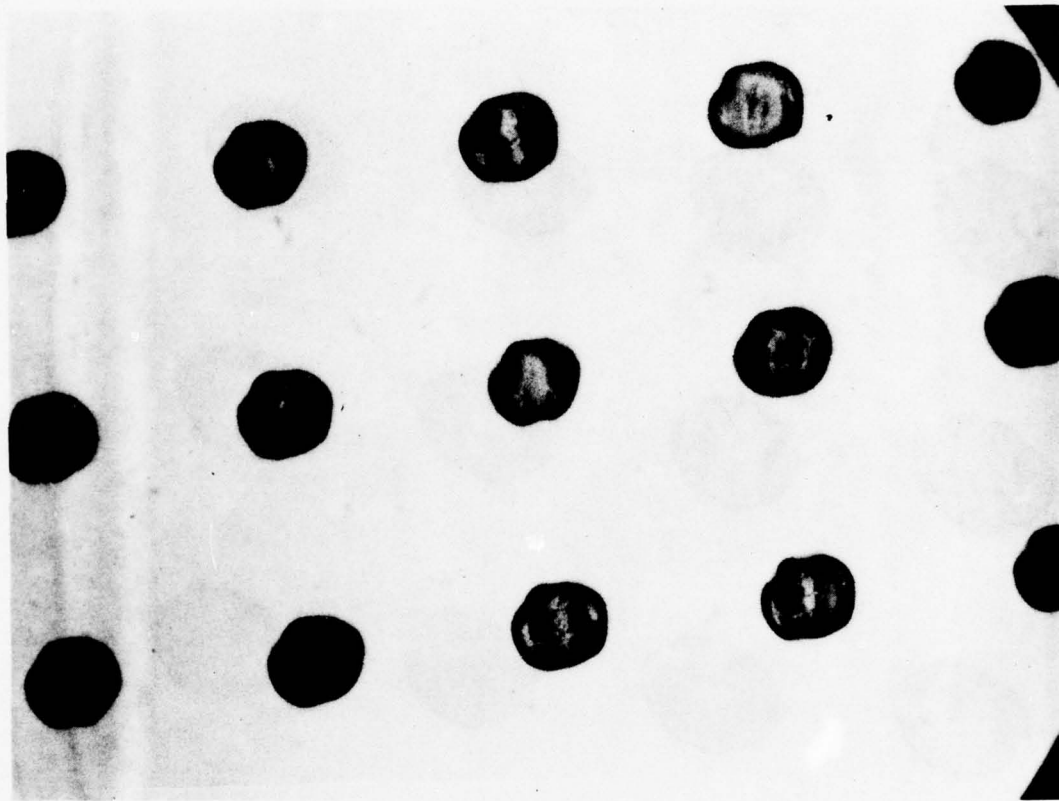


Figure 33. Photomicrograph of the Spots Formed by the Laser at the Lowest Power Used. The Extent of Surface Melting is about Half the Laser Spot Diameter. Spot Spacing is 100 μ m. These are the source of the Samples with Suffix D in Table 5



Figure 34. Photomicrograph of the Spots Formed by the Laser at the Second Lowest Power Setting. These Spots were not Profiled but the Sample was Used to Profile the "matrix" (the Al-Si Profile off a Spot). The Result is Shown in Figure 41, and on Table 4. Spot Spacing is 100 μ m



Figure 35. Photomicrograph of the Spots Formed by the Laser at the Third Power Setting. The Elliptical Shape of the Spots is Due to the Defocused State of the Laser. Two of these Spots are Profiled in Figures 39 and 40 and are Listed in Table 4 as Samples with Suffix B. Spot Spacing is 100 μ m



Figure 36. Photomicrograph of the Spots Formed by the Laser at the Highest Power Setting. The Laser Operation is Somewhat Unstable at this Setting as is Evident from the Surface Pattern. Two of these Spots are profiled in Figures 37 and 38 and are Listed in Table 4 as Samples with Suffix A. Spot Spacing is 100 μ m

37 through 43. Figure 41 is a profile of the matrix (taken off of a spot) as a control. Note that all spots showed evidence of Si even at the surface and that there appears to be fairly uniform mixing of Si throughout the Al film. Figure 44 shows the Auger spectrum of sample No. 14D before beginning ion milling. The Si line can be clearly seen. Also, in each case there is a well defined edge (boundary) to the Al film. In every case except the lowest power (Figure 43) there is excess Al (beyond its solid solubility) in the Si below the alloy region. This suggests that a temperature well in excess of the Si-Al eutectic (577°C) has been reached melting the region below the Al. Cooling then proceeded so rapidly that particles of Al precipitated in the Si. Table 5 summarizes the information given by the profiles. The compositions are uncertain to about $\pm 25\%$. The relative junction depths (given in minutes of ion milling time) also contain uncertainties. The origin of some of these errors is discussed below following a description of the Auger spectrometer.

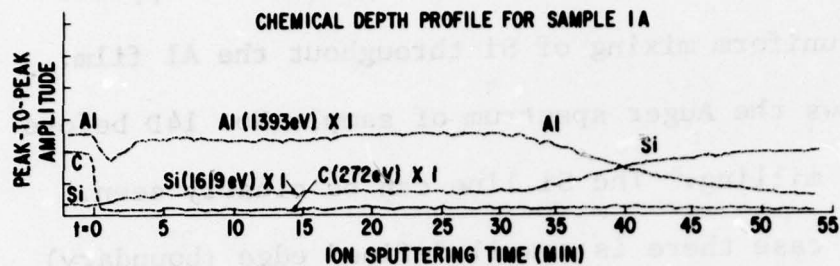


Figure 37. Auger Profile Obtained from Spots Shown in Figure 36

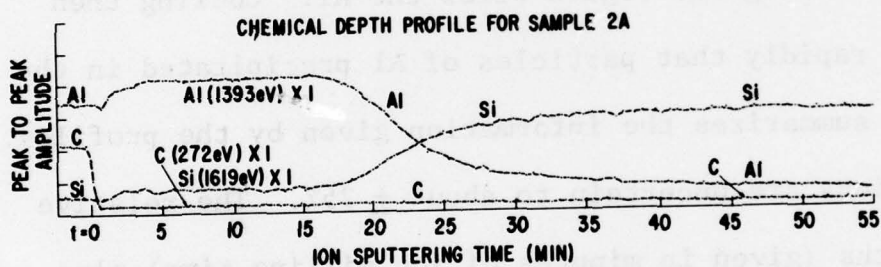


Figure 38. Auger Profile Obtained from Spots Shown in Figure 36

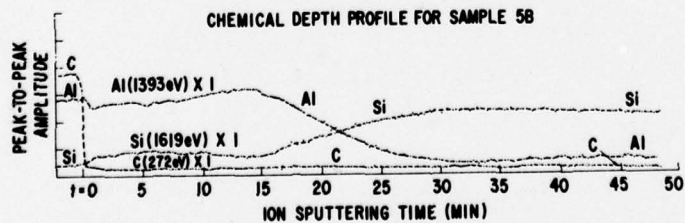


Figure 39. Auger Profile Obtained from Spots Shown in Figure 35

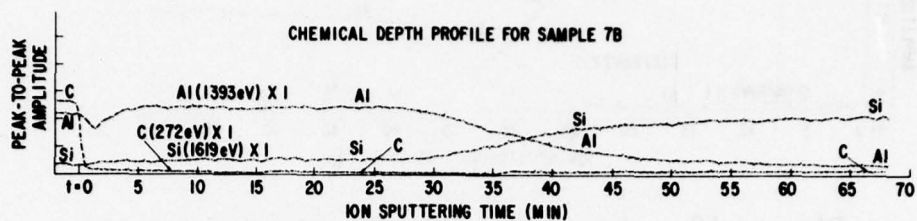


Figure 40. Auger Profile Obtained from Spots Shown in Figure 35

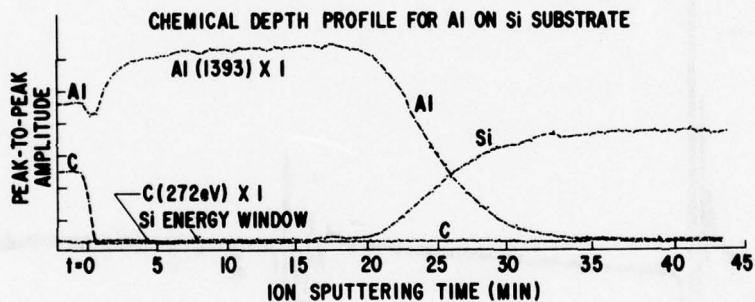


Figure 41. Auger Profile Obtained from the Region Between Spots Shown in Figure 34

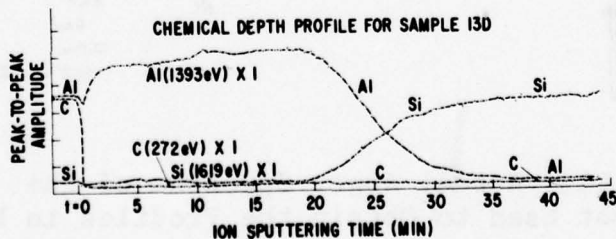


Figure 42. Auger Profile Obtained from Spots Shown in Figure 33

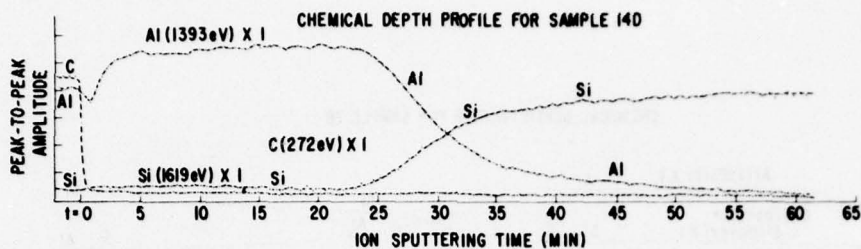


Figure 43. Auger Profile Obtained from Spots Shown in Figure 33

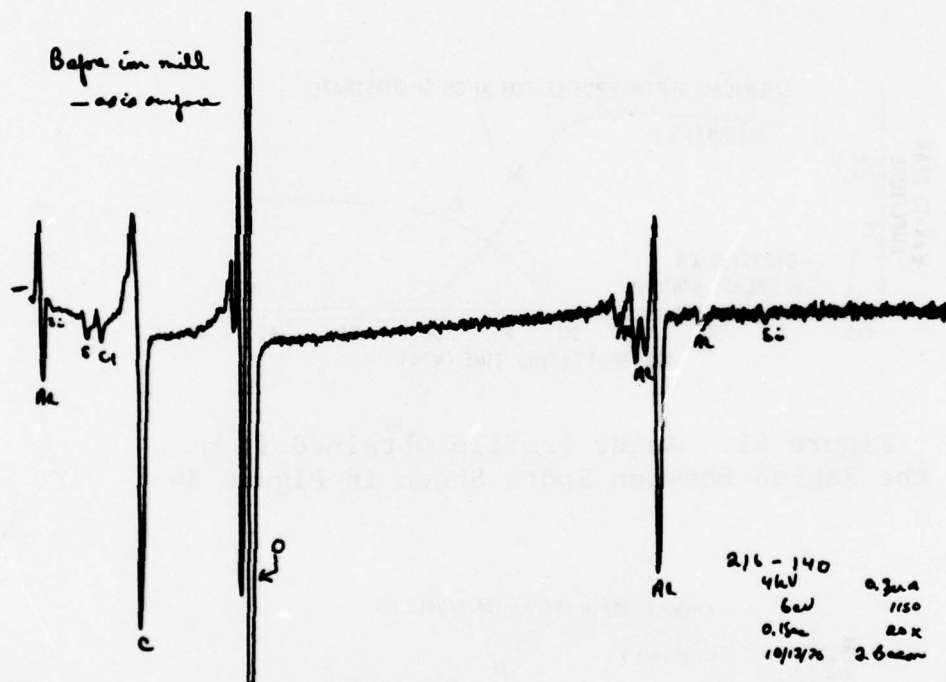


Figure 44. Actual Auger Spectrum of the Surface on the Spot Used to Obtain the Profiles in Figure 43

TABLE 5

AUGER PROFILING RESULTS

Sample No.	% Si in Al	% Al in Si	Junction Depth (min)
1A	20	16	32
2A	26	12	18
5B	25	10	16
7B	10	8	28
9C (matrix)	0	0	20
13D	8	2	19
14D	8	0	23

To discover how deep the region of Al precipitation goes, a linear pattern of closely spaced spots was formed and a 10:1 angle lap performed. Figure 45 shows the results of this angle lap after an etch which decorates Al precipitates with copper metal. The depth is about 5 μ m.

Conclusions

Only the most lightly irradiated spots come close to simulating the effect expected of the electron beam. The surface melting of these (Figure 33) spots does not necessarily imply that the melting point of Al (660°C) was reached since



Figure 45. Photomicrograph Showing the Depth of Melting and Al Precipitation in One of the More Heavily Irradiated Samples (300X). The Bottom Half is a 10:1 Angle Lap. The Array of Closely Spaced Laser Induced Spots is Clearly Seen in the Upper Half

Si is dissolved in the Al at a level close to the eutectic concentration. As will be seen later in this section, even very lightly irradiated spots made by a single laser pulse can be read by an electron beam and such spots will be analyzed by Auger spectrometry early in the next quarter. The fact that the more heavily damaged spots are easily read is of no value since the Si was melted to a depth (5 μ m) far in excess of what is practical in the ultimate system.

Auger Electron Spectrometer

The Surface Analysis Component of the Materials Characterization Branch of the Research and Development Center performs Auger analysis as an in-house service. They are currently using a Physical Electronics Industries Model 548 ESCA/Auger Spectrometer with Model 545 scanning Auger microprobe attachment. Figure 46 shows the physical arrangement of the complete system. Figure 47 is a schematic representation of the principal elements of the spectrometer. The two possible electron gun orientations and the arrangement for simultaneous sputter etching and Auger analysis are indicated. The rays represent paths of transmitted electrons which have a well defined energy determined by the bias between the coaxial cylinders of the electron energy analyzer. As the voltage applied to the outer cylinder is scanned, the secondary

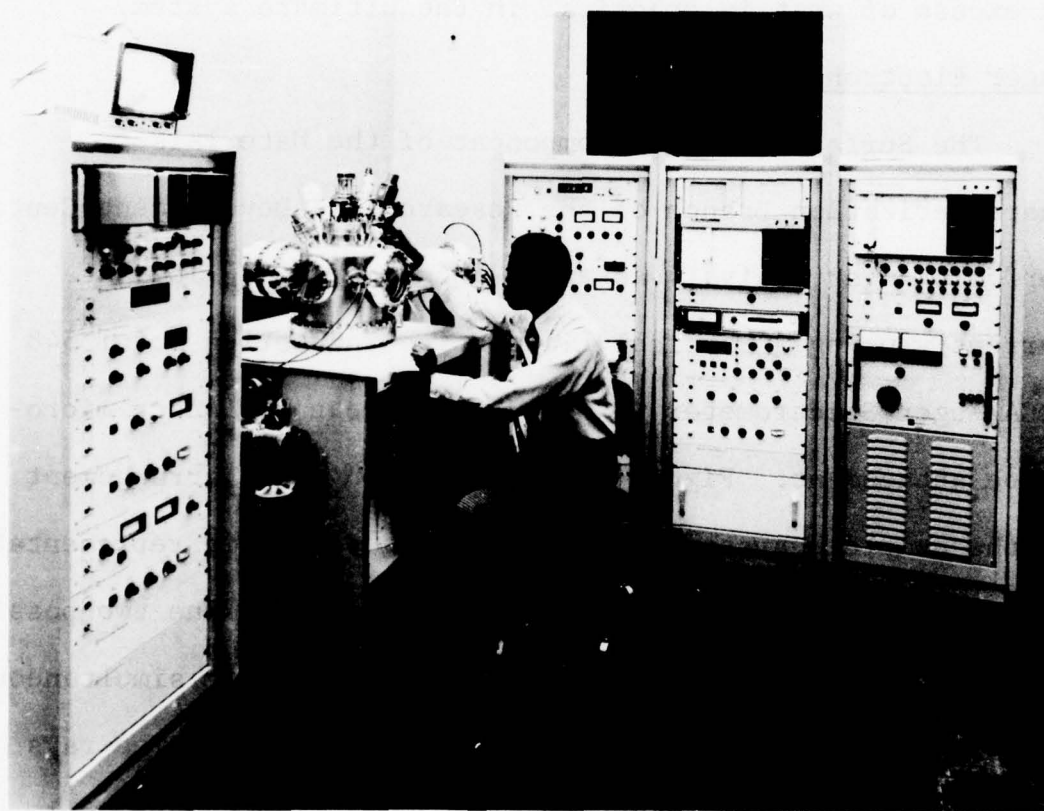


Figure 46. The Auger Electron Spectrometer,
Ion Milling Apparatus and Associated Equipment

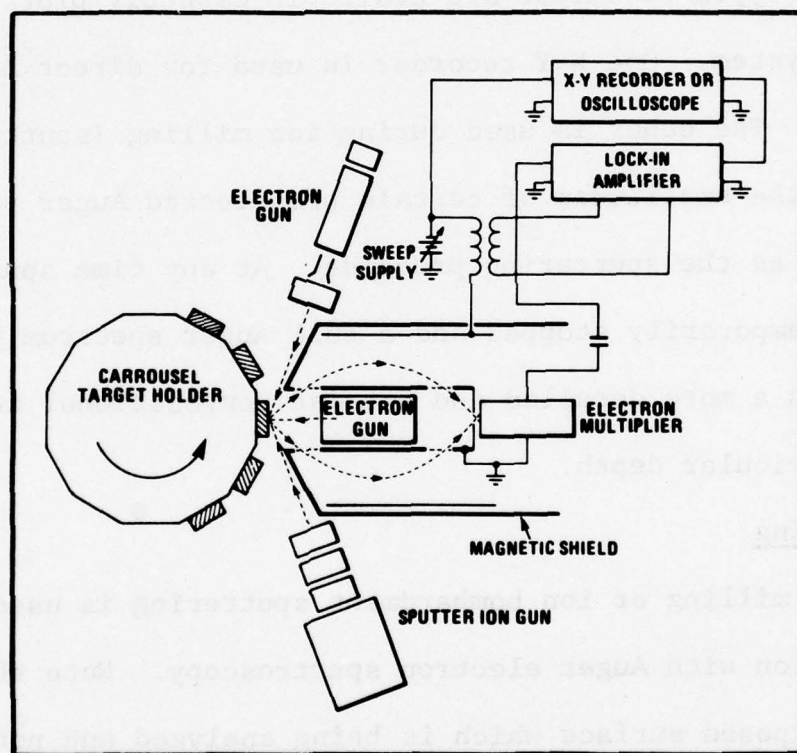


Figure 47. Schematic Representation of the Auger Spectrometer.
The Various Parts Shown Here are Discussed in the Text

electron energy distribution is obtained from the electron multiplier output current. A small a.c. voltage in series with the analyzer is detected by the lock-in amplifier so that the derivative $dN(E)/dE$ vs. E of the secondary electron current is plotted as the Auger spectrum. The rotatable "carrousel" sample holder permits mounting several samples at one time. Figure 48 shows the test chamber with samples visible on the carrousel.

Two types of output are available directly plotted by the system. One X-Y recorder is used for direct Auger spectra. The other is used during ion milling (sputtering) to plot the amplitudes of certain preselected Auger peaks vs. time as the sputtering proceeds. At any time sputtering may be temporarily stopped and a full Auger spectrum plotted to obtain a more detailed and precise compositional analysis at a particular depth.

Ion Milling

Ion milling or ion bombardment sputtering is used in combination with Auger electron spectroscopy. Note that it is the exposed surface which is being analyzed and not the material removed. Since there are substantial differences in the sputtering yields of the elements, their surface concentrations will adjust to compensate for this. Hence, the elemental

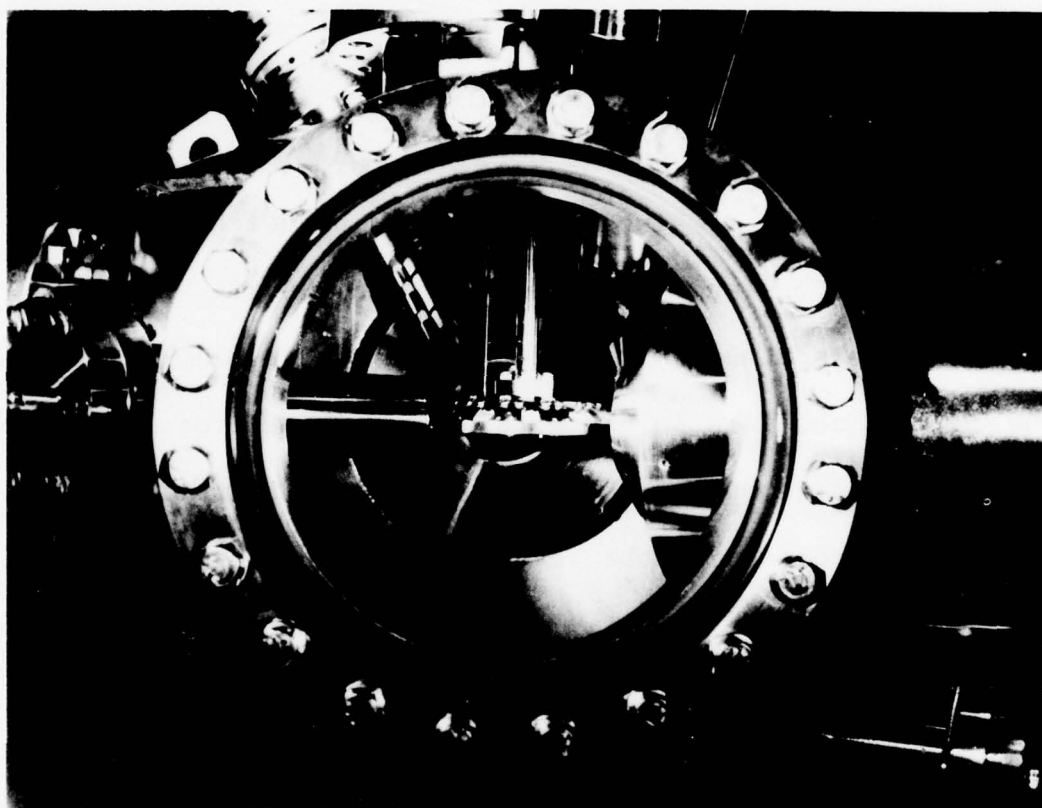


Figure 48. The Test Chamber as Seen Through Viewing Port. The Auger Analyzer and Sputter Ion Gun are on the Right and the Samples can be Clearly Seen Mounted on the Carrousel in the Center

composition of the sputter etched surface will, in general be different from the original bulk solid. The Auger spectrum, because it is derived from the top few atomic layers, will represent this altered composition. The existence of even small amounts of surface deposits of substances having a low sputtering yield can lead to major topological changes in the surface. This fact can lead to anomalously slow milling of otherwise easily sputtered material. The foreign substance may have a very different yield as an impurity than it does as a bulk material. Sputtering rates may also be influenced by defects, dislocation networks and sample orientation. Still another way in which the sputter-etching process can adversely influence the results obtained in elemental composition profiling is by causing displacement of the atoms in the host lattice. This "knock-in" process is most severe when high energy ions are used.

Alloy Junction - Eutectic Writing Experiments

During the first quarter of this contract alloy junction target experiments were performed using an Electro Scientific Industries, Model 25, laser trimming system. This experiment has a Q-switched Nd:YAG laser with programable x-y position which allows a multiplicity of operating conditions in terms

of pulses per position and power delivered. The first studies were aimed at demonstrating alloy junction writing with the laser using a Si n-p planar diode with an Al metal layer.

The first quarter experiments and the results of these experiments are discussed in detail in the first quarter report. Here we will just summarize the important results. First, it was shown that writing could be accomplished with the laser system with multiple pulses. Memory type readout was achieved from laser irradiated areas before and after removal of the Al layer using a Cambridge Mark IIA Stereoscan Scanning Electron Microscope. Second, it was demonstrated by moving the table and writing "on the fly" that writing could be accomplished with a single laser pulse of typically 150 nsec duration. This verified that writing could be achieved on a time scale compatible with a desired 10^7 Hz writing rate for a final memory configuration. Average and peak power measurements were made for the laser system over its full range of operating conditions. Based on these measurements, it was estimated that power densities in the range of 10^7 to 10^8 W/cm² were used in the writing. Considerable surface damage of the Al layer was evident in written areas indicating power well in excess of that required for eutectic alloying was used. Angle

lap and stain measurements of the written areas further confirmed this by showing Al at depths of 5 to 6 μm below the surface of the Al/n-Si interface. This is much greater than anticipated depths for strictly eutectic alloying, expected to be approximately 1/3 to 1/2 of the thickness of the Al layer or approximately 300 to 500 \AA .

Based on the first quarters results the experiments for the second quarter were aimed at demonstrating eutectic alloying of the written regions using the laser system. This goal has been achieved and the experiments and results of these experiments are described in detail in this section of the report.

Laser Experiments for Eutectic Writing

Laser writing experiments were conducted again this quarter using the Model 25 Electro Scientific Industries laser trimmer which is described in detail in Section 6 of the first quarterly report. Readout and analysis of the written areas was done on the Cambridge Scanning Electron Microscope. The target was a planar n or p Si diode. The top surface of the n layer was plasma etched and sputter coated with 1000 \AA of Al to remove and prevent regrowth of the native oxide layer. A cross section of the target is shown in Figure 49.

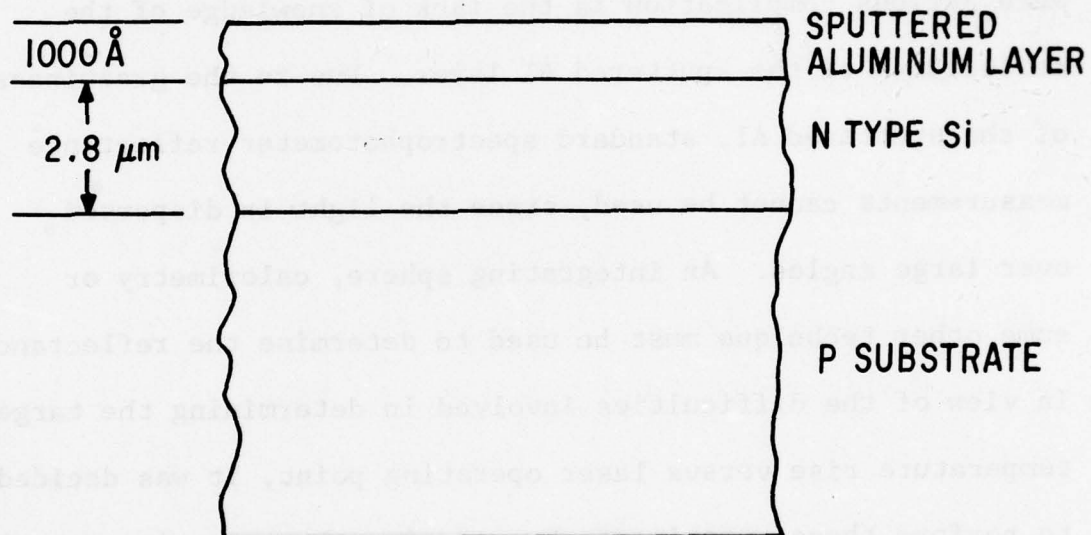


Figure 49. Cross Section of Target Used for Alloy Junction Experiments

As reported in the first quarterly report power measurements were made for the peak and average power of the Nd:YAG laser in the Model 25 system. It was hoped that these data would be useful in determining the temperature rise of the target during writing and predicting future writing temperatures. Unfortunately, the power measurements showed considerable variation in the pulse amplitude and hence peak power from pulse to pulse. Therefore, only an "average" peak power per pulse can be ascertained. An even more serious complication is the lack of knowledge of the reflectance of the sputtered Al layer. Due to the graininess of the sputtered Al, standard spectrophotometer reflectance measurements cannot be used, since the light is dispersed over large angles. An integrating sphere, calorimetry or some other technique must be used to determine the reflectance. In view of the difficulties involved in determining the target temperature rise versus laser operating point, it was decided to perform these experiments by reducing the power in controlled steps from a known operating point.

The operating conditions for the laser system were selected for the most stable point based on the previous power measurements. The lamp drive current was 22 A, Q-switch repetition rate 2 kHz, 60 mil aperture and 10% beam splitter.

A photograph of the laser output pulse for the operating point is shown in Figure 50. The power was reduced for various operating points in the experiment by neutral density filters. These filters are made from Schott glass and can handle the laser power involved while giving an accurately controlled reduction of the power at the target plane. A list of the filters purchased for these and future alloy junction experiments as well as their transmission properties is summarized in Table 6. The density number, D, is logarithmically related to the transmission, T, transmitted energy/input energy as

$$D = \log_{10} \frac{1}{T} \quad (35)$$

TABLE 6

TRANSMISSION VALUES OF SCHOTT GLASS FILTERS

<u>Density</u>	<u>Quantity</u>	<u>Transmission</u>
.1	2	.794
.2	1	.631
.3	2	.501
.4	1	.250
1	1	.10
2	1	.01
3	1	.001
4	1	.0001

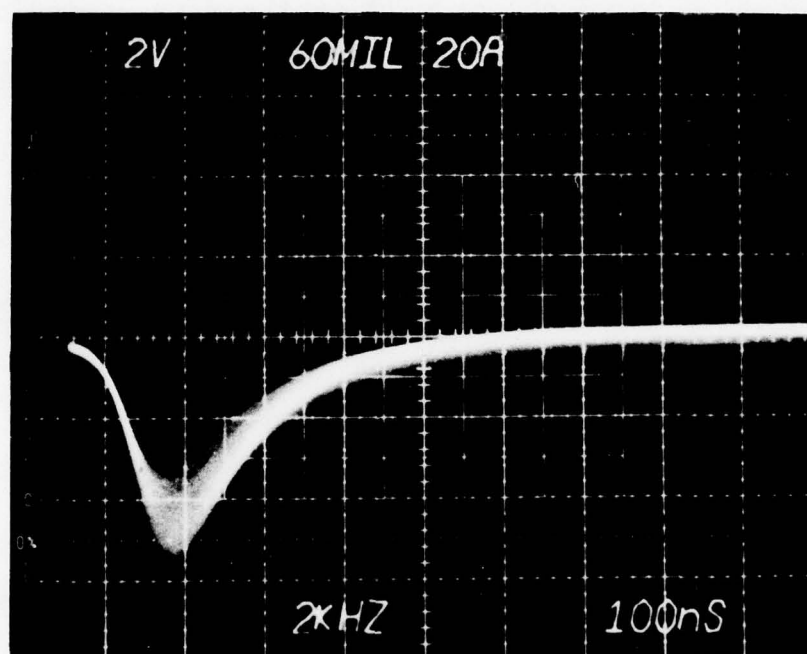


Figure 50. Laser Pulse Output, Laser Pulse at 22 A
Lamp Drive, 60 Mil Aperture, 2 kHz Rep Rate

This set of 8 filters allows full adjustment of laser power in a range $10^4:1$ in 20% steps.

For the eutectic writing experiments, the laser system was programmed to produce a 10×10 array of spots in $20 \mu\text{m}$ centers with 10 pulses per spot. Starting at the operating point previously mentioned, neutral density filters were inserted in the optical system starting at $D = 0.1$ and ending with $D = 0.6$, in increments of 0.1. At each filter setting a 10×10 array was exposed on the target. The starting filter value ($D = 0.1$) was preselected so that the input power at the laser operating point was approximately the same as the first quarter experiments. This allowed formation of alloyed regions without having to worry about punch through of the n layer by too powerful a laser pulse. The last visible surface marks due to pulsing of the laser were at $D = 0.4$. Therefore, continued reduction of the input power for two filter numbers beyond this (i.e. $D = .5$ & $.6$) were carried out before the tests were stopped.

The target with metal layer on was read out using the Scanning Electron Microscope. Each area irradiated, corresponding to a different neutral density filter, was surface inspected by secondary electron techniques. Also each area was investigated by using the planar diode signal to z modulate

the SEM display. Photographs of each area for the neutral density filter range for both secondary emission and planar diode readout are shown in Figure 51(a) to 51(f). Missing from these photos is the secondary emission surface scan for neutral density filter number 0.5. There was no visible surface damage at this filter setting viewed by secondary electrons. The area appeared essentially the same as the secondary electron picture in Figure 51(f) and was therefore not recorded. Even though this was the most stable operating point, there is still considerable power variability as can be seen from a comparison of the secondary emission and planar diode signals at the various filter settings. The percent modulation for several written areas at each of the different irradiated areas was measured at 6 kV landing potential. These data are summarized in Figure 52. Here the availability of laser power shows up in the percent modulation. At each filter value a written area that is typical of the more heavily written regions, as indicated with an x in Figure 52, was selected for more detailed investigation. For each of these written areas, gain versus read beam landing energy was measured. These data are plotted in Figure 53 along with the gain versus landing energy data for the aluminum layer alone.

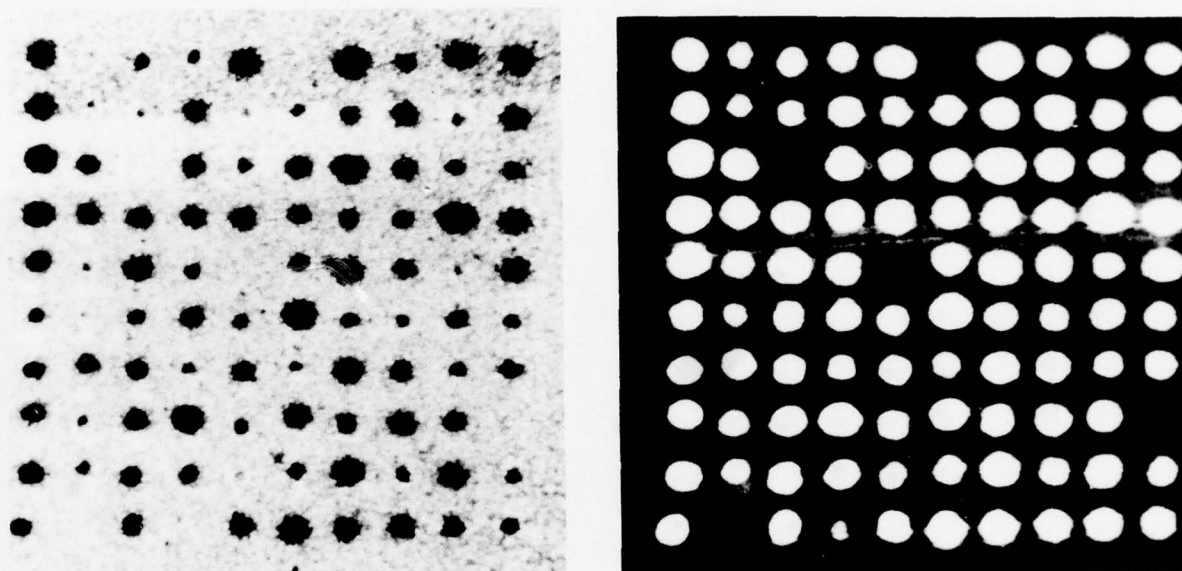


Figure 51(a). Laser Irradiated 10 x 10 Array, 10 Pulses per Spot. Left Secondary Emission Surface Scan. Right Planar Diode Readout. Operating Conditions:
Lamp Current = 22A
Aperture = 60 Mil
Frequency = 2 kHz
Beam Splitter = 10%
Neutral Density Filter = .1

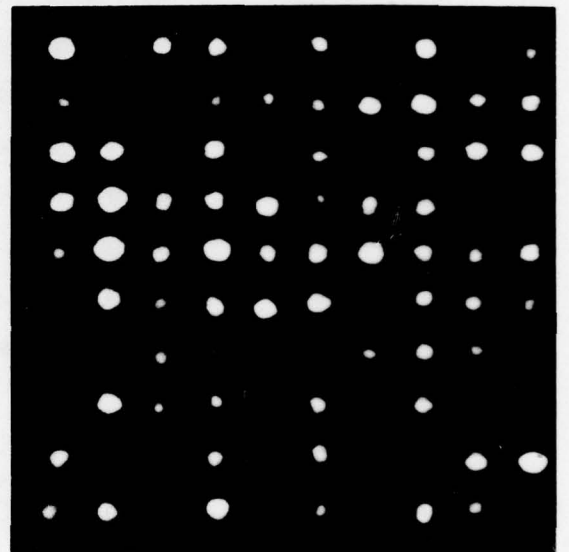
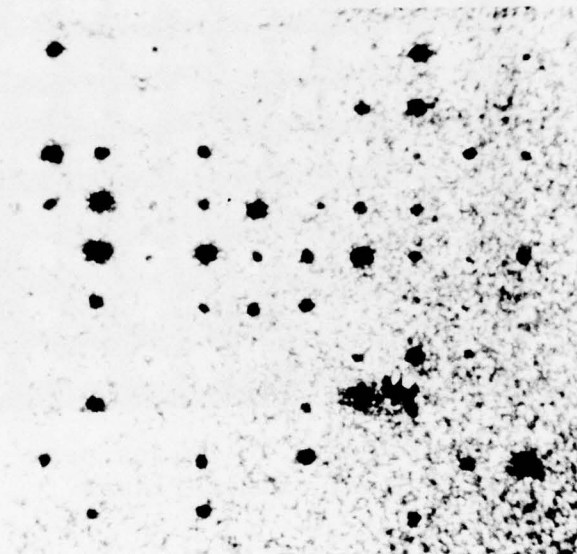


Figure 51(b). Laser Irradiated 10 x 10 Array, 10 Pulses per Spot. Left Secondary Emission Surface Scan. Right Planar Diode Readout. Operating Conditions:
Lamp Current = 22A
Aperture = 60 Mil
Frequency = 2 kHz
Beam Splitter = 10%
Neutral Density Filter = .2

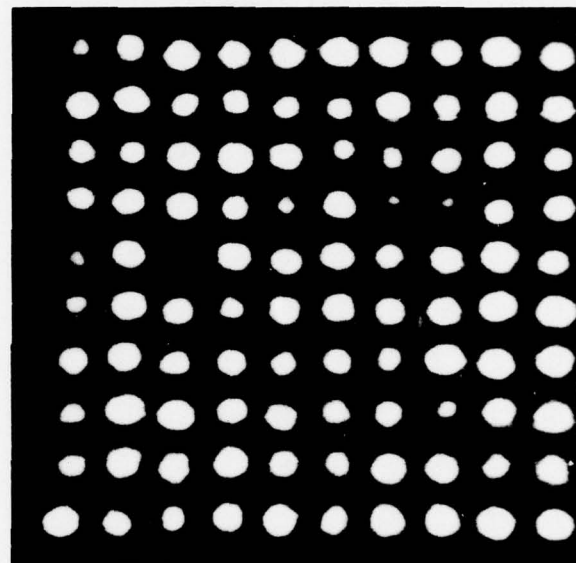
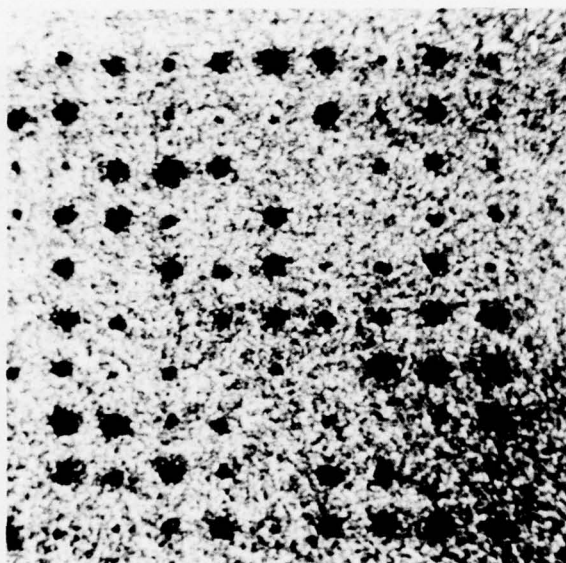


Figure 51(c). Laser Irradiated 10 x 10 Array, 10 Pulses per Spot. Left Secondary Emission Surface Scan. Right Planar Diode Readout. Operating Conditions:
Lamp Current = 22A
Aperture = 60 Mil
Frequency = 2 kHz
Beam Splitter = 10%
Neutral Density Filter = .3

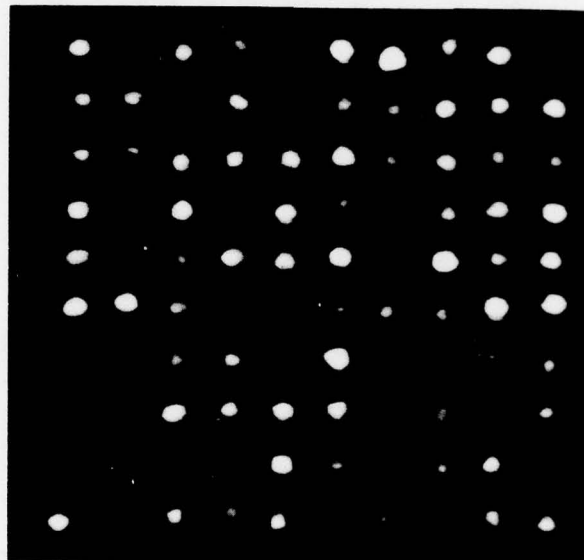
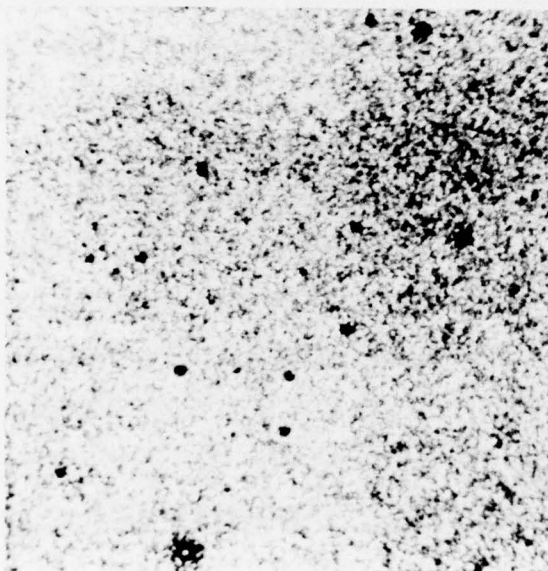


Figure 51(d). Laser Irradiated 10 x 10 Array, 10 Pulses per Spot. Left Secondary Emission Surface Scan. Right Planar Diode Readout. Operating Conditions:

Lamp Current = 22A

Aperture = 60 Mil

Frequency = 2 kHz

Beam Splitter = 10%

Neutral Density Filter = .4

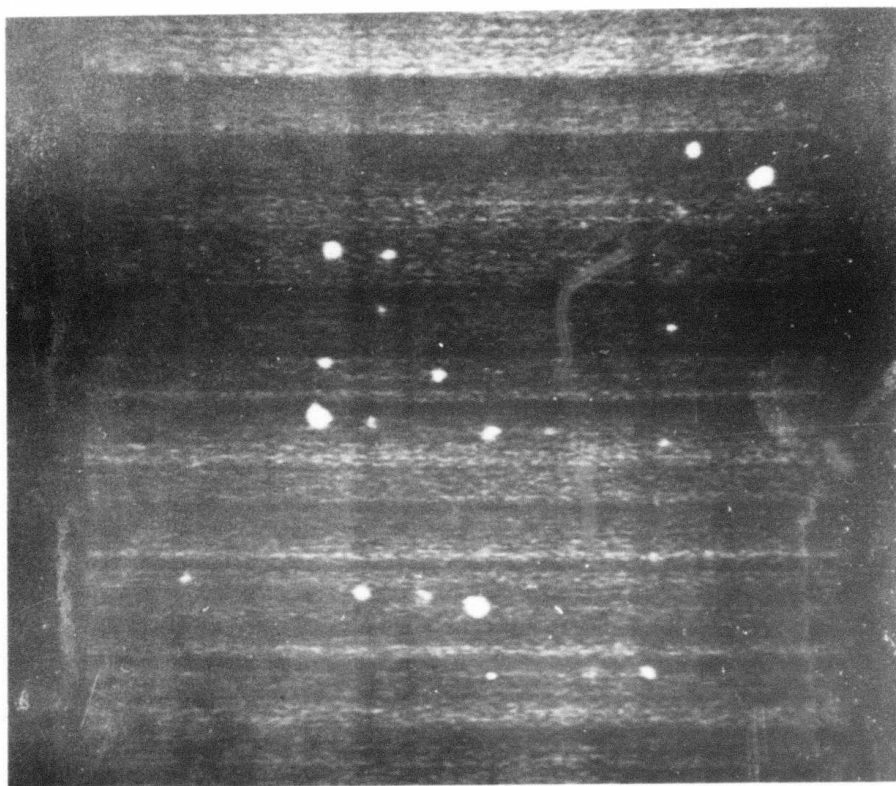


Figure 51(e). Laser Irradiated 10 x 10 Array, 10 Pulses per Spot. Planar Diode Readout. Operating Conditions:
Lamp Current = 22A
Aperture = 60 Mil
Frequency = 2 kHz
Beam Splitter = 10%
Neutral Density Filter = .5

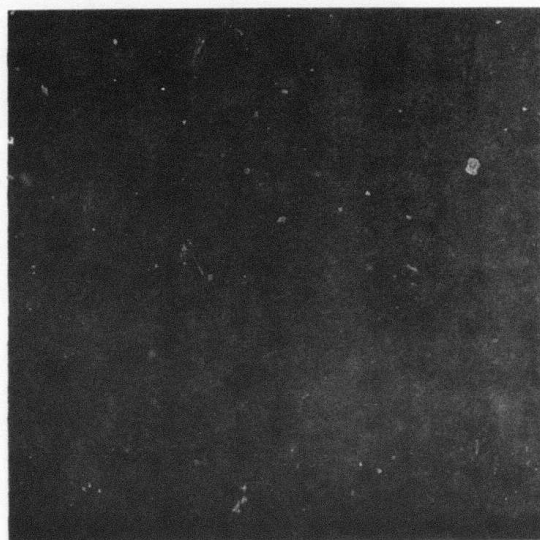
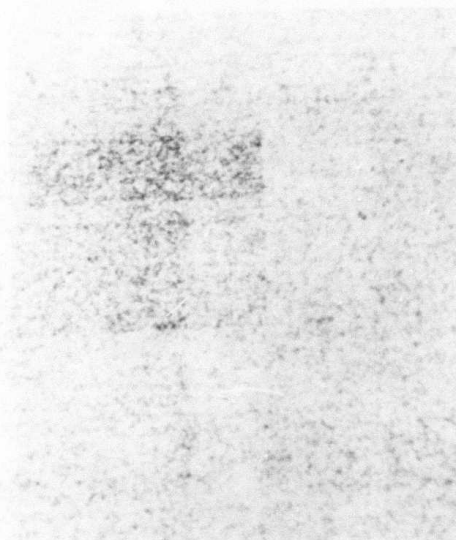


Figure 51(f). Laser Irradiated 10 x 10 Array, 10 Pulses per Spot. Left Secondary Emission Surface Scan. Right Planar Diode Readout. Operating Conditions:

Lamp Current = 22A

Aperture = 60 Mil

Frequency = 2 kHz

Beam Splitter = 10%

Neutral Density Filter = .6

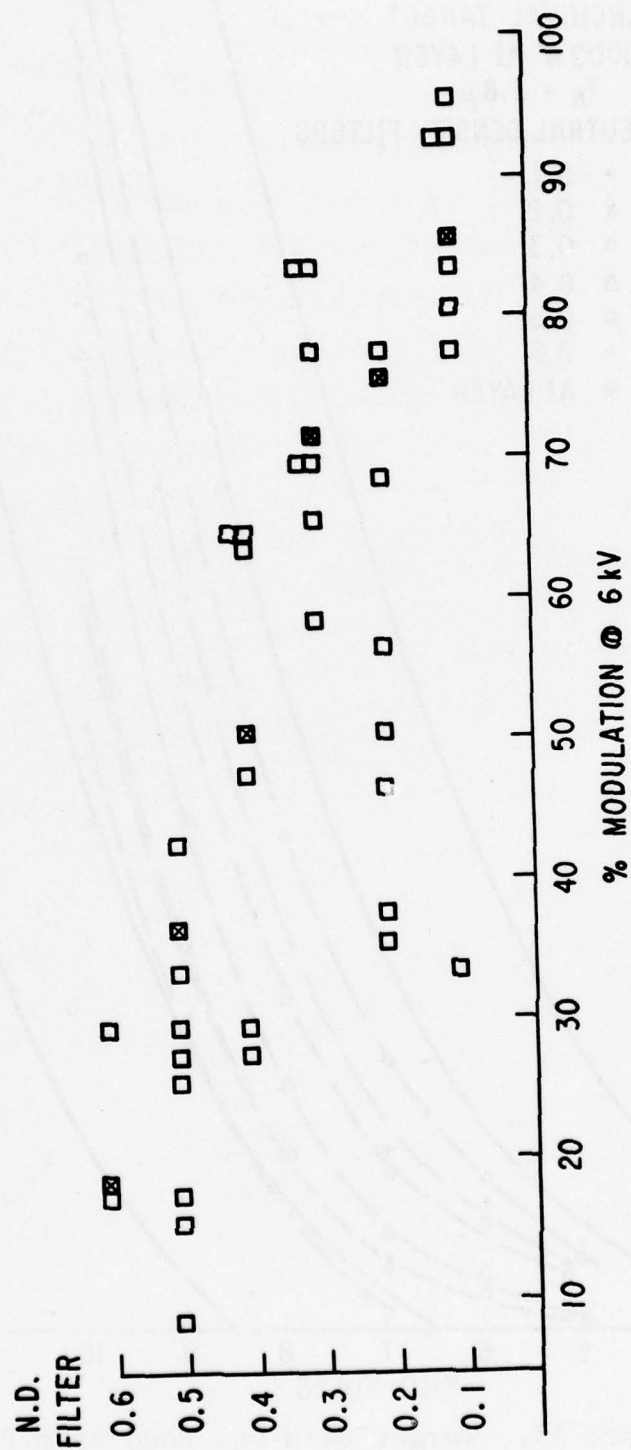


Figure 52. Percent Modulation at 6 kV Read Beam Potential for Several Alloy Written Regions at Each Neutral Density Filter Setting

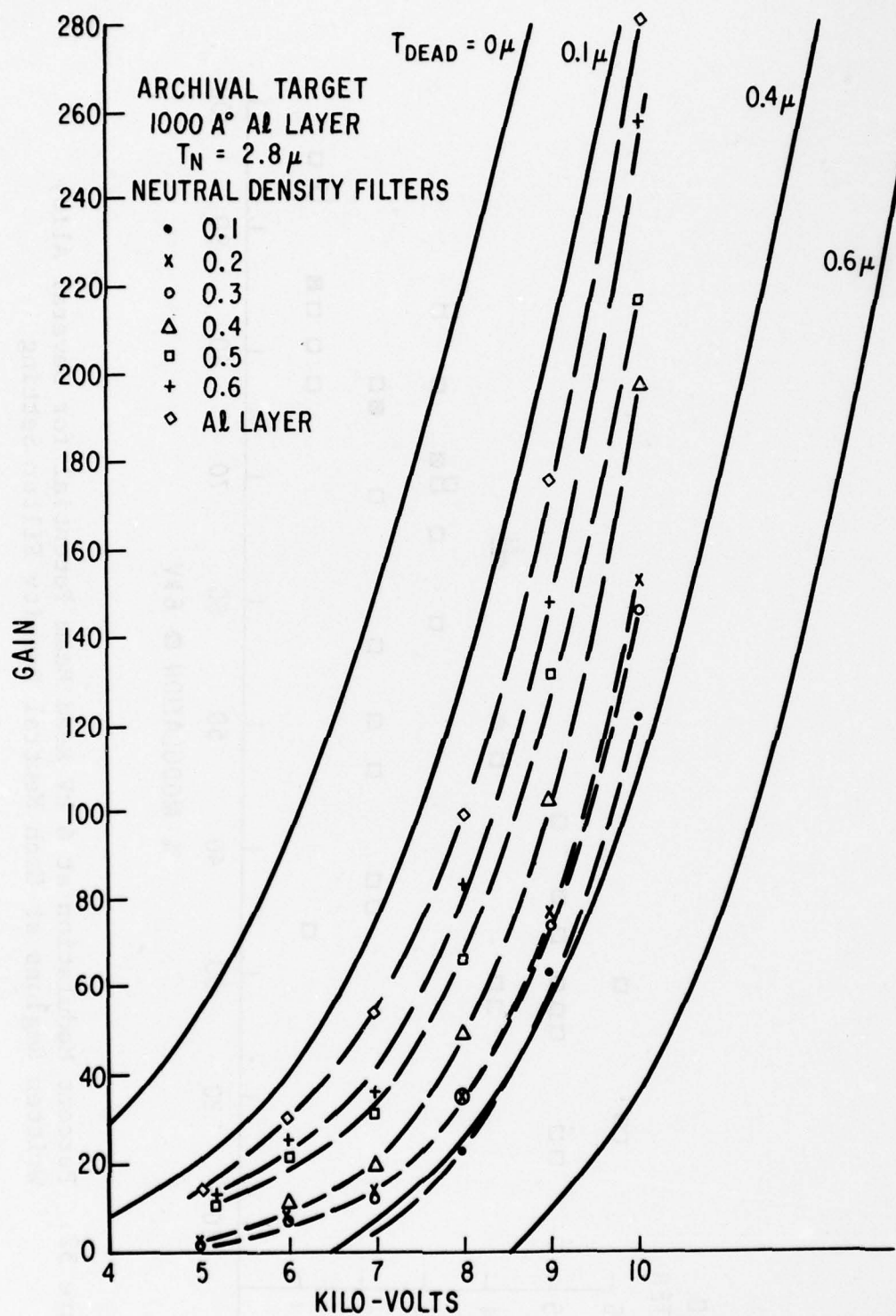


Figure 53. Target Gain vs. Read Beam Potential

Superimposed on these data are gain versus landing energy curves calculated with one dimensional model for various "dead-layer" thicknesses as described in Section II. At energies greater than 7 keV there is an excellent fit between the model and experimental curves. Using the gain vs. landing energy curves for the model, the gain versus "dead-layer" thickness at 9 keV shown in Figure 54 was developed. At 9 keV landing potential, the experimental gain was used in conjunction with Figure 22 to estimate the dead-layer thickness, T_D , for each written area and for the Al layer by itself. The writing depth, W_D , was estimated by subtracting the dead-layer thickness for the sputtered Al by itself. These data for these written areas are summarized in Table 7.

TABLE 7

EXPERIMENTAL GAIN VS. DEAD-LAYER THICKNESS AND WRITING DEPTH

G	Td Å	Wd Å	Target Area
175	0.15 μ	0	Al layer only
64	0.39 μ	0.24 μ	0.1 N.D. filter
76	0.36 μ	0.21 μ	0.2 " "
74	0.37 μ	0.22 μ	0.3 " "
103	0.29 μ	0.14 μ	0.4 " "
131	0.23 μ	0.08 μ	0.5 " "
148	0.20 μ	0.05 μ	0.6 " "

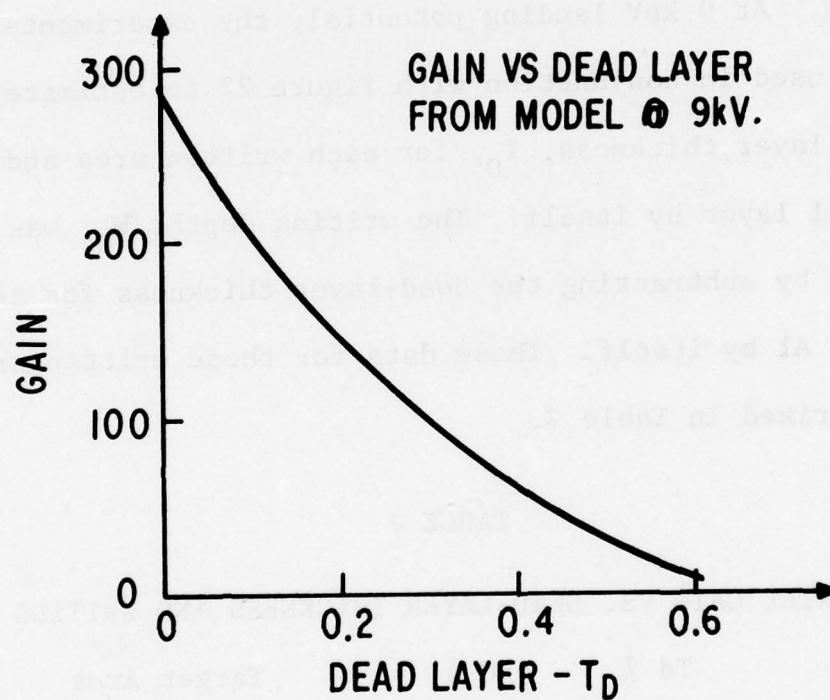


Figure 54. Target Gain vs. Dead-Layer Thickness
Based on the One Dimensional Model

Based on the experiments of this quarter the goal of eutectic point writing has been achieved. As shown in Figures 51(e) and 51(f) memory readout of laser irradiated areas without visible damage to the Al layer surface was demonstrated. This implies that the laser writing beam in these areas supplied enough power to raise the Si-Al interface to a temperature at or above the eutectic point (577°C) but below the Al melting point (660°C). Eutectic writing has further been confirmed by analysis of the target gain of the laser irradiated areas. As seen from the data in Table 7, the writing depth achieved with neutral density filters of 0.5 and 0.6 (corresponding to the areas shown in Figures 51(e) and 51(f)) is on the order of $1/3$ to $1/2$ the initial Al layer thickness. These writing depths are in agreement with expected values for writing near the eutectic.

The experiments this quarter were carried out with 10 pulses per spot. This is not a serious handicap, since as was shown in the first quarter single pulse per spot writing can be achieved for the same laser operating conditions. This was in agreement with our initial prediction of the writing mechanism on thermal time constants of the materials. However, a program for the laser system is being written to form arrays

of single pulse per spot fields. Single pulse experiments and further characterization of the written areas is planned for the next quarter.

Thermal Bias Studies

As has been previously noted in the first quarterly report and also above, the maximum achievable energy densities in a submicron diameter electron beam may be insufficient to heat a typical semiconductor-metal system from room temperature to its eutectic temperature, e.g., to the Si-Al eutectic at 577°C. To overcome this problem, thermal biasing of the target to near the eutectic point has been suggested. Such thermal biasing would also provide the "hysteresis" needed so that electron beam writing could not accidentally be carried on while reading, etc.

The thermal biasing could be carried out in a number of different ways. A "large"-area, off-axis, pulsed electron beam, or a laser beam, for example, could be used such that only the immediate area to be written would be heated. This would have the advantage of thermally cycling only a small portion of the target and of reducing the total heating time in any given portion since only that portion would have to be heated once while writing. However, close temperature control over the writing area would be challenging to achieve.

The simplest approach is to uniformly heat the whole target with an auxiliary resistance heated stage. This, however, raises some serious questions relating to the stability of the metal-semiconductor interface near the eutectic temperature arising from the solid-state diffusion of the eutectic component species. For example, in the total accumulated writing time (days), significant alloying may occur. Also, the thermal cycling involved in successive writing sessions may cause solution and precipitation (regrowth) in critical amounts. A discussion of some of these kinds of problems with references to the literature can be found in the first quarterly report.

Two general experimental approaches are being planned for the next quarter to study these possible complications. One is to cycle metallized Ge and Si wafers in standard processing furnaces. These samples will then be studied using standard metallographic techniques to look for changes in the metal-semiconductor interface. A second experiment is to repeat the laser experiments but using a heated stage. Actual writing will be carried out and it will be noted whether the laser power required to write is reduced as expected. Also, previously written areas on a given wafer will be re-read after each writing cycle to see if there is

any degradation in the signal with thermal bias temperature, time, and/or cycling.

To carry out these proposed laser experiments, a heated stage is desired with the following features: (1) A "large" flat heating station to accommodate Si/Ge wafers up to 2 inches in diameter; (2) A window so that the sample can be exposed to the laser beam; (3) A reasonably low temperature gradient and close absolute temperature control ($\sim < 5^{\circ}\text{C}$) so that operation near the eutectic temperature can be realized without the danger of accidentally alloying; and (4) The capability of maintaining temperatures up to at least the Si-Al eutectic, 577°C .

Commercially available microscope heating stages such as those made by E. Leitz, Inc., were considered. While very well built and, with a quartz window, capable of handling the requirements of accessibility to the laser beam, they provide only a very small heated area. Not only would this require small samples but there would be problems of temperature gradients and of monitoring the actual sample temperature. For these reasons, a specially designed heated stage was built. Figure 55 shows a photograph of this stage. Details of particular construction features are noted in Figure 56 and are described in the following paragraphs.



Figure 55. Photograph of Laser Heating Stage

In designing any thermal station, a basic question involved is whether the thermal stability that is desired should be achieved through thermal mass loading or by an electronic feedback loop. The former requires a massive heater assembly; the latter a very low thermal mass for rapid response and close control. We chose the latter approach. Figure 56 shows the basic features of our design. Low mass is achieved with the hollow cylindrical heater assembly as shown. The heater (not shown) is wound on the circumference of this section which is an integral part of the flat-top sample support forming an inverted cup. This and the high thermal conductivity of the material (moly) assures good heat transfer with minimum thermal mass. The bottom piece of the heater assembly is perforated with many large holes to reduce the thermal mass and to provide some thermal resistance. It is also moly and is nickel-brazed to the top piece. It in turn is screwed to the stainless steel post shown which provides the principal thermal resistance. This post is soft-soldered to the bottom brass vacuum enclosure and can be easily changed to optimize the thermal "leak".

The heater was made as follows: The circumference of the heater assembly was coated with a ceramic layer applied

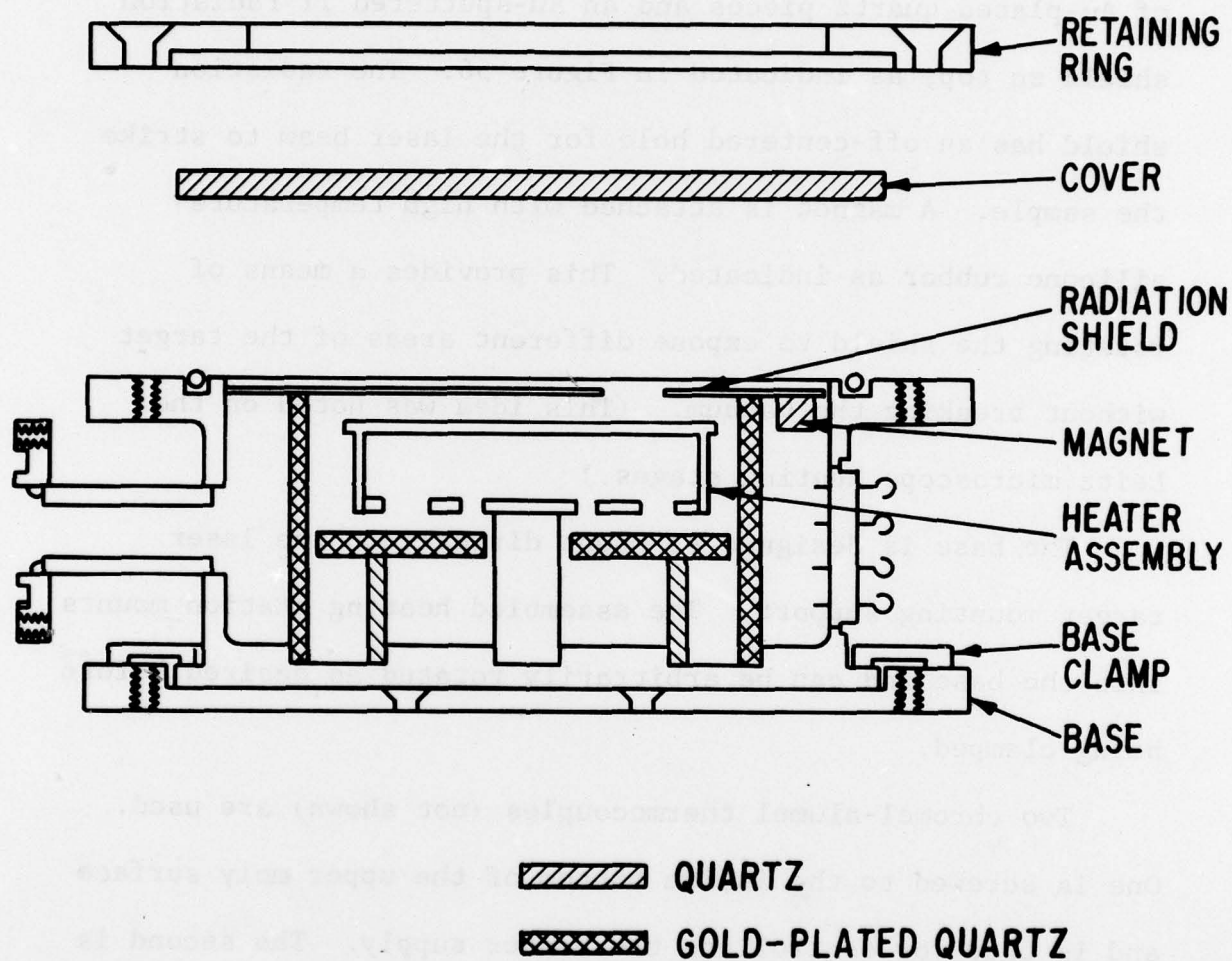


Figure 56. Schematic of Laser Heating Stage. See Text for a Description of Various Parts

with a plasma flame spray gun (Metco Co.). Nineteen turns of 7-mil nichrome wire were applied and held in place with Sauereisen No. 1 cement. This gives 100 ohms of cold resistance.

An "oven" is formed around the heater assembly by use of Au-plated quartz pieces and an Au-sputtered Ti radiation shield on top, as indicated in Figure 56. The radiation shield has an off-centered hole for the laser beam to strike the sample. A magnet is attached with high temperature silicone rubber as indicated. This provides a means of rotating the shield to expose different areas of the target without breaking the vacuum. (This idea was noted on the Leitz microscope heating stages.)

The base is designed to mount directly on the laser target mounting support. The assembled heating station mounts into the base and can be arbitrarily rotated as desired before being clamped.

Two chromel-alumel thermocouples (not shown) are used. One is screwed to the inside bottom of the upper moly surface and is used for controlling the heater supply. The second is screwed to the top surface (see photograph) at the edge and is used for monitoring the temperature and checking on temperature gradients. The heater supply is a Love Controls Corp., Model 71

Solid State Potentiometric Controller which operates into a Variac which in turn drives the heater. The Variac is not necessary, but is used to set the "operating point".

SECTION VI

OPTICS STUDY

As part of this Phase I effort for the Advanced Archival Memory program, analytical studies of the writing optics required for both memory techniques (ion implant/alloy junction) are planned. These studies have been purposely scheduled to occur during the second half of the contract so that more information on the target write/read requirements could be factored into the optics study. A further reason for deferring these studies was to allow at least preliminary results from the Oregon Graduate Center source development contract (F33615-76-C-1327) to be used in the optics analysis. Since this report marks the midpoint of the contract period, the analytical optics studies will begin in the next quarter.

The delay in starting the optics study appears to have been justified. Recent target developments for the ion implanted concept show that damage writing (as opposed to p/n junction formation), with inert gas ions for example, is possible. This writing method shows initial possibilities of reducing the writing beam fluence and thereby easing the requirements on source brightness. Along this same line recent

developments of an argon field ionization source at the Oregon Graduate Center appear promising for this application. Advances are also being made at Oregon on the Ga liquid emitter field ion source. Total beam currents of 70 to 140 μ A have been achieved to date and progress is being made in achieving stable d.c. emission. This source is an attractive candidate for implanting surface diodes.

Since the desired goal is 0.1 μ m bit size field emission or field ionization sources are in general superior to other sources of electrons and ions because of their high brightness, small source size and lower energy spread. However, because of their small virtual source the field emission and ionization sources pose different optical problems than conventional thermal electron or plasma ion sources. Therefore the first phases of the optics study will deal with the problem of coupling between the source and lens system. This will also be accompanied by a thorough investigation of the capabilities of various sources. These inputs will then be used in the evaluation of write station capabilities in the concluding phases of the optics study.

REFERENCES

1. Caughey and Thomas, Proc. IEEE Letters, Dec. 1967, p. 2192.
2. G. Baccarani and P. Ostoga, Solid State Elect. 18, 1975, p. 579.
3. J. Guldberg and D. K. Schroder, Theoretical and Experimental Gain of Electron-Excited Silicon Targets, IEEE Trans. on Electron Devices, ED-18, 1971, pp. 1029-35.
4. E. J. Sternglass, Backscattering of Kilovolt Electrons from Solids, Phys. Rev. 95, 1954, pp. 345-58.
5. F. N. Schwettmann, "Enhanced Diffusion during the Implantation of Arsenic in Silicon," Appl. Phys. Lett. 22, (1973), pp. 570-2.
6. G. Dearnaley, M. A. Wilkens, P. D. Goode, J. H. Freeman and G. A. Gard, in Proceedings of the Conference on Atomic Collision Phenomena in Solids (North Holland, Amsterdam, 1970).
7. G. W. Ellis, G. E. Possin and R. H. Wilson, "Diode Detection of Information Stored in Electron-Beam Addressed MOS Structures," Appl. Phys. Lett. 24, May 1974, pp. 419-421.

8. S. Dash and M. L. Joshi, "Diffusion-Induced Defects and Diffusion Kinetics in Silicon," AIME, Proceedings Defects in Electronics Materials for Devices Conference, Boston, Mass., August 1969, pp. 202-222.
9. T. M. Buck, H. C. Casey, Jr., J. V. Dalton, and M. Yamin, "Influence of Bulk and Surface Properties on Image Sensing Silicon Diode Arrays," BSTJ 47, (1968), pp. 1827-54.
10. E. I. Gordon and M. H. Crowell, "A Charge Storage Target for Electron Image Sensing," BSTJ 47, (1968), pp. 1855-73.
11. A. R. Moore and W. M. Webster, "The Effective Surface Recombination of a Germanium Surface with a Floating Barrier," Proc. IRE 43, April 1955, pp. 427-435.
12. J. Gibbons, W. S. Johnson, S. W. Mylroie, "Projected Range Statistics," Dowden, Hutchinson & Ross, Inc., Stroudsburg, Pa., 1975.
13. E. Tannenbaum, "Detailed Analysis of Thin Phosphorous-Diffused Layers in p-Type Silicon," Solid-State Electron., Vol. 2, 1961, pp. 123-132.
14. W. R. Runyan, "Semiconductor Measurements and Instrumentation," McGraw-Hill, New York 1975, Ch. 3.

15. G. Dearnaley, J. H. Freeman, R. S. Nelson, and J. Stephen, "Ion Implantation," American Elsevier, New York 1973, Ch. 5.
16. J. A. Davies, G. C. Ball, F. Brown, and B. Domeij, "Range of Energetic Xe^{125} Ions in Monocrystalline Silicon," Can. J. Phys., Vol. 42, June 1964, pp. 1070-1080.
17. E. F. Duffek, C. Mylroie, and E. A. Banjamini, "Electrode Reactions and Mechanism of Silicon Anodization in N-Methylacetamide," J. Electrochem. Soc., Vol. 111, September 1964, pp. 1042-1046.
18. P. F. Schmidt and W. Michel, "Anodic Formation of Oxide Films on Silicon," J. Electrochem. Soc., Vol. 104, April 1957, pp. 230-236.
19. K. M. Busen and R. Linzey, "Removal of Thin Layers of n-Type Silicon by Anodic Oxidation," Trans. Met. Soc. AIME, Vol. 236, March 1966, pp. 306-309.
20. W. Przyborski, J. Roed, J. Lippert, and L. Sarholt-Kristensen, "A Refined Oxidation-Stripping Technique of Thin n-Type Si Films," Rad. Eff., Vol. 1, 1969, pp. 33-39.
21. P. F. Schmidt and A. E. Owen, "Anodic Oxide Films for Device Fabrication in Silicon," J. Electrochem. Soc., Vol. 111, June 1964, pp. 682-688.

22. W. K. Hofker, H. W. Werner, D. P. Oostlock, and N. J. Koeman, "Boron Implantations in Silicon: A Comparison of Charge Carrier and Boron Concentration Profiles," Appl. Phys., Vol. 4, 1974, pp. 125-133.
23. R. A. Sigsbee, private communication.
24. J. Wong and M. Ghezzi, "Arsenic Diffusion in Silicon Using Low As_2O_3 -Content Binary Arsenosilicate Glass Sources," J. Electrochem. Soc., Vol. 119, October 1972, pp. 1413-1420.
25. J. C. C. Tsai, "Shallow Phosphorous Diffusion Profiles in Silicon," Proc. IEEE, Vol. 57, September 1969, pp. 1499-1506.
26. See L. B. Valdes, Proc. IRE 42, (1954) 420 for a detailed analysis of four-point probe measurements.
27. R. A. Evans and R. P. Donovan, Solid-State Electron. 10 (1967) p. 155.
28. D. M. Caughey and R. E. Thomas, Proc. IEEE 55 (1972) p. 2192.
29. G. Baccarani and P. Ostojic, Solid-State Electron. 18 (1975) p. 579.